MODELING AEROSOLS FORMED IN THE RING - PACK OF A RECIPROCATING PISTON

A DISSERTATION IN
Mechanical Engineering
and
Physics

Presented to the Faculty of the University
of Missouri-Kansas City in partial fulfillment of
the requirements for the degree

DOCTOR OF PHILOSOPHY

by
BRIAN ELLIS DALLSTREAM

M.S., University of Missouri – Kansas City, 2006
B.S., University of Missouri – Kansas City, 2003

Kansas City, Missouri
2012

MODELING AERSOLS FORMED IN THE RING - PACK

OF A RECIPROCTING PISTON

Brian Ellis Dallstream, Candidate for the Doctor of Philosophy Degree

University of Missouri – Kansas City, 2012

ABSTRACT

The hydrocarbon emissions of an internal combustion engine are directly correlated with the engine's oil consumption. This oil consumption is associated with reverse blow-by, a condition in which gases flow past the ring-pack from the crankcase to the combustion chamber. This reverse blow-by breaks down the oil film on the cylinder walls and entrains oil particles in the gas flow during the downstroke of the piston.

In this project a numerical model was developed that accurately describes the formation of aerosols in the ring pack by simulating the mechanisms by which oil globules are broken up, atomized, and entrained in a gas flowing through an orifice. The results of this numerical model are in good agreement with experimental values. Thus, this numerical model gives insight into the parameters that govern oil consumption.

A discussion is also presented regarding the general applications of atomization and how past researchers have developed and advanced the theories of atomization.

Included in this discussion is an introduction to past models of oil consumption and the conditions needed for aerosols to form within the ring-pack of a piston.

The faculty listed below, appointed by the Deans of The School of Computing and Engineering and the College of Arts and Sciences have examined a dissertation titled "Modeling Aerosols formed in the Ring Pack of a Reciprocating Piston," presented by Brian E. Dallstream, candidate for the Doctor of Philosophy degree, and certify that in their opinion it is worthy of acceptance.

Supervisory Committee

Bryan R. Becker, Ph.D., P.E.
Department of Civil-Mechanical Engineering

Ganesh Thiagarajan, Ph.D., P.E.
Department of Civil-Mechanical Engineering

Da-Ming Zhu, Ph.D.
Department of Physics

Fred Leibsle, Ph.D.
Department of Physics

Donald Priour, Ph.D.
Department of Physics

CONTENTS

LIST OF FIGURES

LIST OF TABLES

Table Page

LIST OF GRAPHS

NOMENCLATURE

A ..... area
F ..... force
L ..... length
P ..... pressure
Q ..... volumetric flow rate
R ..... gas constant for nitrogen, 0.29680 kJ / kg·K
T ..... temperature
V ..... volume or velocity
a ..... viscosity coefficient or acceleration
b ..... viscosity coefficient
c ..... viscosity coefficient
concentration ..... concentration of aerosol
g ..... gravity, 9.81 m/s^2
h ..... height
m ..... mass
mT ..... total oil mass
r ..... radius
x ..... thickness or distance ligament moves
$\dot{m}$ ..... mass flow
ρ ..... density
θ ..... angle
σ ..... tension
μ ..... viscosity
dE/dt ..... strain rate
Δx ..... change in thickness
Δt ..... change in time
dx/dt ..... velocity of deformation, x – direction with respect to time
dU_∞/dy ..... velocity of oil globule in x - direction with respect to height
$\Delta\rho$ ..... difference in density between oil globule and gas

Subscripts

c ..... central
drop ..... droplet
I ..... internal
LIG ..... ligament
max ..... maximum
N ..... normal force
OIL ..... denotes oil
P ..... pressure
S ..... surface
V ..... perpendicular
x ..... x – direction

1.....Location 1 or outermost circumference
2.....Location 2 or innermost circumference
3.....Location 3 or boundary layer
4.....Location 4 or internally from oil globule
5..... Location 5

ACKNOWLEDGEMENTS

I sincerely thank my advisor, Dr. Bryan R. Becker, for his dedicated guidance, suggestions, and encouragement during my doctoral studies. It would have not been possible to accomplish this research without his help. I want would also like to thank Dr. Brian A. Fricke not only for his excellent academic advise, but also for his endless support in the past 5 years.

I would also like to thank the other members of my doctoral committee, Dr. Ganesh Thiagarajan, Dr. Da-Ming Zhu, Dr. Fred Leibsle, and Dr. Donald Priour. Their comments and suggestions were greatly appreciated. Special thanks are also due to Harold McCormick, head engineer, manager, and owner of CK Engineering, St. Louis Missouri for providing experimental data and his support.

Finally, I sincerely want to thank the Missouri Space Grant Consortium, a funding organization overseen by the National Avionics and Space Administration (NASA) for providing funding for this work. Without them, my doctoral research would have not been possible.

DEDICATION

I dedicate this dissertation to my wonderful family; particularly to my understanding and patient wife, Katie, who has put up with these many years of research, and to our precious son Riley, who is the joy of our lives. I must also thank my loving parents and my terrific in-laws who have given me their fullest support.

CHAPTER 1

INTRODUCTION

The piston rings of an internal combustion engine form a seal between the cylinder wall and the piston in an attempt to prevent gas leakage from the combustion chamber to the crankcase and vice versa. Gas leakage carries carbon particles from the combustion chamber to the crankcase thus degrading lubricant cleanliness. Carbon particles accelerate the wear of the piston, rings, and cylinder wall surfaces by abrasively changing their designed smoothness. The smoothness of these surfaces is designed to counter high friction which causes unnecessary cylinder wall wear, poor quality sealing, and erratic motions of the piston. In short, the piston rings have sealing and dynamic roles which must be optimized to ensure low emissions and long engine life.

The first patented piston ring design dates back to the steam engine era of the 1850's - 1860's. Then as today, the objective was to have a tight seal between the cylinder wall and the piston ring. It wasn't until Ramsbottom designed a split ring that fit into a circumferential groove in the piston, that ring leakage was greatly reduced [1, 2]. This design was later improved when Miller redesigning the ring to be a looser fit by machining the ring thinner and lighter to allow gas pressure behind the ring to change with the pistons' movement [3]. These two designs are the earliest documented cases of the piston ring-pack and are considered to be forerunners of modern ring-pack design.

Since the time of Ramsbottom and Miller, research has shown that a single ring does not adequately seal and separate the flows from the combustion chamber to the crankcase and vice versa. By utilizing a series of rings, the sealing is greatly increased and the dynamic stability improved by reducing the wobble of the piston. Figure 1

depicts a typical series of rings constituting a ring-pack. Figure 1 also depicts the first, second, and third lands which are the machined surfaces between the ring grooves on the piston. The first ring, or the top level ring, is the first of two compression rings and has the primary goals of sealing gases and controlling upward oil movement. The second ring, also known as a scraper ring, has the same primary goals as the first ring, however; it has the added function of scraping oil off the cylinder wall during the piston's downstroke. The third ring, known as the oil control ring, is the oil transporter for the cylinder wall. It collects the oil from the scraper ring and distributes it up and down the cylinder wall in the direction of the piston's movement.

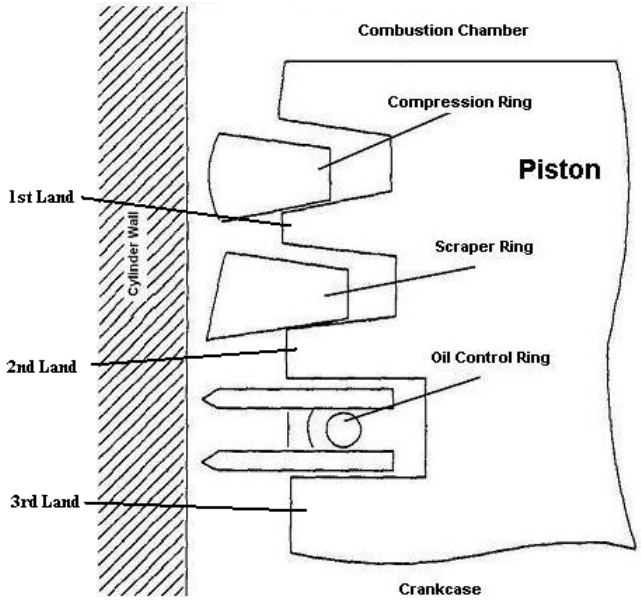

Figure 1: Typical Piston Ring Pack [4].

Blow-by is the condition in which gases flow past the ring-pack from either the combustion chamber to the crankcase or vice versa (reverse blow-by) by means of various leakage paths. As shown in Figure 2, one leakage path is across the face of the ring. It is caused by an absence of lubrication on the cylinder wall resulting from oil evaporation.

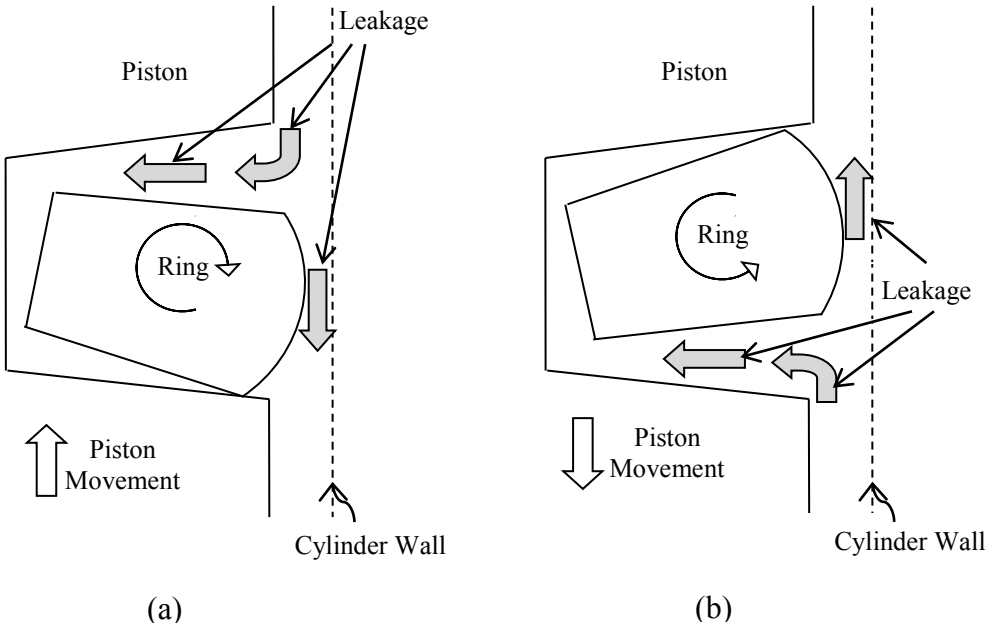

Figure 2: Leakage regions caused by ring twist and oil evaporation during (a) the upstroke of the piston, (b) the downstroke of the piston.

A second leakage path, also shown in Figure 2, occurs as the piston travels within the cylinder. During the piston's upstroke, the ring is twisted in a clockwise direction within its groove as shown in Figure 2a. During the piston's downstroke, the ring is twisted in a counterclockwise direction within its groove as shown in Figure 2b. When the piston changes direction at top or bottom dead center, the ring twist also changes direction. As the piston changes direction and the ring is in mid-twist as shown in Figure 3, the ring doesn't have contact with either wall of its groove allowing gas to flow around and behind the ring.

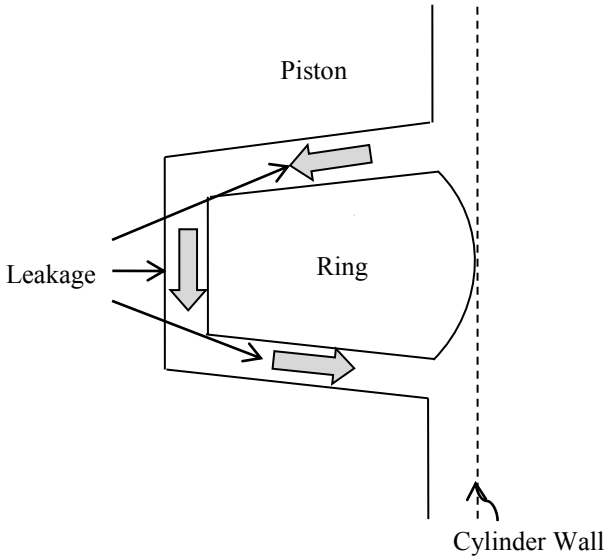

Figure 3: Leakage regions around and behind ring when the piston is at either top or bottom dead center.

The third leakage path is through the end gap of the split ring as shown in Figure 4. Of the leakage paths described, it is the least significant and is only noticeable if the other two paths are sealed [5].

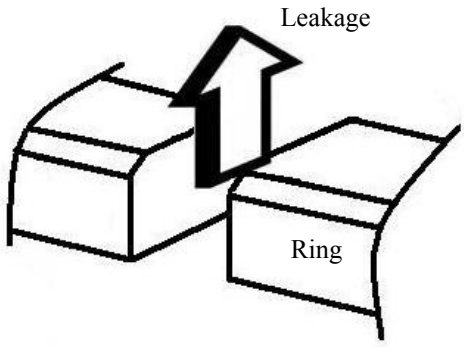

Figure 4: Leakage through the ring end gap.

The direction of the gas flow through the three leakage paths depends upon pressure changes within the cylinder and the direction of the piston's motion. During the upstroke, the pressure in the combustion chamber increases and the gases flow through the various leakage paths toward the crankcase until the piston reaches top dead center.

During combustion, fuel and air are ignited increasing the pressure and temperature and pyrolyzing the oil droplets to form abrasive carbon particles that travel with the burned hydrocarbon gases. The increase in pressure forces the carbon particles and burned hydrocarbon gases to flow through the leakage paths at the ring/piston interface and the ring/cylinder interface toward the crankcase. If blow-by is significant, it's possible for the piston, rings, and cylinder to reach extreme temperatures eventually leading to engine overheat. Furthermore, blow-by carries carbon particles from the combustion chamber to the crankcase, thus contaminating the lubricating oil.

During the downstroke, the pressure in the crankcase increases and the gases flow through the various leakage paths toward the combustion chamber until the piston reaches bottom dead center. This reverse blow-by disturbs the oil film layer on the cylinder wall and entrains oil particles that are carried to the combustion chamber. These oil droplets are then pyrolyzed in the combustion chamber to form abrasive carbon particles and deposits.

When the oil film layer is disturbed, oil ligaments are sheared from the wall and flow through the ring pack forming an aerosol. This methodology of aerosol formation was introduced by Castleman: "A portion of the large mass is caught up by the air stream, being anchored at the other end, is drawn out to a fine ligament. This ligament is quickly cut off by the rapid growth of a dent in its surface, and the detached mass, being quite small, is swiftly drawn up to a spherical drop. The higher the air speed, the finer the ligaments, the shorter their lives, and the smaller the drops formed [6]." In terms of the oil layer and the ring-pack, the mass mentioned by Castleman is an oil globule, the

ligament is a sheared piece of the oil globule, and the air speed is blow-by or reverse blow-by.

In this project a numerical model was developed that accurately describes the formation of aerosols in the ring pack by simulating the mechanisms by which oil globules are broken up, atomized, and entrained in a gas flowing through an orifice. The results of this numerical model are in good agreement with experimental values. Thus, this numerical model gives insight into the parameters that govern oil consumption.

CHAPTER 2

LITERATURE REVIEW

Several attempts have been made to fully explain the oil consumption phenomenon. Most researchers have chosen a specific part or portion of the ring-pack and focused on it. Ting and Meyer were the first researchers to use a computer to predict inter-ring gas pressures by utilizing the orifice and volume method proposed by Eweis in 1935 [7, 8]. Ruddy enhanced the work of Ting and Meyer to predict the gas pressures in a diesel engine ring-pack by including energy loss due to wall friction between the piston and the cylinder wall [7]. Rhode used the information from Ruddy and incorporated the use of mixed lubrication in the friction prediction method [9]. Keriber tried to establish an overall quasi-numeric model applicable for predicting wear and oil consumption as a function of the engine, piston, and ring pack design for certain operating conditions [10]. The same year, Miyachika, of the Mazda Motor Corporation, studied the relationship of the oil consumption to reverse oil blow-by and developed a numerical procedure for optimizing ring gap clearance and volume for acceptable oil consumption [11].

Burnett was the first to research oil consumption from the emissions standpoint by constructing an enhanced mechanistic model for oil transport through the ringpack utilizing correlations for piston deposit formations also known as carbon build-up [4]. Hoult considered blow-by as a mechanism of fluid dynamics. As the oil is scraped by the scraper ring off the cylinder wall, it puddles directly below the top ring and is blown through the top ring gap and into the combustion chamber during the downstroke [12]. In 1996, De Petris defined two stages of oil consumption as the evaporation of oil and its subsequent combustion [13]. De Petris also suggested that the blow-by could also be

creating as oil aerosol. Tian, Noorzij, Wong, and Heywood are the first individuals to couple ring-pack dynamics, gas flows, and piston design to establish a singular gas-flow model that incorporated an oil transport function on the piston lands [5]. The same individuals, and Yilmaz years later, studied oil consumption in an operating engine with varying speeds and loads. Their work characterized the different oil consumption sources by combining measurements and physics based modeling [14].

Cho and Tian modeled engine oil vaporization and oil transport in the ring-pack by looking into the composition of lubricating oil and its mechanical and chemical behavior [15]. Chun wrote a computer algorithm to predict oil consumption in advance to measurements on a selected engine [16]. Day reported on the efforts of Dunaevsky and McCormick to characterize oil consumption in relation to cylinder distortion, oil transport mechanisms in the ring-pack, and the likelihood of aerosol formation in the ringpack [17].

The collapse of a liquid column is the first reference to atomization that is highly acknowledged. Plateau showed that a round cylindrical liquid column, whose length exceeds it circumference, is unstable and will therefore, eventually collapse and atomize under the influence of any disturbance, even one of arbitrarily small amplitude [18]. Castleman applied the theory proposed by Plateau and described the atomization of a liquid as it travels through conditions similar to that of an automotive carburetor [6]. Triebnigg took the theory of liquid atomization by Castleman and proposed a new theory on droplet breakup by introducing and accounting for both surface tension of the liquid and air resistance [19]. After the introduction of Triebnigg's theory, Weber introduced the most complete theoretical and mathematical basis to date on the theory of low jet

velocity sprays [20]. In his work, Weber introduced the Weber Number, which is the ratio of the inertial forces to the surface tension. After the introduction of the Weber number, Hinze used Weber's surface tension data and the Weber number to determine the critical speeds and sizes of liquid globules in a gas stream [21]. Morrell used similar information and investigated the critical conditions for droplet and jet shattering [22]. Ingebo investigated the atomization of a single liquid jet injected into a high velocity, high-pressure airflow [23]. Ingebo was the first researcher to publish mean droplet sizes for optimum evaporation rates after combustion using an optical measuring method.

Reitz revisited the automotive application of aerosols and investigated the breakup of high speed liquid injected through a circular nozzle into a stagnant gas [24]. O'Rourke and Amsden disagreed with Reitz's theory and developed their own theory called the TAB method (Taylor Analogy Breakup) which relates the breakup process to a spring-mass damper system. In the TAB method, the restoring force of the spring is analogous to the surface tension, and the dampening is analogous to the viscosity, while the gas aerodynamics are analogous to the external driving forces [25]. Lastly, Diego used orifice theory and carburetor design coupled with computational fluid dynamics software to obtain the mixing length and fuel droplet size for the optimization of the air/fuel mixture for a carbureted small engine [26]

As seen from the literature review, a significant amount of research has been conducted and published concerning oil consumption and atomization. However, only De Petris [13] and Dunaevsky, and McCormick [17] of CK Engineering have considered the formation of aerosols in the ring-pack. McCormick's experiments have focused on creating, controlling, and measuring an aerosol in a closed system.

CHAPTER 3

CK ENGINEERING

H. McCormick is principle owner of CK Engineering Inc., a mechanical engineering design and consulting company that serves the automotive and machinery industry [27]. They specialize in piston and ring conformity by offering expertise in the areas of measuring, testing, and simulation. They have over 20 years' experience in piston and ring design and been issued 37 patents. In this project, CK Engineering provided the experimental work that preceding the theoretical modeling efforts.

Early Experimental Work

CK Engineering's first attempts at understanding aerosol formation in the ring-pack utilized a single cylinder air compressor. A bracket was constructed to hold a paper towel at various distances from a machined hole in the cylinder wall as shown in Figure 5.

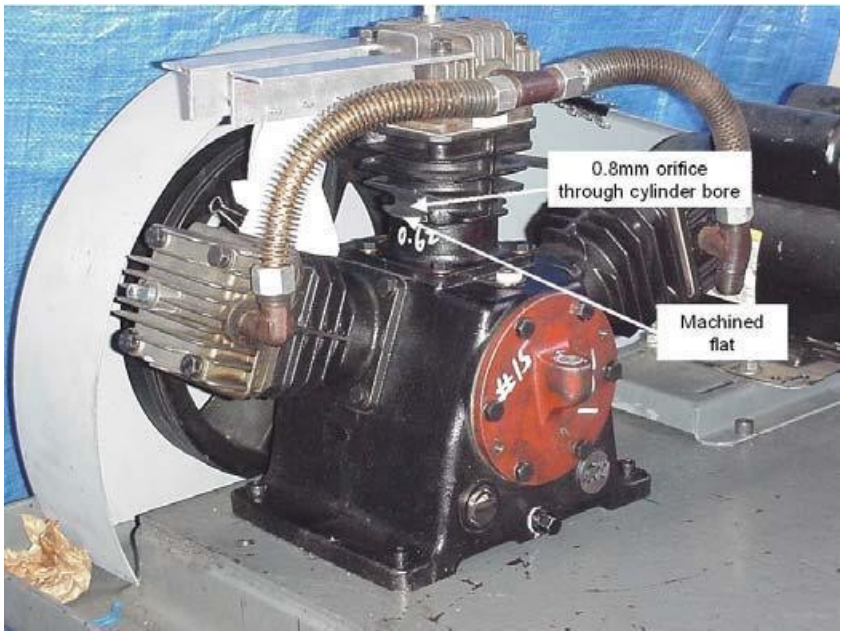

Figure 5: Paper Towel Attached to Air Compressor.

Oil mist deposits were collected at measured distances of 25 mm., 50 mm., and 75 mm., as seen in Figure 6. These three tests indicated that an oil mist aerosol was being formed in the ring-pack.

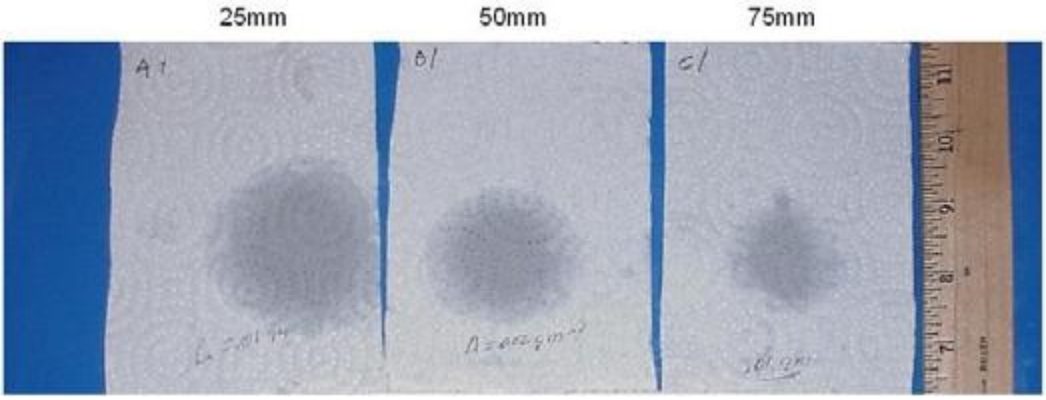

Figure 6: Paper Towel Test Samples.

This research was expanded by creating a single piston/cylinder liner that could be instrumented to measure the pressures on the second and third lands, the rate of supply gas and oil entering at the third land, and the concentration of the aerosol mixture leaking from the top compression ring moving toward the combustion chamber. See Figure 7.

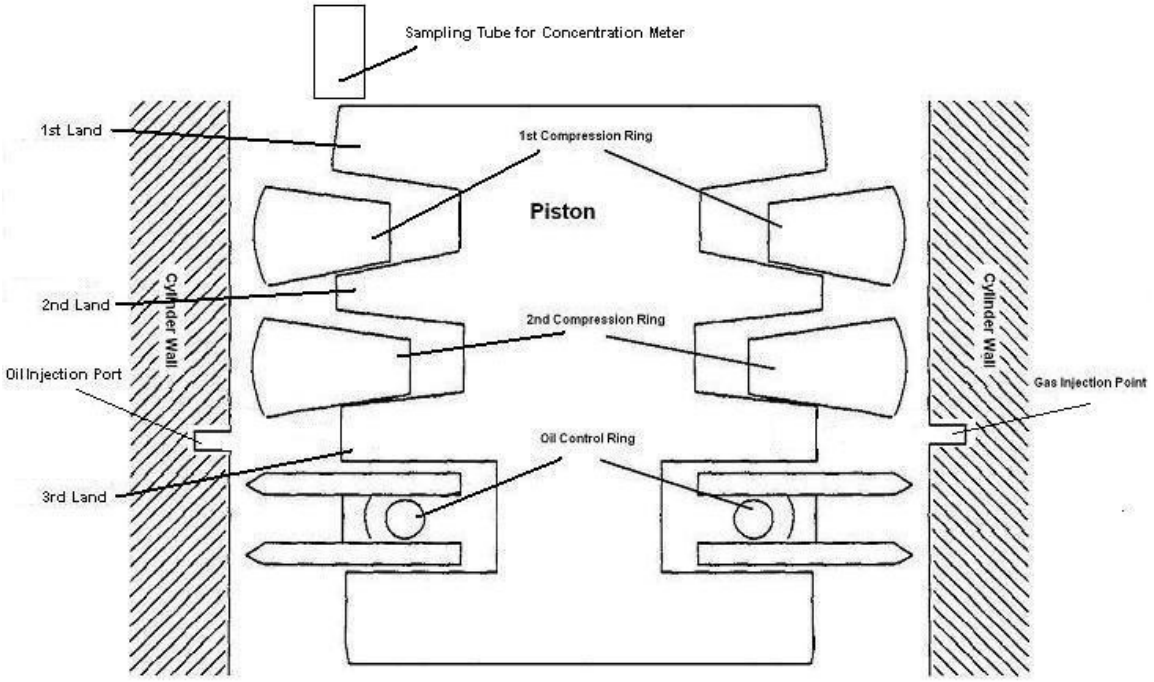

Figure 7: Piston/Cylinder Test Schematic [4].

The oil and gas was injected at the third land to allow for monitoring of the gas pressures and oil feed rate as they mixed and flowed to the second land. After flowing to the second land, the aerosol flows through the second compression ring gap and into the second land and then out through the ring gap of the first compression ring. Immediately above the top surface of the first land, a concentration meter sampled the aerosol concentration over a specific time.

The results for the first tests were inconclusive due to leakage. This leakage was investigated and discovered when the fixture was leak tested by applying soapy water to the top of the piston. As Figure 8 shows, gas, oil, and soap bubbled from and on top of the piston.

Figure 8: Gas, oil, and soap bubbling from the top of the piston at the piston/cylinder interface [17].

This leakage was minimized by sealing the interface of the cylinder and piston using cylinder head gasket sealant. After the cylinder and piston were sealed, the concentration meter data became consistent. See Figure 9.

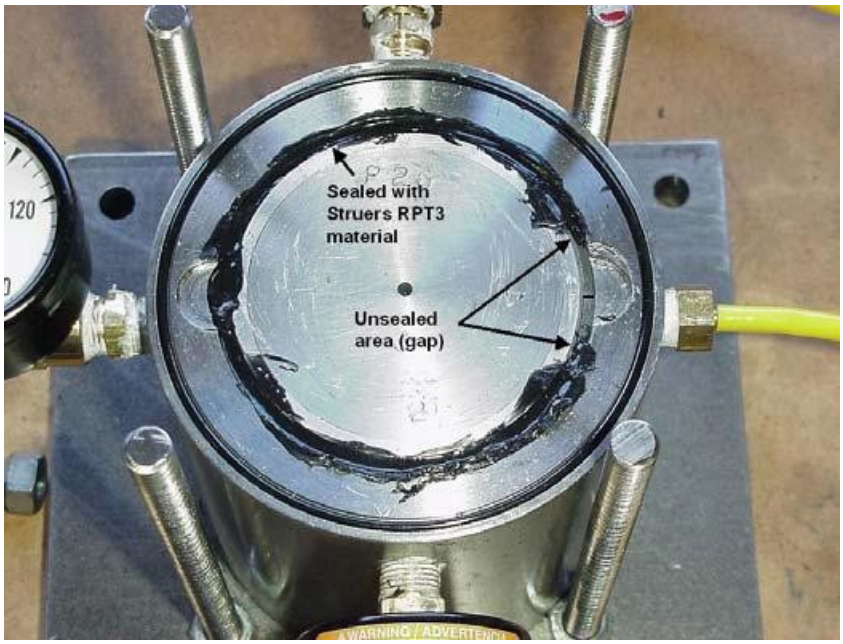

Figure 9: Piston cylinder interface sealed with cylinder head gasket sealant [17].

A test plan was designed to establish the influence of seven major factors on the creation of aerosols in the ring-pack. See Table 1.

Table 1: DOE Factors Investigated

Influence Factors for Aerosol
oil type (chemistry)
3rd land pressure
top ring end clearance
2nd ring end clearance
top/2nd ring end gap alignment
oil injection location with respect to 2nd ring gap
oil injection rate, 3rd land

The results were analyzed and it was found that the major contributors affecting the flow rate of the aerosol were the top ring end clearance, the alignment of the end gaps of the top and second rings, and the 3rd land pressure. The major factors affecting aerosol concentration were the oil injection location, oil type, and the alignment of the end gaps of the top and second rings.

Current Experimental Work

The factors affecting the aerosol concentration in the ring pack proved to be interesting, especially when considering that the test fixture only represented a portion of the factors that influence oil consumption from reverse blow-by. However, it did provide the basis for building another test fixture to test the importance of those factors. The new fixture consists of an orifice, which represents a combination of the ring gaps and clearances. The orifice is positioned at the bottom of a cylindrical orifice chamber which is pressurized with nitrogen to maintain a pressure differential across the orifice that represents the pressure differential experienced between the crankcase and combustion chamber. The orifice chamber is mounted within an oven that is set at specified

temperatures to represent the operating temperatures of typical internal combustion engines. A syringe pump is used to accurately meter the oil feed rate into the orifice chamber while a gas regulator is used to maintain the constant nitrogen pressure within the orifice chamber. This test fixture is shown in Figures 10 and 11.

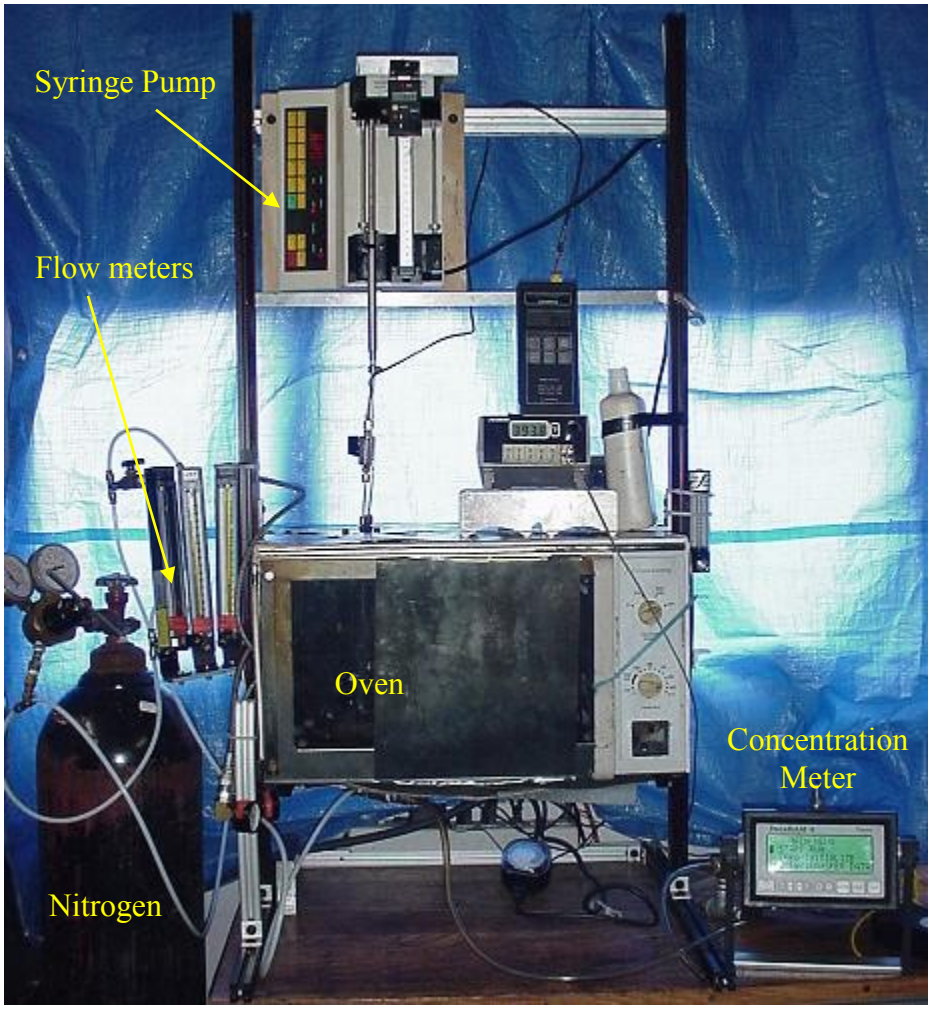

Figure 10: CK Engineering test fixture utilizing an orifice and oven [28].

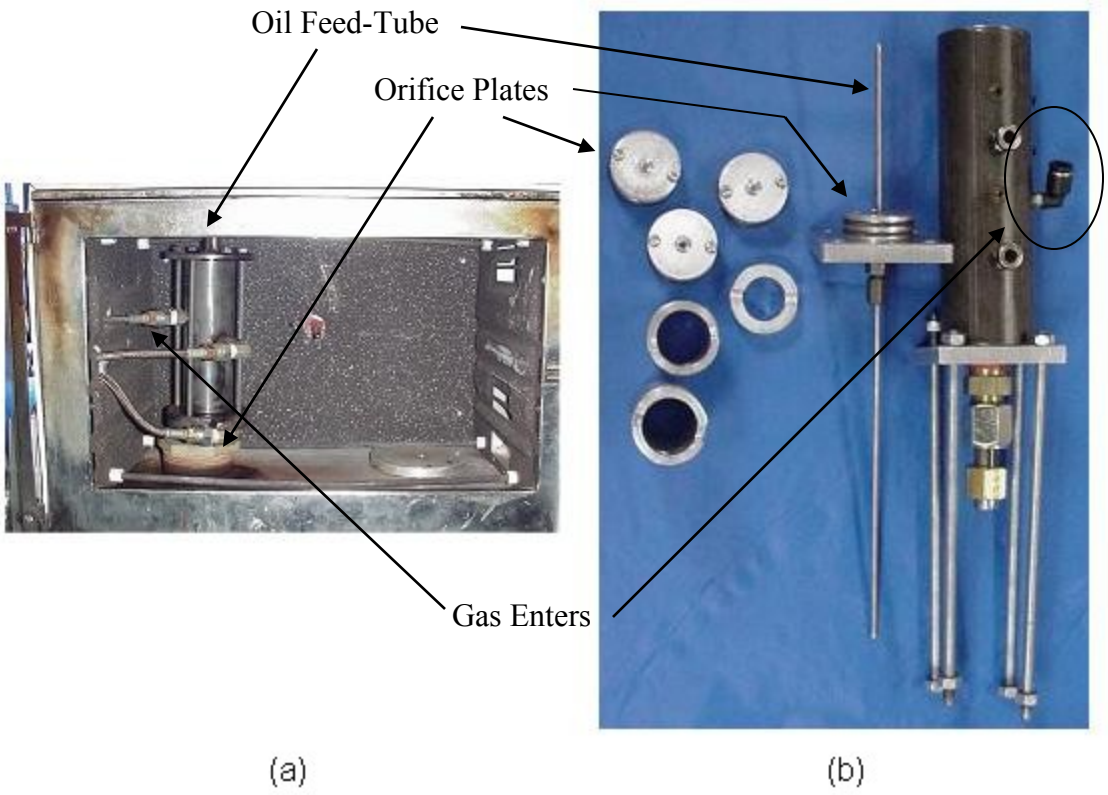

Figure 11: (a) Orifice chamber inside oven. (b) Orifice chamber, exploded view [28].

CK Engineering uses the following procedure to ensure repeatability. First, the oven is set at a predetermined temperature verified by a thermocouple. After 20 minutes, the nitrogen gas is turned on and allowed to flow freely for three to five minutes. The concentration meter is also turned on, allowing for steady state conditions to occur. The motor driven syringe pump is then adequately filled with the test oil, turned on, and set to deliver a specific oil flow rate. The thermocouple at the orifice is checked to ensure that it is in good working order. See Table 2 for typical oil and gas flow rate ranges.

Table 2: Input variables for experiment.

Input Variables and Ranges	
Oil Feed-rate (mL/hr.)	0.5- 1.0
Gas Flow rate (L/min.)	0.09 - 0.59
Dilution Gas Flow rate (L/min.)	0 - 45

The input variables shown in Table 2 are maintained within acceptable limits to simulate the conditions found in a reciprocating piston environment. In these test cases, the pressure differential across the orifice is maintained at 100 psig and the room temperature is held constant at 291.78 K (~ 65.8 °F).

After these preliminary steps are completed, testing is begun. The oil is fed by the syringe pump into the orifice chamber. The nitrogen and oil flows mix within the orifice chamber and are carried through the orifice creating an aerosol. The aerosol leaves the orifice chamber and enters the concentration meter which records and stores the aerosol concentration and temperature. These values are then exported to a computer for analyzing.

CK Engineering uses a DataRAM 4 concentration meter to measure the oil aerosol concentration. **Error! Reference source not found.** lists the sample rate, concentration range, and particle size range for the DataRAM 4 concentration meter calibrated for clean air. The DataRAM4 is

capable of measuring a maximum concentration of 400 mg/m^3, for clean air containing solid particles of dust, smoke, fumes, or mists as shown in **Error! Reference source not found.**. However, the experiments utilize nitrogen instead of air and heated oil instead of solid particles. Therefore, the concentration meter was re-calibrated by the manufacturer to measure oil aerosols in nitrogen with concentrations ranging from 200 - 900 mg/m^3.

Table 3: Thermo Electron Corporations DataRAM 4 Particulate Monitor Specifications calibrated for clean air.

DataRAM 4 Features	Specifications
Sample Rate (s)	1- 60
Concentration Range (mg/m^3)	0.0001- 400
Particle Size Range (μm)	0.04 - 4

CHAPTER 4

THEORETICAL MODEL FOR THE TEST FIXTURE

In this current project a theoretical physics-based numerical model was developed to simulate the aerosol formation in the experimental apparatus currently being used by CK Engineering. Figure 12 shows a schematic of the CK Engineering aerosol experimental setup used as a basis to develop the current theoretical model of aerosol formation. In the theoretical model, the oil feed rate is an input value set to match the experimental value used by CK Engineering. The oil is supplied to the orifice chamber through the oil feed tube shown in Figure 12. Oil is entrained in a gas flow which then passes through a small circular orifice, resulting in an aerosol that is measured by a concentration meter. Location 1 is where the nitrogen gas enters the closed system. The nitrogen gas travels downward toward Location 2 where the nitrogen gas starts to interact with the oil at the top of the orifice plate. Location 3 is where the oil and gas combine and pass through the orifice plate generating an aerosol. Location 4 is where dilution gas is added to the aerosol to dilute the mixture so that its concentration is within the limits given in concentration meter specifications.

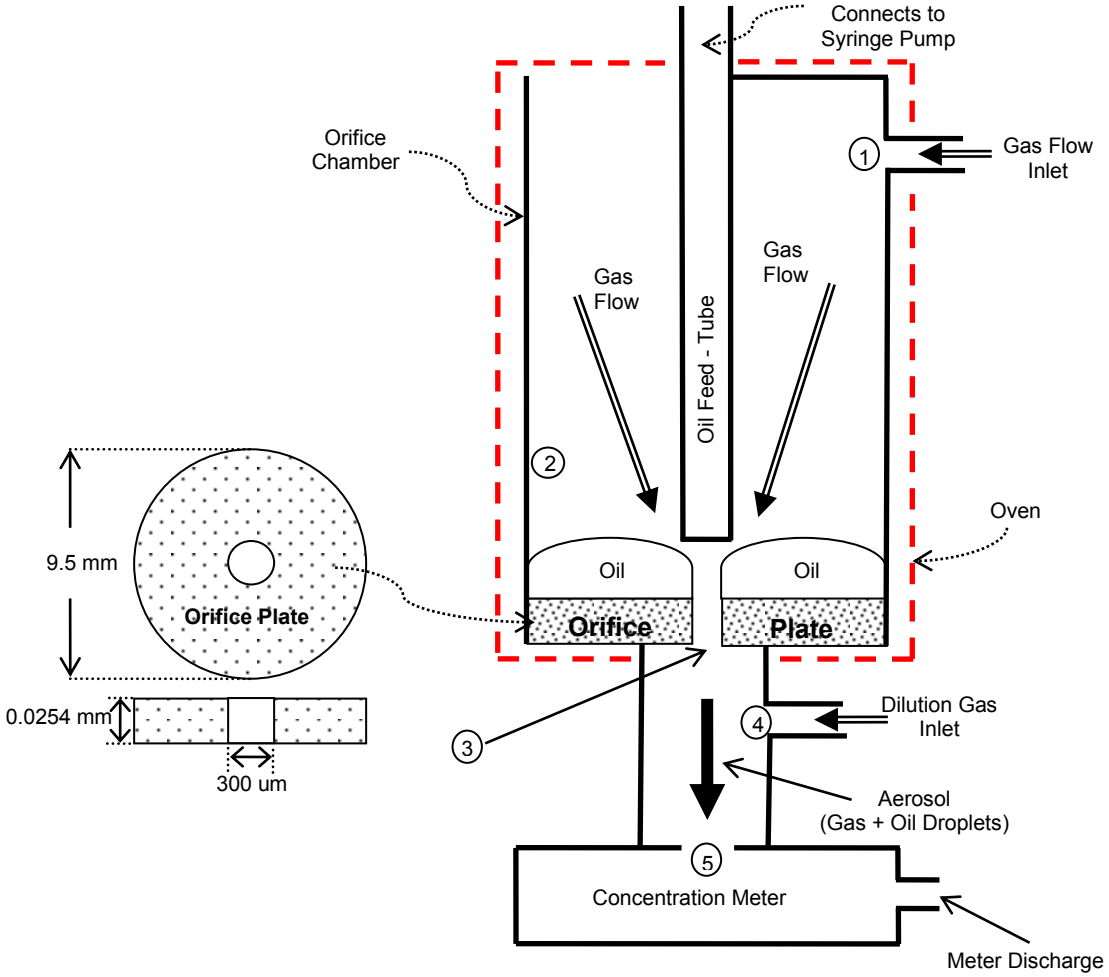

Figure 12: Orifice plate and the test model schematic with gas flow locations noted.

Gas Theory Formulation

The volumetric flow rate of the nitrogen gas entering the test fixture at Location 1 is measured by a volumetric flowmeter. The temperature at Location 1 is room temperature. The pressure at Location 1 is measured via a pressure tap on the orifice chamber. This pressure is maintained by the pressure regulator on the gas supply. The temperature at Location 2 is measured by a thermocouple and the pressure at Location 2 is the same as the pressure at Location 1. The pressure at Location 3 is atmospheric and the temperature at Location 3 is assumed to be the same as at Location 2. The volumetric flow rate of the dilution gas at Location 4 is measured by a volumetric flowmeter. The pressure and temperature at Location 4 are atmospheric pressure and

room temperature. The temperature at Location 5 is measured by a temperature sensor in the concentration meter at atmospheric pressure conditions. See

Table 4 for a summary of the values at Locations 1, 2, 3, 4, and 5.

Table 4: Summary table for gas flow calculations

	State Number				
	1	2	3	4	5
Volumetric Flow rate (m^3/s)	●	—	●●	●	●●
Temperature (K)	●	●	●	●	●
Pressure (Pa)	●	●	●	●	●
Velocity (m/s)	—	—	●●	—	—

Measured Value ● Calculated Value ●● Value not Measured nor Calculated —

The measured values listed in

Table 4 are required to find the calculated values. By using the continuity Equation at Locations 1, 2, and 3 the following expression can be written for the respective mass flows, $\dot{m}$.

$$\dot{m}_1 = \dot{n}_2 = \dot{n}_3 \tag{1}$$

The Equation for the mass flow rate is written as

$$\dot{m} = \rho Q = \rho AV \tag{2}$$

where ρ is the density of the gas, and Q is the volumetric flow described in terms of the cross sectional area, A, and velocity, V.

The density, ρ, seen in Equation 2 is given by the ideal gas law which states that when the pressure, P, and temperature, T, are known, and combined with the universal gas constant R, the density, ρ, can be calculated.

$$\rho = \frac{P}{RT} \tag{3}$$

By combining Equations 1, 2, and, 3, an equation for the velocity at Location 3 can be derived utilizing $T_2 = T_3$.

$$\dot{m}_1 = \dot{m}_3 \tag{4}$$

Substituting Equations 1, 2, and, 3 for $\dot{m}$:

$$\frac{P_1}{RT_1} Q_1 = \frac{P_3}{RT_3} A_3 V_3 \tag{5}$$

Solving for V_3 with $T_2 = T_3$:

$$V_3 = \left(\frac{P_1}{P_3} \right) \left(\frac{T_2}{T_1} \right) \left(\frac{Q_1}{A_3} \right) \tag{6}$$

Similarly the volumetric flow at Location 3 is calculated as

$$Q_3 = A_3 V_3 = \left(\frac{P_1}{P_3} \right) \left(\frac{T_2}{T_1} \right) Q_1 \tag{7}$$

The mass flow rate at Location 5, $\dot{m}_5$, is found by adding the mass flow rates at Locations 3 and 4.

$$\dot{m}_5 = \dot{m}_3 + \dot{m}_4 \tag{8}$$

By combining Equations 2, 3, and 8, an expression is derived relating the volumetric flow rate at Location 5, Q_5, to the volumetric flow rate at Locations 3, Q_3, and 4, Q_4.

$$\frac{P_5}{RT_5} Q_5 = \frac{P_3}{RT_3} Q_3 + \frac{P_4}{RT_4} Q_4 \tag{9}$$

Since $P_5 = P_3 = P_4$, Equation 9, can be simplified to:

$$Q_5 = \left(\frac{Q_3}{T_2} + \frac{Q_4}{T_4} \right) T_5 \tag{10}$$

Oil Theory Formulation

Consider a globule of oil sitting on a surface near an edge as shown in Figure 13a. Suddenly, gas starts to flow perpendicularly past the edge and adjacent to the globule of oil. The gas flow creates suction and pulls on the globule until a ligament is ripped away from the larger globule by overcoming the surface tension and viscous effects of the oil globule as seen in Figure 13b.

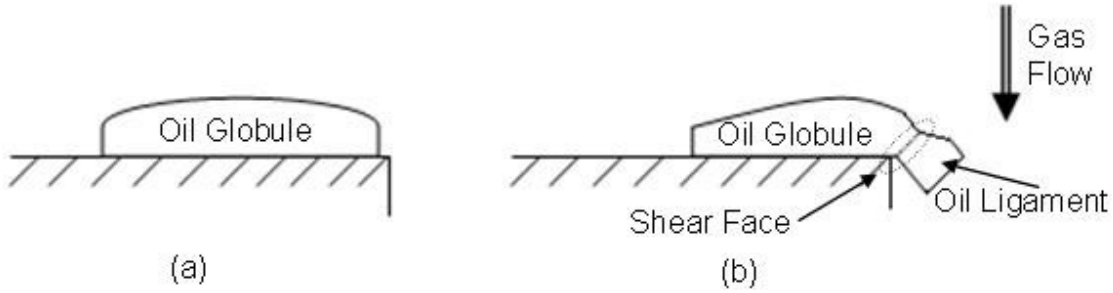

Figure 13: (a) Oil Globule on a hard surface. (b) Oil Globule sheared by gas flow

The stresses caused on the shear surface by the ligament ripping are similar to those seen in orthogonal machining processes. In orthogonal machining, the prevalent cutting action creates both a normal and shear stress on the face of the material being removed as seen in Figure 14a. In Figure 14b, the normal force, F_N, results from the normal stress associated with the fluid's surface tension while the parallel force, F_V, results from the shear stress associated with the viscosity of the fluid. The pressure force, F_p is the force required to shear the oil globule into an oil ligament with mass, m_{LIG}.

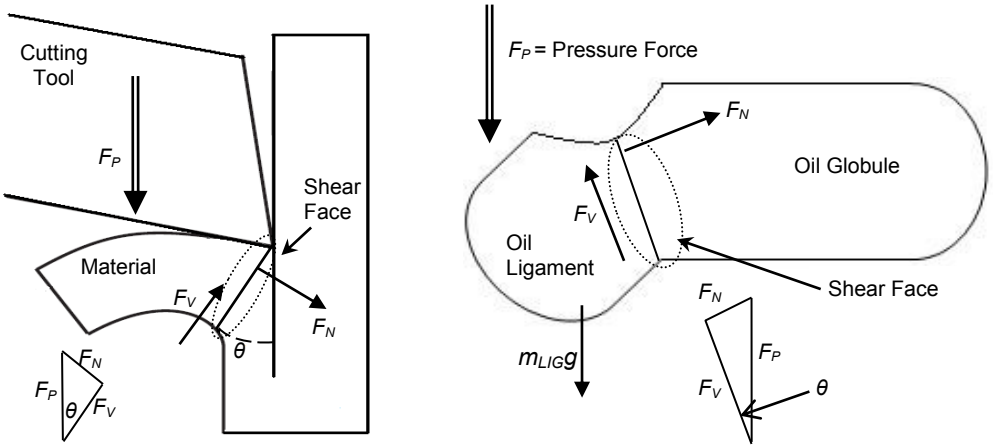

(a) (b)

Figure 14: (a) Orthogonal machining. (b) Free-body diagram of shearing oil globule.

The summations of the parallel and perpendicular forces with respect to the shear face produce the following equations for F_V and F_N.

$$\begin{aligned} F_V &= F_P \cos\theta + n_{LIG}\, g \cos\theta \\ F_N &= F_P \sin\theta + n_{LIG}\, g \sin\theta \end{aligned} \tag{11}$$

By subtracting F_N from F_V an equation is expressed relating the surface tension and viscosity.

$$\frac{F_V}{\cos\theta} - \frac{F_N}{\sin\theta} = \,) \tag{12}$$

The surface tension, σ_S, related to the normal force F_N, acts on the outermost edge of the oil ligament. This is shown in Figure 15a, which depicts the same oil globule as shown in Figure 14b, but with the surface tension locations labeled.

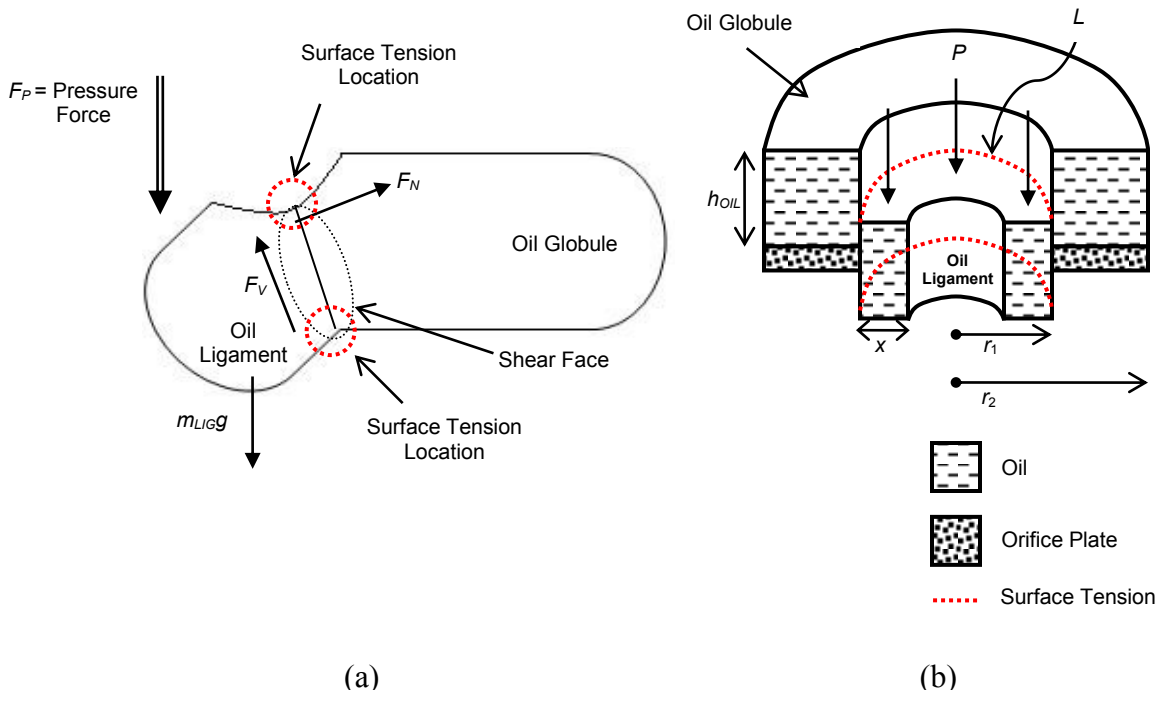

Figure 15: (a) Oil globule and ligament with reference to surface tension locations (b) Oil ring sitting upon orifice plate.

Figure 15b shows the ring shaped oil globule sitting upon the round orifice plate with an oil ligament being sheared.

Now that the surface tension locations have been shown, the relationship between the normal force F_N, and the surface tension, σ_S, is introduced:

$$\sigma_s = \frac{F_N}{L} \tag{13}$$

The circumferential length, L, is depicted in Figure 15b and defined by Equation 14. It represents where the normal force acts, that is, on the outermost circumference of the oil ring with radius, r_1.

$$L = 2\pi r_1 \tag{14}$$

By combining Equations 13 and 14, an equation for normal force, F_N, is expressed in terms of the surface tension, σ_S,

$$F_N = 2\sigma_s(2\pi r_1) \tag{15}$$

The surface tension acts at only two locations; the top and bottom. The locations are depicted in Figure 15a and represented mathematically in Equation 15 by the number two. The surface tension values utilized for this study are based upon the temperature at Location 2, T_2, as seen in Figure 12. See Graph 1 for the graphical representation of the linear relationship between surface tension and temperature. Table 5 gives the equations shown in Graph 1 describing the surface tension for four different oils as functions of temperature. In this project, the Syntholube surface tension equation is utilized.

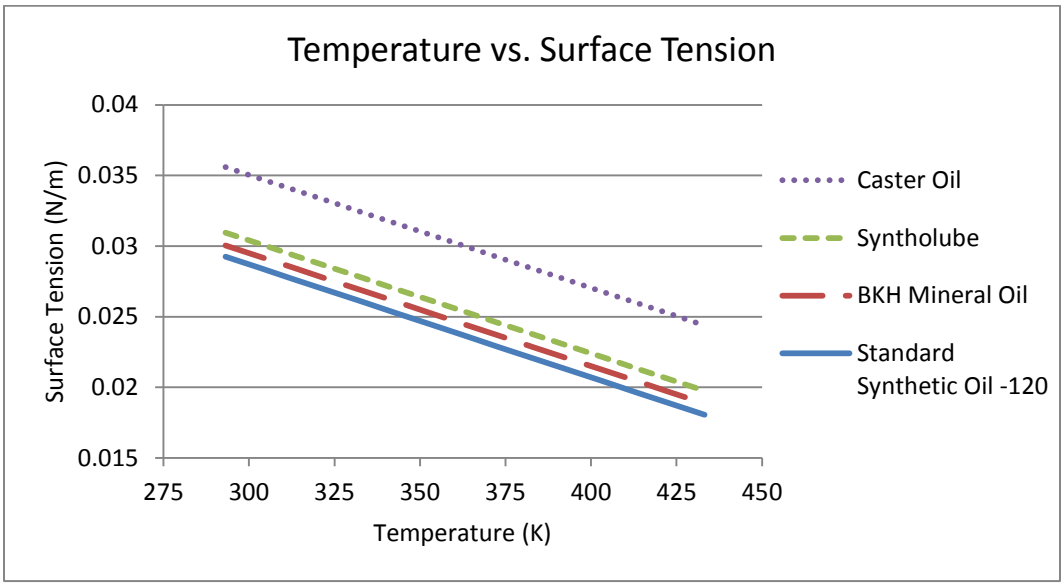

Graph 1: Temperature vs. Surface Tension for four types of oils. *Reproduced from NACA Technical Note 2030* [29].

Table 5: Surface Tension equations for four specific oils based upon temperature.

Oil	Surface Tension (σ_S) (N/m)
Castor Oil	-0.00007857 · (Temp, K) + 0.059
Syntholube	-0.00007857 · (Temp , K) + 0.0544
Mineral Oil	-0.00008 · (Temp, K) + 0.0535
Synthetic Oil-120	-0.00008 · (Temp, K) + 0.052

The normal force, F_N has been derived in Equation 15 , an expression for the shear force, F_V, needs to be introduced.

The shear force, F_V, shown in Figure 15a is the viscosity component of the shearing of the ligament. The shearing of the ligament is expressed in terms of the viscosity, μ, the strain rate, dE/dt, and the area, A, by the following equation:

$$F_V = \mu \left(\frac{dE}{dt} \right) A \tag{16}$$

The viscosity, μ, is a function of the temperature and the rate of strain. The rates of strain used in this model are of typical values found in a reciprocating piston environment. The viscosity as a function of strain rate and temperature was measured by an independent lab that specializes in measuring lubrication properties and rheology. The viscosity data was furnished to us by CK Engineering [30]. See Graph 2 for a plot of dynamic viscosity as a function of strain rate and temperature.

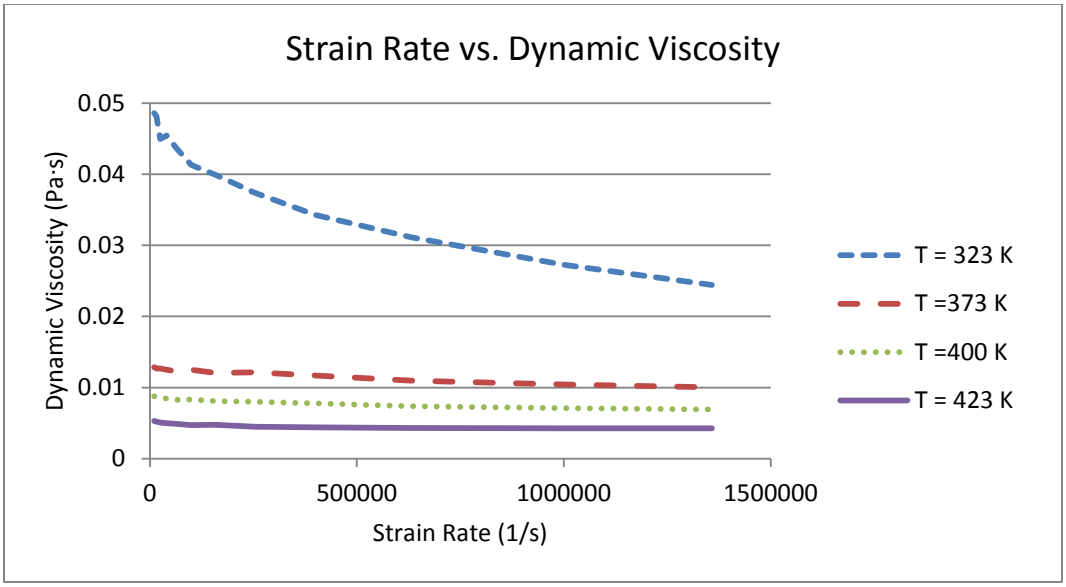

Graph 2: Strain Rate vs. Dynamic Viscosity for the same oil at four different temperatures.

Equation 17 describes the dependence of the viscosity of the oil upon the strain rate and temperature. Equation 17 was derived by fitting the data shown in Graph 2.

Table 6 gives the coefficients used in Equation 17 corresponding to each of the four temperatures.

$$\mu = \frac{1}{a + b\left(\frac{dE}{dt}\right)^{c}} \tag{17}$$

Table 6: Coefficients relating viscosity to temperature.

Temperature (K)	Coefficients		
	a	*b*	*c*
323	20.005	0.002	0.648
373	78.052	0.0003	0.801
400	111.961	0.0285	0.4997
423	6.739	114.431	0.05

From materials science, we know that the strain rate is defined as follows:

$$\left(\frac{dE}{dt}\right) = \left(\frac{\Delta x/x}{\Delta t}\right) = \frac{d}{dt}\left(\frac{\Delta x}{x}\right) = \frac{dx}{dt}\left(\frac{1}{x}\right) \tag{18}$$

where dx/dt represents the velocity of deformation in the vertical direction and x represents the thickness of the ligament as shown in Figure 15b. Utilizing this information, the strain rate is written in terms of the gas flow at Location 3, V_3, shown in Figure 12 and the ligament thickness x, as seen in Equation 19 and depicted in Figure 15b.

$$\frac{dE}{dt} = \frac{V_3}{x} \tag{19}$$

The first two variables of Equation 16, the viscosity and strain rate, have been derived. The last component, the area upon which the shear stress acts, A, is given in Equation 20 in terms of the height and the circumference of the oil ligament, h_{OIL}, and $2\pi r_1$, as depicted in Figure 15b.

$$A = 2\pi r_1 h_{OIL} \tag{20}$$

Figure 16 depicts the oil globule as it appears on top of the orifice plate.

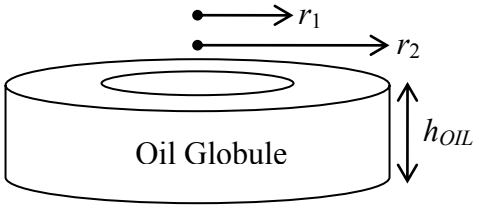

Figure 16: Oil globule referencing radius and height

Equation 21 defines the height of oil globule, h_{OIL}, in terms of the inner and outer radii of the oil globule, r_1 and r_2, respectively, the density of the oil, ρ_{oil}, and the total mass of the oil globule, mT.

Table 7 gives for the density of the oil for representative temperature ranges.

$$h_{OIL} = \frac{mT}{\rho_{oil}\pi(r_2^2 - r_1^2)} \tag{21}$$

Table 7: Oil densities for temperature ranges [31-33].

Temperature Range (K)	Oil Density, ρ_{oil} (kg/m^3)
$T_2 < 420$	817
$460 > T_2 \geq 420$	800
$T_2 \geq 460$	790

Combining Equations 12, 15, 16, 17, 19, and 20 to form a single expression, seen in Equation 22, which relates the temperature, viscosity, surface tension, thickness, and the rate of strain for an oil ligament being sheared from a globule.

$$\frac{1}{a + b\left(\frac{dE}{dt}\right)^c}\left(\frac{V_3}{x}\right)\left(\frac{h_{OIL}}{\cos\theta}\right) - \frac{2\sigma_S}{\sin\theta} = 0 \tag{22}$$

Equation 22 can be algebraically manipulated, so that an iterative method can be utilized to solve for the strain rate, $dE/dt = V_3/x$.

Since V_3 has been calculated via Equation 6, once the strain rate, V_3/x, is found from Equation 22, the thickness of the oil ligament, x, can be calculated. The thickness of the oil ligament, x, can then be used to find the volume and mass of the oil ligament by Equations 23 and 24. See Figure 15b.

$$V_{LIG} = \pi h_{OIL}(2r_1 x - x^2) \tag{23}$$

$$m_{LIG} = \rho_{OIL}\pi h_{OIL}(2r_1 x - x^2) \tag{24}$$

Now that an expression for the mass of the ligament has been derived, m_{LIG}, the amount of time, Δt, required for the ligament to travel x distance (ligament thickness)

needs to be derived. This time is then utilized as a time step for the progression of the aerosol model.

In Figure 17 the free body diagram for an oil globule on top of an orifice plate is shown. The forces F_1, F_2, and F_3 are shown with reference to an oil ligament of thickness, x.

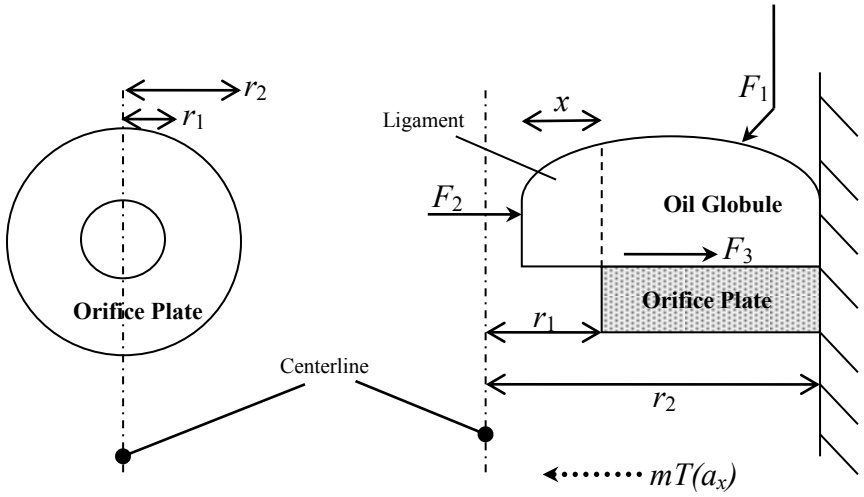

Figure 17: Free-body diagram of orifice plate with oil ligament shearing

F_1 represents the gas pressure force acting on the outer most circumference of the oil with F_2 representing the gas pressure force acting on the inner most circumference. See Equations 25 and 26.

$$F_1 = P_2 \left(2\pi r_2 h_{OIL}\right) \tag{25}$$

$$F_2 = P_2 \left(2\pi r_1 h_{OIL}\right) \tag{26}$$

F_3 is the viscous force felt by the boundary between the orifice plate and the oil globule, represented by Equation 27.

$$F_3 = \mu \left(\frac{dU_\infty}{dy}\right) A \tag{27}$$

The viscosity, μ, is found from Equation 17, the height of the oil globule, h_{OIL} is seen as dy in Figure 18, and calculated from Equation 21. U_∞ is the velocity of the moving globule approximated by Equation 28.

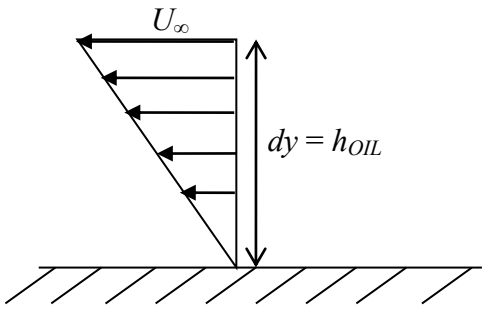

Figure 18: Velocity profile of oil globule.

$$U_\infty = \frac{x}{\Delta} \tag{28}$$

The velocity gradient, dU_∞/dy, is approximated by Equation 29. See Figure 18.

$$\frac{dU_\infty}{dy} = \frac{x/\Delta}{h_{OIL}} \tag{29}$$

The surface area, A, is found from Equation 30.

$$A = \pi(r_2^2 - r_1^2) \tag{30}$$

By combining Equations 27, 28, 29 and 30 a single equation for F_3 is derived.

$$F_3 = \frac{\mu}{h_{OIL}}\left(\frac{x}{\Delta}\right)\pi(r_2^2 - r_1^2) \tag{31}$$

Expressions are now known for all the forces, F_1, F_2, and F_3, as shown in Figure 17. These forces can be summed in the horizontal direction to derive an expression for Δt.

$$\sum F_x = -ma_x \tag{32}$$

Combining Equations 25, 26, 31, and 32 yields an equation that relates the oil height, h_{OIL}, to the total mass of the oil globule, mT, its acceleration, a_x, and the oil ligament thickness, x.

$$P_2(2\pi h_{OIL})(r_1 - r_2) + \frac{\mu}{h_{OIL}}\left(\frac{x}{\Delta}\right)\pi(r_2^2 - r_1^2) = -mT\,a_x \tag{33}$$

The acceleration, a_x, is approximated by

$$a_x = \frac{x}{\Delta t^2} \tag{34}$$

By combining Equations 33 and 34, the expression shown in Equation 35 is found that relates all three forces, F_1, F_2, and F_3 to the time, Δt, it takes for the ligament to grow to length, x.

$$P_2(2\pi h_{OIL})(r_1 - r_2) + \frac{\mu}{h_{OIL}}\left(\frac{x}{\Delta t}\right)\pi(r_2^2 - r_1^2) = -mT\left(\frac{x}{\Delta t^2}\right) \tag{35}$$

Since Equation 35 is a quadratic equation, the quadratic formula is utilized to solve for the time, Δt.

All the equations needed to solve for the concentration of the aerosol have now been derived. The equation for calculating oil aerosol concentration is seen as

$$concentration = \frac{m_{LIG}}{Q_5\,\Delta t} \tag{36}$$

where the mass of the ligament, m_{LIG} is found from Equation 24, the total volumetric flow at the concentration meter, Q_5, is found from Equation 10, and the time, Δt, required for the ligament to grow to x distance, from Equation 35.

A Further Constraint

At the beginning of a simulation, the total mass of the oil globule, mT, and the height of the oil globule, h_{OIL}, are both zero. During a time step, Δt, the total mass of the oil globule, mT, is both increased according to the oil feed rate and decreased according to the mass of the ligament that is sheared off during the time step. The height of the oil globule, h_{OIL}, is then calculated using Equation 21.

As oil is fed into the orifice chamber over several time steps, both the total mass of the oil globule, mT, and the height of the oil globule, h_{OIL}, increase until the rate of mass removed due to the ligament shearing equals the oil feed rate. However, the height of the oil globule, h_{OIL}, is also limited by the maximum oil globule height, h_{MAX}.

This maximum oil globule height, h_{MAX}, is determined by considering the oil globule as a sessile or sitting droplet as shown in Figure 19a. In Figure 19b the oil globule is cut at the centerline and the internal forces F_4 and F_5 are depicted.

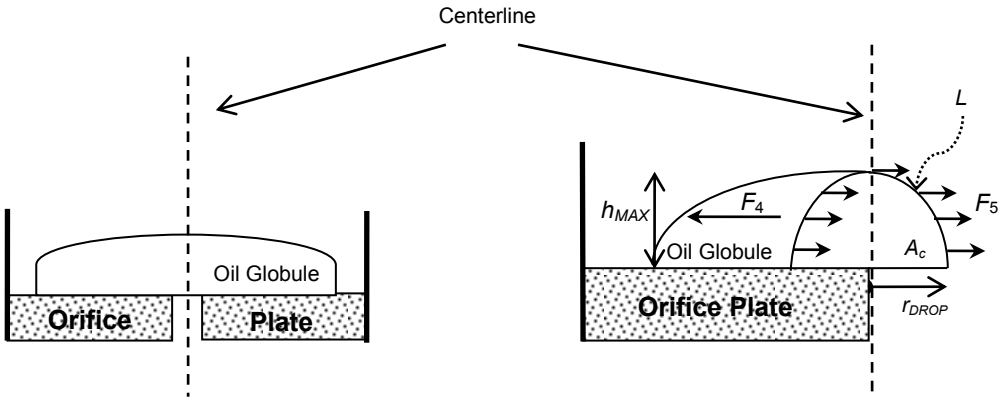

Figure 19: (a) Oil droplet sitting on orifice plate. (b) Free-body diagram of oil globule.

Summing the forces in the horizontal direction as seen in Figure 19b, yields an expression relating the internal pressure force of the oil globule, F_4, to the surface tension force, F_5.

$$\sum F_{HORZ} = 0 \tag{37}$$

$$F_4 = F_5 \tag{38}$$

The internal pressure force of the oil globule, F_4, is found from

$$F_4 = P_I A_C \tag{39}$$

where the internal pressure, P_I, is the pressure exerted over the cross sectional half-circle area, A_c. The internal pressure is found from Equation 40 and the area, A_c from Equation 41.

The $\Delta\rho$ in Equation 40 is related to the difference in density between the oil and the the surrounding gas. The temperature dependence of the oil density is given in

Table 7 while the gas density is calculated using the ideal gas law, Equation 3. Both oil and gas densities are evaluated at T_2, the temperature at Location 2, and shown in Figure 12.

$$P_I = (\Delta\rho) g h_{MAX} \tag{40}$$

$$A_c = \frac{\pi (r_{DROP})^2}{2} \tag{41}$$

The surface tension force, F_5, is the force that tends to keep the globule together and maintain a rounded edge shape. F_5 is approximated by Equation 42.

$$F_5 = \sigma_S (L) \tag{42}$$

The value of the surface tension, σ_S, utilized is that of Syntholube, shown in Table 5. The cross-sectional circumferential length, L, depicted in Figure 19b, is calculated by

$$L = \frac{(2\pi r_{DROP})}{2} = \pi r_{DROP} \tag{43}$$

By combining Equations, 38, 39, 40, 41, 42, and 43 and utilizing an approximation by Campbell and Padday that relates the height of a sessile drop to the radius, $h_{MAX} = 2r_{DROP}$, a single expression is found relating the maximum height, h_{MAX}, to the surface tension and internal pressure [34, 35].

$$h_{MAX} = 2\sqrt{\frac{\sigma}{(\Delta\rho)g}} \tag{44}$$

CHAPTER 5

PROGRAM STRUCTURE

The flowchart for the model developed in this research project is given in Figure 20. It shows both the structure of the model and the sequence of the calculations performed.

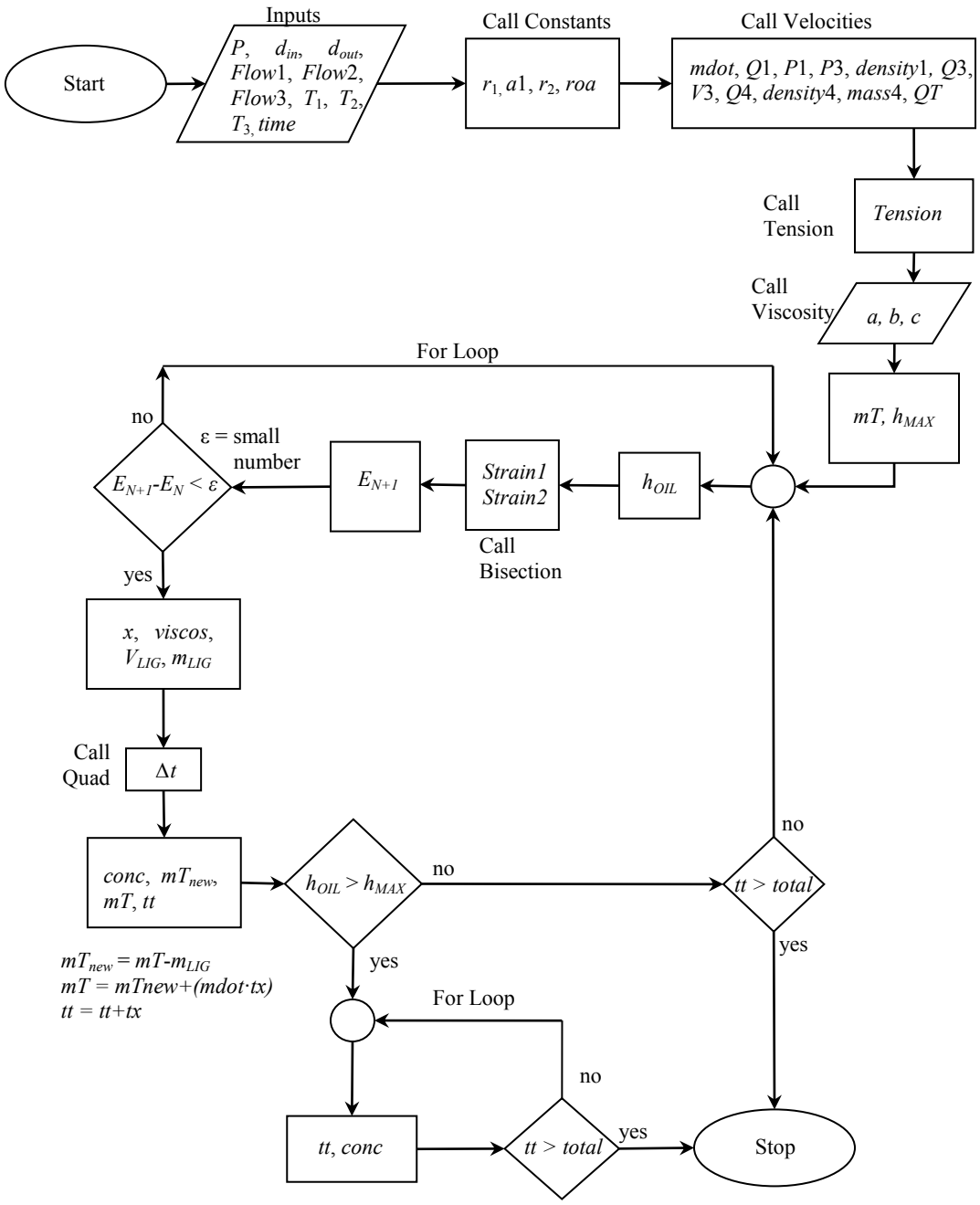

Figure 20: Program Flowchart

At the start, initial inputs are directly entered and used to calculate the variables seen in each of the call statements to the subroutines: Constants, Velocities, Tension, and Viscosity. The values returned by these subroutines are then used to calculate the total oil globule mass, mT, and the maximum oil globule height, h_{MAX}.

An iterative loop is used to calculate the height of the oil globule, h_{OIL}, and to call subroutine Bisection that calculates the rate of strain, $dE/dt = V_3/x$, by using the bisection numerical procedure. Once the strain, $dE/dt = V_3/x$ is found, it is used to calculate, x, *viscos*, V_{LIG}, and m_{LIG} which leads to the calculation of Δt in subroutine Quad.

Now that Δt is known, the concentration, *conc*, can be calculated, followed by the calculation of mT_{NEW}, the new total mass of the oil globule after the ligament sheared, mT, the total oil globule mass after oil is added, and *tt*, the total time the model ran.

Once the concentration is calculated and the mass, mT, has been updated, the model makes a decision: is $h_{OIL} > h_{MAX}$? If 'YES', then the model will enter another control loop that will not let h_{OIL} grow any larger, but will increment with the same time step, Δt, and hold the concentration steady until the total time exceeds that of the experimental time.

If the answer is 'NO', the model checks the total time, *tt*. If the total time, *tt*, is greater than *total*, the experimental time, the model ends. If the *tt* is smaller than *total*, then the algorithm loops back to the first 'For Loop' to find the next strain rate $dE/dt = V_3/x$. The algorithm loops until all the decision blocks answer 'YES'.

CHAPTER 6

RESULTS

The results of this research are presented in four sections. The first section, 'Model Validation,' validates the aerosol model by focusing on four test trials. These trials hold the fixture temperature and oil feed rate constant and vary the dilution gas flow rate. By taking the 'Absolute Difference in Concentration' expressed as a percentage between the experiment and the model, a trend is shown. Next, the plots for the four test trials are graphed and shown on a per second basis with the experimental results in 'Analysis of Model Results.' Lastly, after the model is shown to predict well, an additional 32 tests are analyzed in an 'Analysis of 36 Test Trials.'

The second section, 'Effects of Variation in Dilution Gas Flow Rate at Constant Temperature and Oil Feed Rate,' graphically presents the results of varying the dilution gas flow rate at constant oil feed rate and temperature.

The third section presents the 'Effects of Fixture Temperature Variation at a Constant Oil Feed Rate.' By varying the fixture temperature and holding the oil feed rate constant, the concentration reveals a trend

The fourth section, 'Effects of Oil Feed Rate Variation at Constant Fixture Temperature,' graphically presents the results of varying the oil feed rate when the temperature is constant.

Model Validation

One of the most important steps in the development of a numerical model is its validation with experimental data. The model predictions must be both accurate and

representative of the experimental design. Otherwise, the results from the algorithm cannot be trusted and hence the model would not be a viable design tool for future use. A significant amount of effort has been devoted in this research to validate the developed methodology using experimental data. This section provides the evidence of this effort.

The inputs utilized to validate the model are given in Tables 8 and 9.

Table 8 shows the inputs that remained constant for the validation tests, while Table 9 gives the various dilution gas flow rates used. All the values utilized in Tables 8 and 9 are a subset of

Table 10 and noted by an asterisk (*) in

Table 10.

Table 8: Constant values used for the input of model. *Note: Table is a partial subset of*

Table 10.

Time (s)	Orifice Plate Diameters		Pressure Above Orifice (psi)	Gas Flow rate (L/min.)	Oil Feed Rate (mL/hr.)	Temperature (K)		
	Inner (um)	Outer (um)				Room	Fixture	Meter
600	300	9.5	100	0.092	0.7	291.78	390	303

Table 9: Test numbers showing the variable gas dilution rates used for the input of the model. *Note: Table is a partial subset of*

Table 10.

Test Number	Dilution Gas Flow Rate (L/min.)	Time Averaged Concentrations (mg/m^3)		Absolute Difference in Concentration (%)
		Experimental	Model	
1	5.907	713	775	8.7
2	8.806	598	539	9.9
3	11.617	422	416	1.4
4	16.977	367	291	20.7

Table 9 shows four tests numbered one through four and their respective dilution gas flow rates. For each test, Table 9 also gives time averaged values of oil aerosol concentration as determined from the CK Engineering experimental test rig and from the physics based model developed in this research project. Table 9 also gives the absolute value of the difference between the experimental and model results as a percentage. See Equation 45.

$$\text{Absolute Difference in Concentration (\%)} = \left| \frac{\text{Experimental Time Averaged Concentration} - \text{Model Time Averaged Concentration}}{\text{Experimental Time Averaged Concentration}} \right| \times 100 \qquad (45)$$

As shown in the last column of Table 9, the 'Absolute Difference in Concentration' varies from 8.7% to 20.7% with an average absolute difference for the cases being 10.2% which is excellent agreement considering the variability of the experimental data.

Analysis of Model Results

This section presents a detailed analysis of four validation test trials. These four test trials are a subset of the 36 test trial simulations conducted in this project.

The inputs utilized by the model are given in Tables 8 and 9.

Table 8 shows the inputs that remained constant for each of the test trials, while Table 9 gives the various dilution gas flow rates used. All the values utilized in Tables 8 and 9 are a subset of

Table 10 and noted by an asterisk (*) in

Table 10.

In Graphs 3, 4, 5, and 6 the experimental data from CK Engineering is represented by a blue line. The green line is the time average of the blue line and represents the time average of the aerosol concentration as determined from the CK Engineering experiment. This value is reported in Table 9 as the 'Experimental Time Averaged Concentration.'

The red line in Graphs 3, 4, 5, and 6 is a plot of the oil aerosol concentration as determined by the model and recorded every second. The time average of the red line is also reported in Table 9 as the 'Model Time Averaged Concentration.' The absolute difference between the time averaged values of the experimental and model concentrations is shown in the 'Absolute Difference in Concentration' column of Table 9.

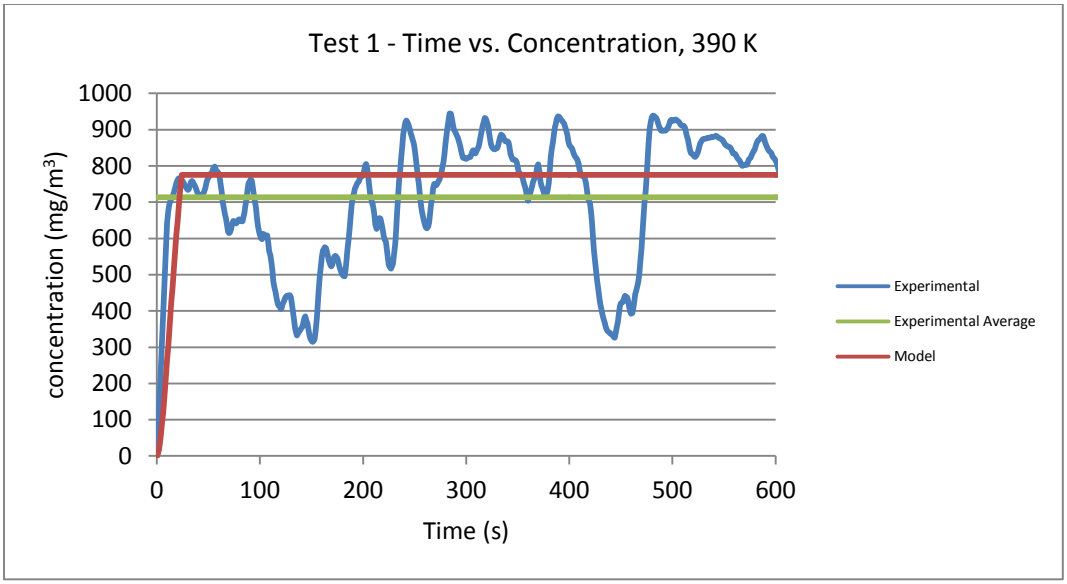

Graph 3: Test 1 - Time vs. Concentration at 390 K for a dilution of 5.907 L/min.

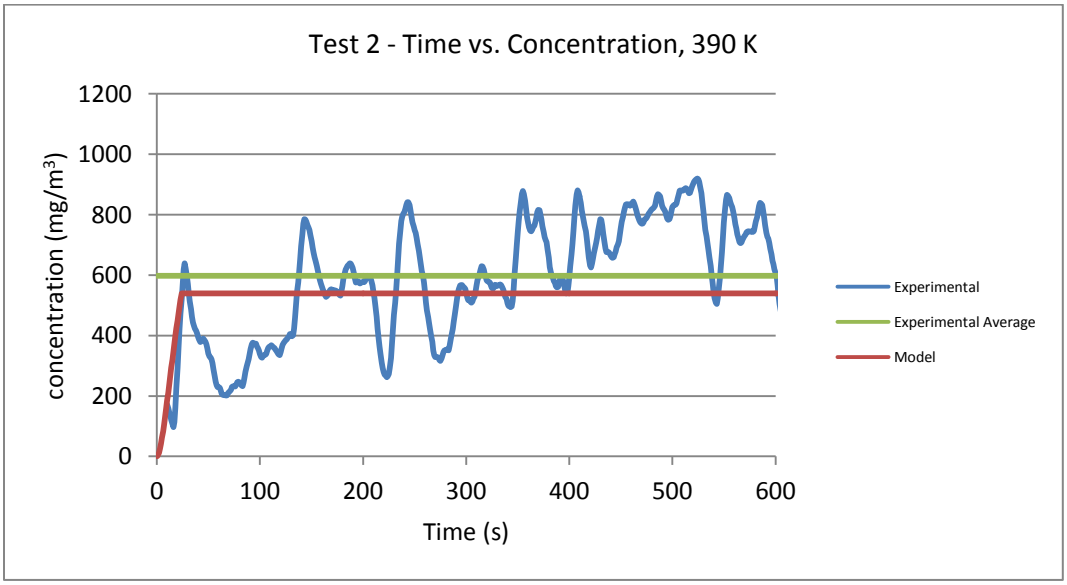

Graph 4: Test 2 - Time vs. Concentration at 390 K for a dilution of 8.806 L/min.

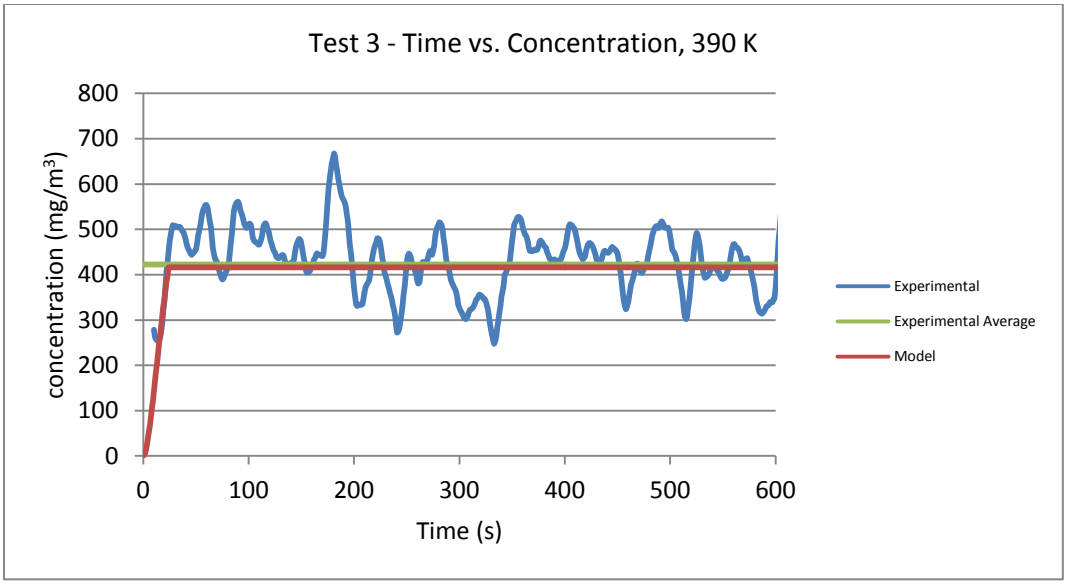

Graph 5: Test 3 - Time vs. Concentration at 390 K for a dilution of 11.617 L/min.

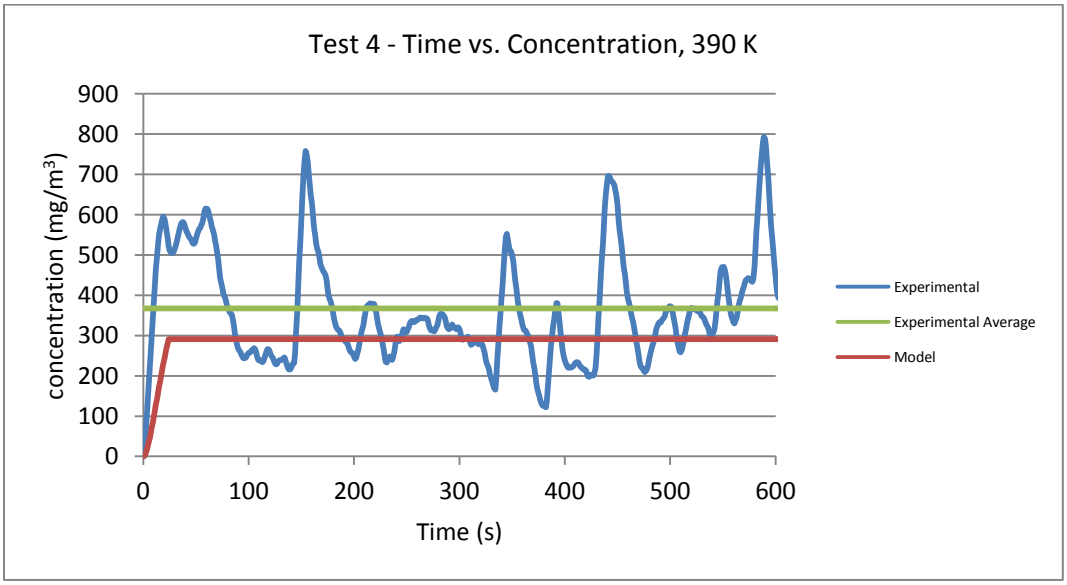

Graph 6: Test 4 - Time vs. Concentration at 390 K for a dilution of 16.977 L/min.

The experimental results from CK Engineering shown in Graphs 3, 4, 5, and 6 are reported on a per second basis from the concentration meter. This means that the meter reports a single concentration value for a given second. This single concentration value from the concentration meter is obtained by taking several concentration samples a second and averaging those values. This average value is then reported as the concentration for that second.

The model behaves similarly, by calculating concentration several times within a second, however only one concentration is reported every second. This is done to control the amount of time the model runs by speeding up the processing. It also eases comparison with the CK Engineering results. If the model were to report a concentration for every time step, Δt, there could be as many as 500 concentrations listed for each second.

At the beginning of a simulation, the concentration ramps up over a short amount of time as shown in Graphs 3, 4, 5, and 6. This is due to the simultaneous addition and subtraction of oil. When oil is added to the system, the height of the oil sitting on the orifice plate increases. Hence, the amount of oil sheared off as a ligament increases as does the aerosol concentration. When the amount of oil sheared off in the form of a ligament is equal to the amount of oil being added, the concentration stabilizes. This stabilization is represented by the horizontal portion of the red lines shown in Graphs 3, 4, 5, and 6.

The physics-based model tracks the CK Engineering experimental test results well. As the experiment ramps up at the beginning of the test, the model follows. Although the experiment has fluctuations in the concentrations over the total test time as shown by the blue line, the average of those fluctuating concentrations is shown to be close to the models calculated concentration. This is seen by comparing the time averaged concentration of the experiment, the green line, and the concentration calculated by the model at a particular second as shown by the red line. The values are similar.

Analysis of the 36 Test Trials

Table 10 shows the results from the 36 test trials. The trials are categorized from least to greatest by the oil feed rate. The fixture temperatures for each of the feed rates are shown to be one of three temperatures: 390 K, 420 K, or 480 K. The dilution gas flow rates are listed from least to greatest for each of the temperatures, for each of the oil feed rates. Test Trials 16–19, corresponding to an oil feed rate of 0.7 mL/hr. and a fixture temperature of 390 K, are the test trials that have been discussed in detail in the section on 'Model Validation and the Effects of Dilution Gas.'

The experimental time average concentration reported from CK Engineering is shown for each test trial and accompanied by the model's time average results. Also, the absolute value of the difference between the experimental and model concentrations is shown as a percentage for each test trial, calculated according to Equation 45.

Table 10: Results for test numbers 1-36. * Indicates values utilized in Table 9.

Test Number	Oil Feed Rate (mL/hr.)	Fixture Temp (K)	Dilution Gas Flow Rate (L/min.)	Time Averaged Concentration (mg/m^3)		Absolute Difference in Time Averaged Concentration (%)
				Experimental	Model	
1	0.5	390	11.617	430.35	416	3.3
2			16.977	248.75	290	16.6
3		420	10	643.72	604	6.2
4			16.977	405.3	366	9.7
5			20	352	306.7	12.9
6		480	20	252	302	19.8
7	0.6	390	5	705	889	26.1
8		480	25	404	293	27.5
9	0.65	390	10	514.8	479	7.0
10			11.617	585	416	28.9
11			15	372	326	12.4
12			16.977	282.1	284	0.7
13			20	441.3	388	12.1
14		480	36.617	279.62	213	23.8
15				303	213	29.7
16	0.7	390*	5.907	713	775	8.7
17			8.806	598	539	9.9
18			11.617	422	416	1.4
19			16.977	367	291	20.7
20		420	10	840	846	0.7
21	0.75	390	5.907	769	755	1.8
22			11.617	496	466	6.0
23				398	466	17.1
24				544	466	14.3
25				586	466	20.5
26			16.977	346.8	289	16.7
27				371	288	22.4
28			20	398.8	390	2.2
29		420	10	841	898	6.8
30				775.4	892	15.0
31			16.977	555	542	2.3
32			20	465	466	0.2
33			31	293	293	0.0
34	0.8	390	11.617	535	418	21.9
35			16.977	272	290	6.6
36		420	30.907	440	326	25.9

The maximum and minimum 'Absolute Difference in Time Averaged Concentration' values shown in Table 11 represent the highest and lowest absolute difference in time averaged concentration for the 36 test cases seen in

Table 10. The average is the computed mean of the 'Absolute Difference in Time Averaged Concentration' values listed in

Table 10 and represented as a single value, 12.72%. This value represents that on average, the model's time averaged concentration is 12.72% different from the experimental time averaged concentration.

Table 11: Statistical Results Summary

	Maximum	Minimum	Average	St Dev
Absolute Difference in Time Averaged Concentration (%)	29.7	0	12.72	0.26

The standard deviation (St Dev) is a measure of the dispersion from the average. For this particular data set, the standard deviation is considered low at 0.26%. This means that overall the 'Absolute Difference in Time Averaged Concentration' values tend to be close to the average.

The summarized results in Table 11 show a strong relationship between the experimental and model time averaged concentrations. This strong relationship is expressed well by the correlation coefficient. The correlation coefficient expresses how well a predicted trend follows a measured trend, or in these cases, how well the time averaged concentration predicted by the model follows the time averaged concentration measured in the experiment. If the experiment and the model agree well, the value of the

correlation coefficient will be either close to one or negative one. If close to one, the experimental and model values increase at nearly the same rate. If the correlation coefficient is close to negative one, the opposite would be true, meaning that the experimental and model values decrease at nearly the same rate. See Graph 7 for a graphical representation of the correlation coefficient grouped by temperature and Graph 8 for a graphical representation of the correlation coefficient grouped by oil feed rate.

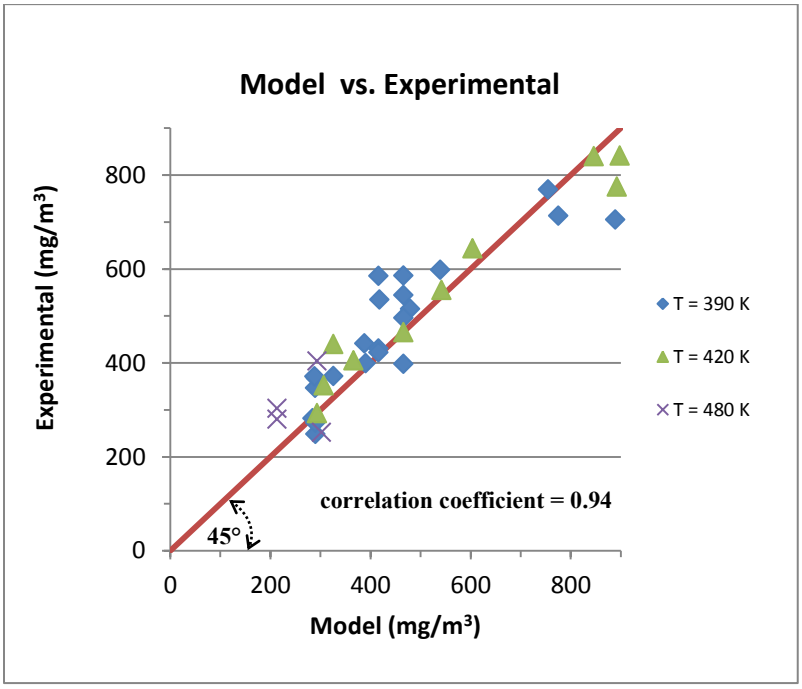

Graph 7: Model Concentration vs. Experimental Concentration grouped by temperature.

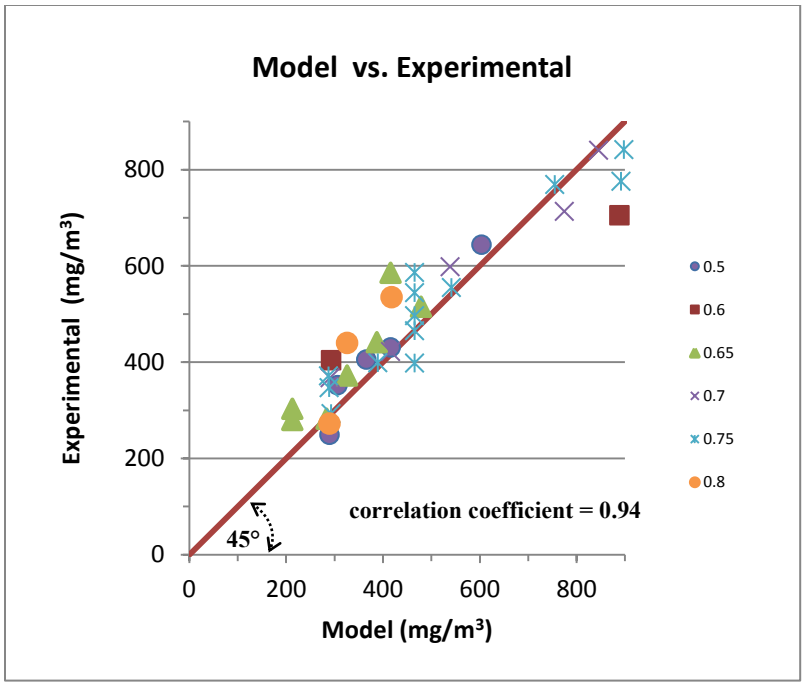

Graph 8: Model Concentration vs. Experimental Concentration grouped by oil feed rate.

In Graphs 7 and 8, the red 45° lines represent a correlation coefficient equal to one or the situation in which the experimental and model time averaged concentrations are equal. Of the 36 tests tabulated in Table 10, this occurs once, at Test 33. The other test cases come close to the red line, however they do have a variance. The overall correlation coefficient of the 36 test cases is 0.94, showing good agreement between the experimental and model time averaged concentrations.

Graph 9 compares the experimental and model concentrations by fixture temperature. Groupings can be found that correspond with the various oil feed rates. Thus, Graph 9 gives insight into how well the model makes predictions with reference to the oil feed rates at the various temperatures.

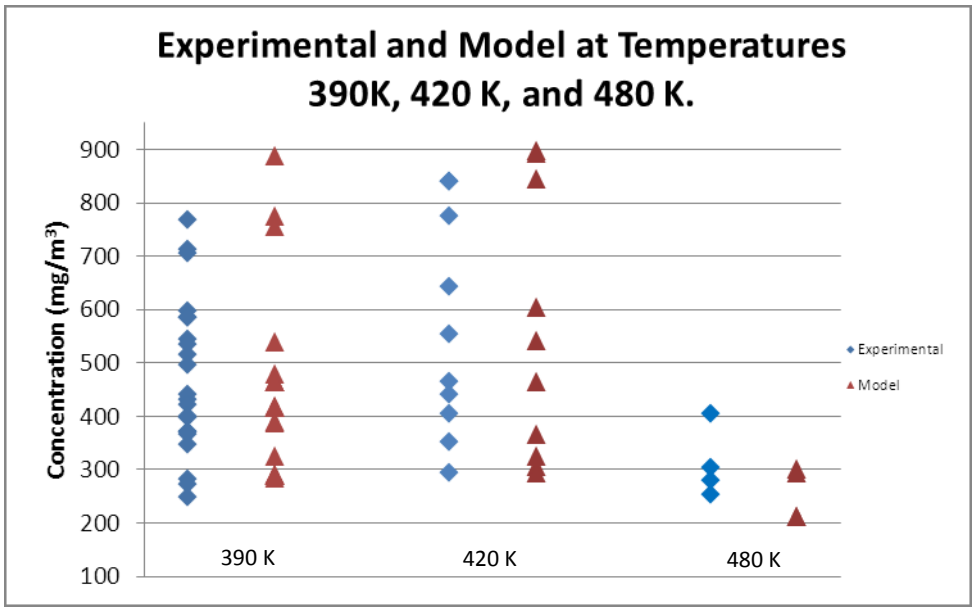

Graph 9: A comparison graph showing the Experimental and Model Concentrations plotted versus Temperatures

As shown in Graph 9, the model predicts the experimental results well. First, by looking at the 390 K fixture temperature, the model and the experiments have similar groupings. These groupings occur at the different oil feed rates and show how well the model performs at those oil feed rates. The groupings shown by the 420 K fixture temperature show similar performance as does the 480 K fixture temperature range.

Overall, as shown in Graph 9 and by the values recorded in

Table 10, the model performs best at the 420 K fixture temperature with an oil feed rate of 0.75 mL/hr. The oil aerosol concentrations calculated by the model at a fixture temperature of 420 K have a stronger dependence on the oil feed rate than those concentrations calculated at fixture temperatures 390 K and 480 K. Furthermore, it is shown generally by Graph 9, that when the fixture temperature is increased, the oil aerosol concentration determined experimentally decreases as does the concentration determined by the model.

Effects of Variation in Dilution Gas Flowrate on Concentration at Constant Temperature and Oil Feed Rate

By comparing Graphs 3-6, and inspecting the 'Dilution Gas Flow Rate' and the 'Time Averaged Concentrations' in Tables 9 and 10 for both the experiment and the model, the effects of the dilution gas flow rate upon the oil aerosol concentration are seen. The effects of variation in dilution gas flow rate are shown in Graph 10 for a constant oil feed rate of 0.7 mL/hr. and a constant fixture temperature of 390 K.

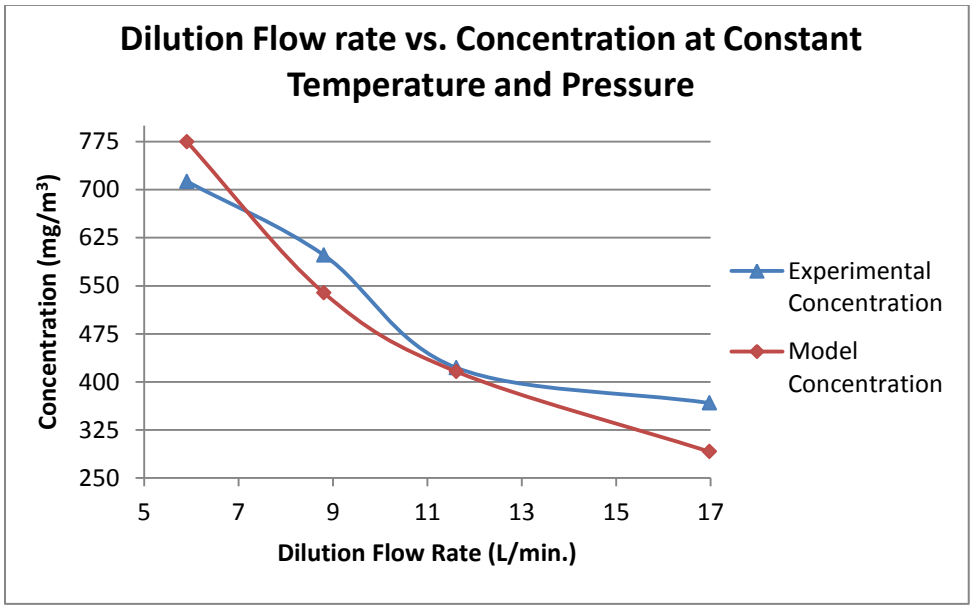

Graph 10: Dilution Flowrate vs. Concentration at Constant Temperature and Pressure.

At a dilution gas flowrate of 5.907 mL/hr., the concentration calculated by the model is higher than that of the experimental measurements. Vice versa is true for the 8.806 mL/hr. dilution gas flow rate. At a dilution gas flowrate of 11.617 mL/hr., the measured concentration from the experiment and the concentration calculated by model are nearly equal with an 'Absolute Difference in Concentration,' of 1.4%. At the dilution gas flowrate of 16.977 mL/hr., the calculated concentration from the model is lower than that of the experiment.

Overall, the trends of the experimental and model concentrations are similar. Graph 10 shows that as the dilution gas flow rate is increased, the oil concentration in the aerosol decreases. However, graphically, the model concentration is a smoother fit.

Effects of Fixture Temperature Variation at Constant Oil Feed Rate

Graphs 11-16 depict the effects of temperature variation upon the experimental and model time averaged concentrations at various oil feed rates. As before, the red 45° line indicates complete agreement between the experimental and model results.

Graph 11, for an oil feed rate of 0.5 mL/hr., shows that the model performs well when the fixture temperature is equal to 420 K, although it slightly under predicts. When the fixture temperature is 390 K, the model both over and under predicts, while at the 480 K fixture temperature, no conclusive results could be determined due to the low number of data points. Lastly, the three data points at 420 K indicate three different concentrations that correspond to the three different dilution gas flow rates used, as seen in

Table 10.

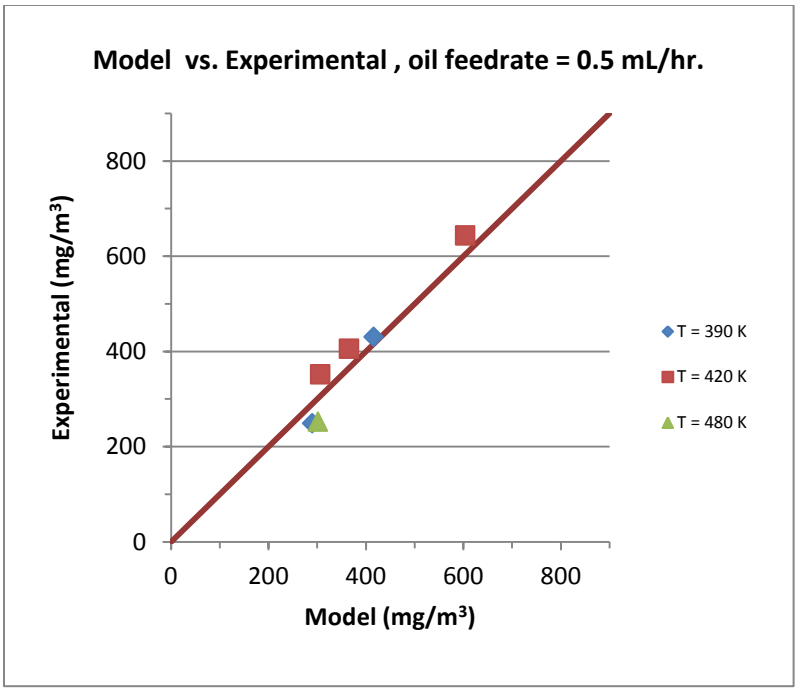

Graph 11: Model Concentration vs. Experimental Concentration with an oil feed rate = 0.5 mL/hr. at 390 K, 420 K, and 480 K.

Graph 12 has only two data points, thus little can be concluded other than at the temperature of 480 K, the model under predicts and at 390 K over predicts.

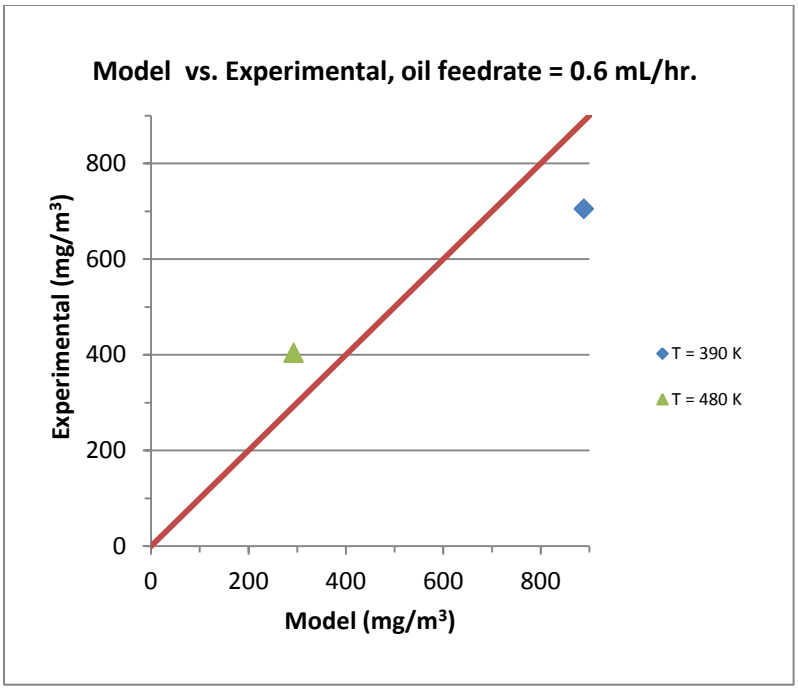

Graph 12: Model Concentration vs. Experimental Concentration with an oil feed rate = 0.6 mL/hr. at 390 K and 480 K.

Graph 13, for an oil feed rate of 0.65 mL/hr., shows that the model under predicts the concentration for four of the five data points at a fixture temperature of 390 K. The fifth data point, positioned nearly on top of the red 45° degree line, has an 'Absolute Difference in Concentration' of only 0.7%, meaning an almost perfect correlation. Also, the various concentrations given for each temperature correspond to the different dilution gas flow rates used, as shown in

Table 10. That is, as the dilution increases, the concentration decreases. The two data points at the fixture temperature of 480 K show that the model under predicts, however these points do show a grouping.

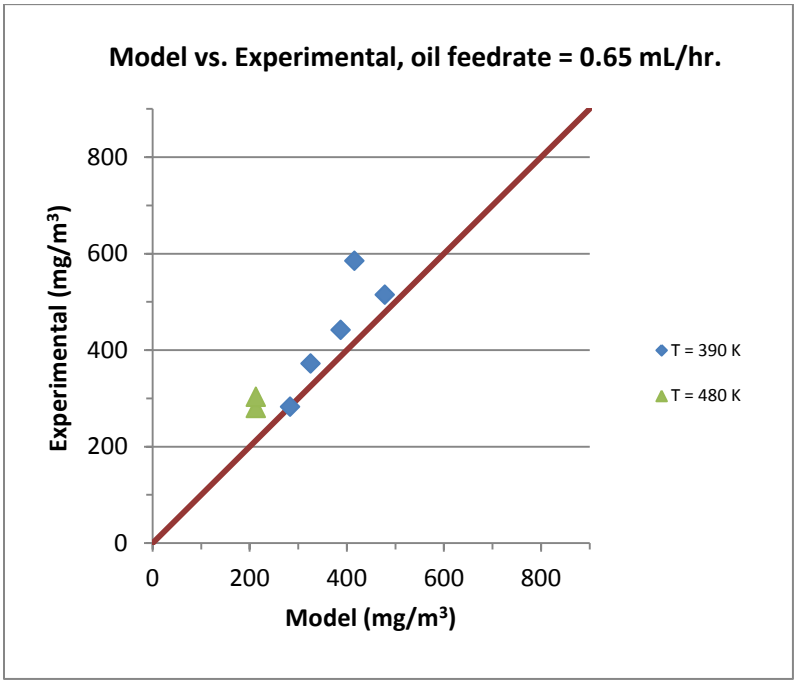

Graph 13: Model Concentration vs. Experimental Concentration with an oil feed rate = 0.65 mL/hr. at 390 K and 480 K.

Graph 14, for an oil feed rate of 0.7 mL/hr., depicts the data utilized for Table 9 at a fixture temperature of 390 K. For two of the four data points at 390 K, the model under predicts and over predicts for the third. The fourth data point, positioned nearly on top of the red 45° degree red line, has a nearly perfect correlation. The correlation is confirmed by a low 'Absolute Difference in Concentration' of only 1.4%.

Although there is only one data point for the fixture temperature of 420 K, the model's performance is nearly flawless. This is shown graphically by the data point lying nearly perfectly on the red 45° degree line and mathematically by a low 'Absolute Difference in Concentration' of 0.7%. Also, as shown in

Table 10, at a constant temperature, each data point has a different dilution gas flow rate. When the dilution gas flow rate increases at a constant temperature and oil feed rate, the concentration decreases.

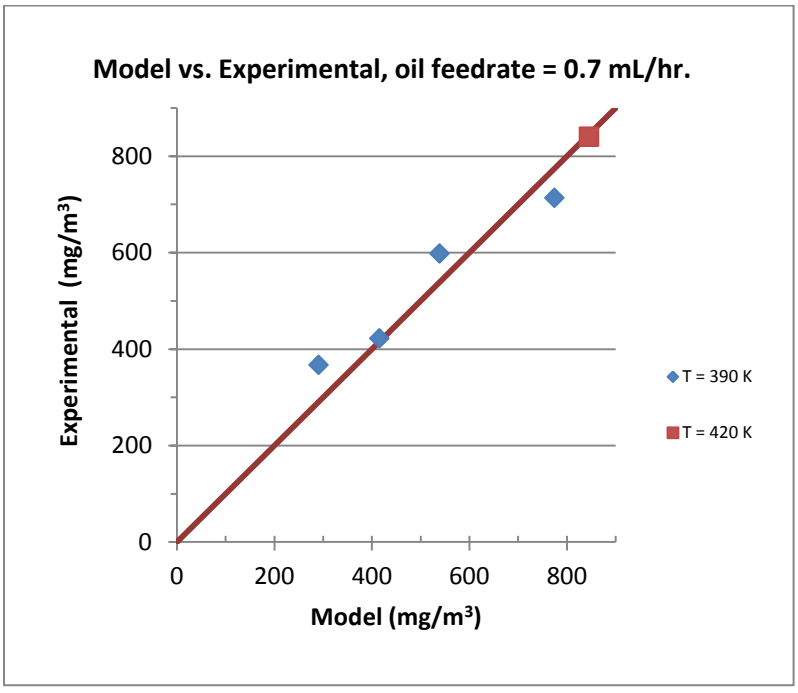

Graph 14: Model Concentration vs. Experimental Concentration with an oil feed rate = 0.7 mL/hr. at 390 K and 420 K.

Graph 15, for an oil feed rate of 0.75 mL/hr., displays the most data for a fixture temperature at 390 K. For five of the eight data points, the model under predicts, and over predicts for one data point. The two other data points at the fixture temperature of 390 K show a strong correlation by having low 'Absolute Difference in Concentration' of 1.8% and 2.2%.

The fixture temperature of 420 K also shows a strong correlation for three of the five data points plotted. The three strong data points have low 'Absolute Difference in Concentration' of 0, 0.2% and 0.3%. Graphically this strength is shown by its proximity to the red 45° degree line. The other two data points show an over prediction by the model, however they have an acceptable 'Absolute Difference in Concentration' of 6.8% and 15%. Furthermore, it is shown that for each data point with the same temperature, as the dilution gas flow rate increases, the concentration decreases.

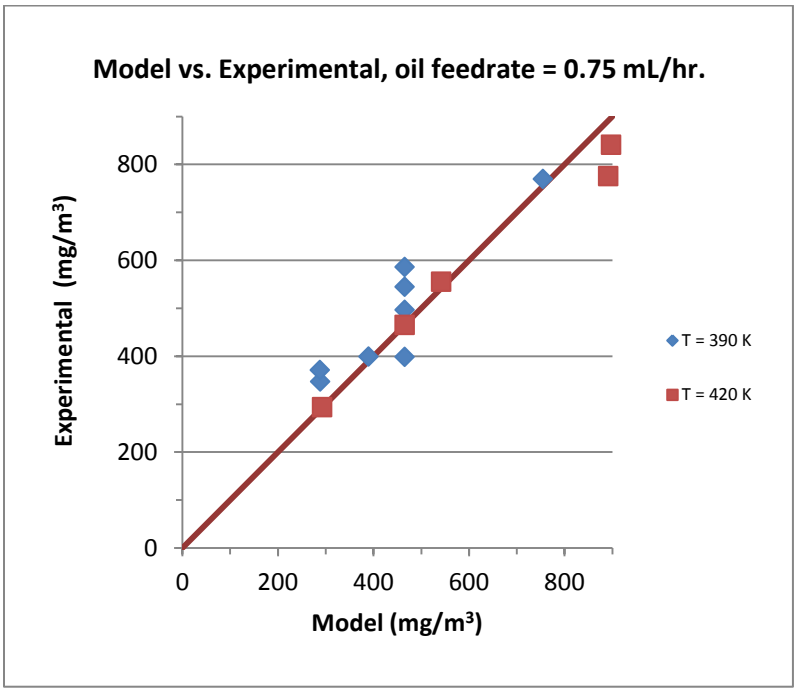

Graph 15: Model Concentration vs. Experimental Concentration with an oil feed rate = 0.75 mL/hr. at 390 K and 420 K.

Graph 16, for an oil feed rate of 0.8 mL/hr., shows two data points at a fixture temperature of 390 K and one at 420 K. The first 390 K data point shows that the model over predicts and the second data point shows under prediction. The over prediction of the first data point is only minor as shown by its close proximity to the red 45° degree line and its somewhat low 'Absolute Difference in Concentration' of 6.6%. The 420 K fixture temperature data point shows that the model under predicts with an 'Absolute Difference in Concentration' of 25.9%.

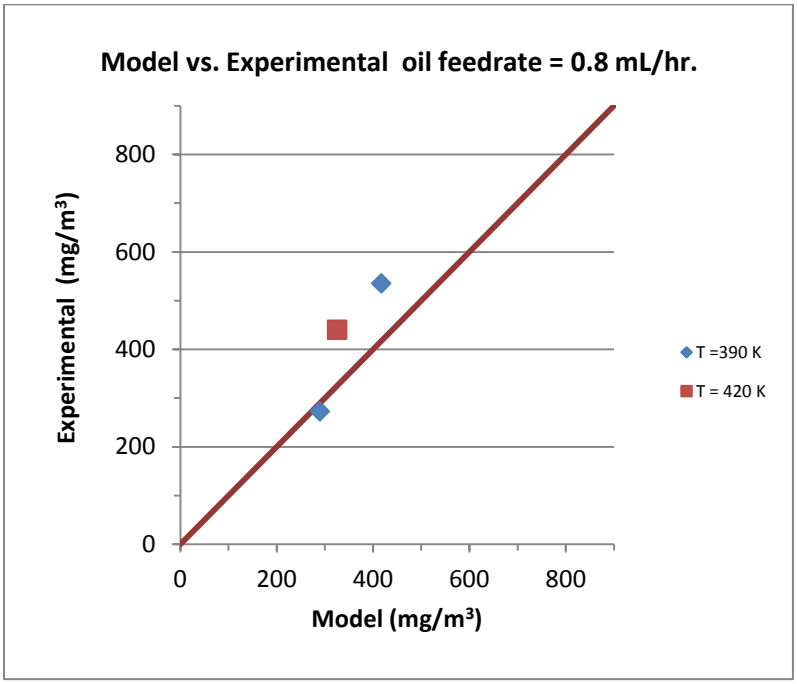

Graph 16: Model Concentration vs. Experimental Concentration with an oil feed rate = 0.80 mL/hr. at 390 K and 420 K.

In summary, by plotting the aerosol concentrations at various temperatures for each oil feed rate in Graphs 11-16, the effect of temperature on the concentration is shown. For the model concentrations calculated at a fixture temperature of 390 K and a constant dilution gas flow rate, the model concentrations predicted closely follow those

of the experiment a majority of the time, however, there is some variance. The model concentrations calculated at a fixture temperature of 420 K with a constant dilution gas flow rate show a nearly flawless agreement with the experimental data. Both these statements agree well with the conclusion stated before, the best model performance is at the 420 K fixture temperature.

In general, at the higher temperatures, the concentration tends to be lower, and, at the lower temperatures, the concentration tends to be higher. This trend can be explained by the temperature dependence of the dynamic viscosity. Dynamic viscosity decreases with increasing temperature resulting in a decreased strain rate. The decreased strain rate in return affects the thickness and height of the oil ligament, x and h_{OIL}, and ultimately the mass of the ligament, m_{LIG}.

Effects of Fixture Temperature Variation at Constant Oil Feed Rate Without Dilution Gas

In the experiment, the dilution gas is utilized to dilute the oil aerosol to keep within the range of the concentration meter. Mathematically, the dilution gas has no effect upon the mechanisms for aerosol formation, it only affects the measurements taken by the concentration meter. Thus, it is appropriate to see how the model reacts with relation to the varied fixture temperature without the effects of the dilution gas. This can be achieved in the model by simply setting the dilution gas flow rate to zero.

By removing the dilution gas, holding the oil feed rate constant, and varying the temperature, the concentration changes. These effects are shown in Table 12 and Graph 17.

Table 12: Table containing the oil feed rate, fixture temperature, and time averaged concentrations from the aerosol model.

Oil Feed Rate (mL/hr.)	Fixture Temp (K)	Time Averaged Concentration (mg/m^3)
0.5	390	8697
	420	8604
	480	8458
0.6	390	10467
	420	10333
	480	10173
0.65	390	11353
	420	11268
	480	11031
0.7	390	12238
	420	12103
	480	12073
0.75	390	13125
	420	13023
	480	12944
0.8	390	14013
	420	13856
	480	13650

Table 12 shows the oil feed rates, fixture temperatures, and the time averaged concentrations calculated by the model. The oil feed rates and fixture temperatures are categorized from least to greatest and used as inputs for the aerosol model. The concentrations calculated from the model are categorized in decreasing order for each of the oil feed rates.

Graph 17 plots the model's calculated concentration for each of the three fixture temperatures, 390 K, 420 K, and 480 K, as a function of the oil feed rate. The lowest

calculated concentrations are at the lowest oil feed rate and the highest calculated concentrations are at the highest oil feed rate. From the graph and the table, it is shown that the 0.65 mL/hr. oil feed rate is the feed rate most affected by fixture temperature. Graphically, this is shown by a large difference in concentration between the fixture temperatures of 420 K and 480 K. The oil feed rate least affected by fixture temperature is 0.7 mL/hr. This is shown in the graph between the fixture temperatures of 420 K and 480 K by having a small concentration difference. Lastly, it is shown that by holding the oil feed rate constant and increasing the fixture temperature, the concentration decreases.

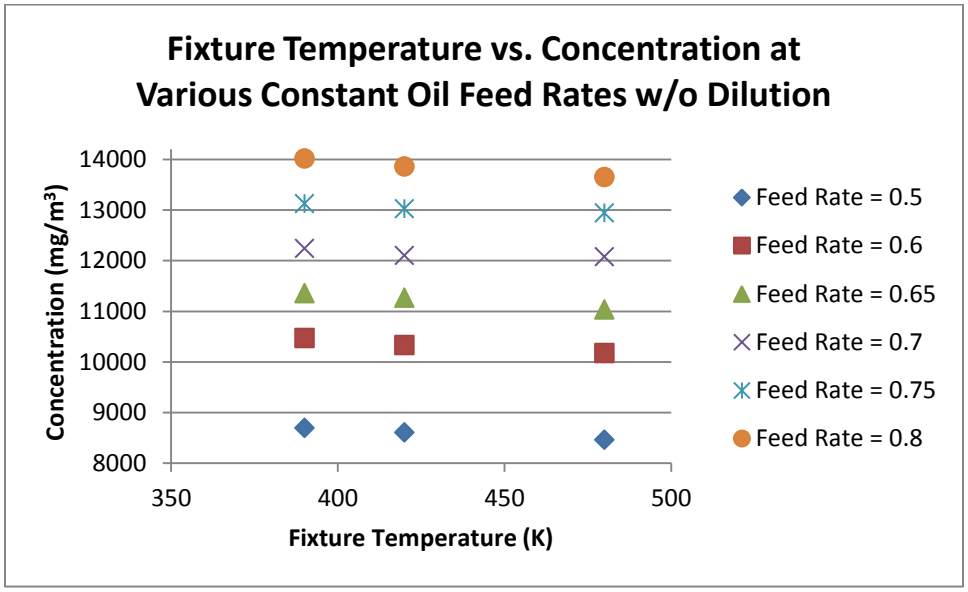

Graph 17: Fixture Temperature vs. Concentration at Various Constant Oil Feed Rates without Dilution Gas.

As discussed earlier, the dynamic viscosity decreases with increasing temperature resulting in a decreased strain rate. The decreased strain rate in return affects the thickness and height of the oil ligament, x and h_{OIL}, and ultimately the mass of the ligament, m_{LIG}.

Effects of Oil Feed Rate Variation at Constant Fixture Temperature

Graphs 18-20 depict the effects of varying the oil feed rate upon the experimental and model time averaged concentrations at various temperatures. Again, the red 45° line indicates complete agreement between the experimental and model results.

The overall agreement between the model and the experiment, shown in Graph 18 for the fixture temperature of 390 K, is very good. The largest 'Absolute Difference in Concentration' shown, 28.9%, is at the oil feed rate of 0.65 mL/hr. The smallest 'Absolute Difference in Concentration' is 0.7% and occurs at the oil feed rate of 0.7 mL/hr. The difference between the smallest and largest 'Absolute Difference in Concentration' is just 21.9%, thus the large number of concentration values at 390 K are well represented by the model. Furthermore, it is shown that for each data point with the same oil feed rate, as the dilution gas flow rate increases, the concentration decreases.

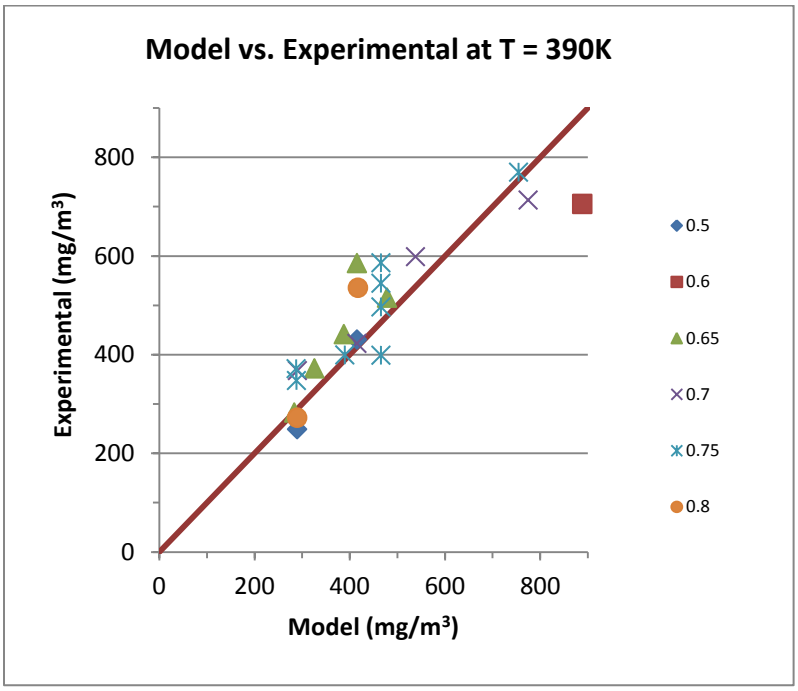

Graph 18: Model Concentration vs. Experimental Concentration at T = 390 K for various oil feed rates.

At the oil feed rate of 0.5 mL/hr., the model under predicts for one data point and over predicts for the other. At the 0.6 mL/hr. oil feed rate, the model under predicts four

out of the five test trials. At the 0.7 mL/hr. oil feed rate, the model over predicts once in the four trials shown and under predicts for the others. At the 0.75 mL/hr. oil feed rate the model over predicts only once and under predicts for the other seven trials. At an oil feed rate of 0.8 mL/hr., the model under predicts two out of the three test trials.

The 0.75 ml/hr. oil feed rate shown in Graph 19, for a fixture temperature of 420 K, has three data points having less than an 1% 'Absolute Difference in Concentration' as shown by their close proximity to the red 45° line. The other two data points at the same oil feed rate show over predictions by the model. At both the 0.5 mL/hr. and 0.8 mL/hr. oil feed rates, the model under predicts slightly. The model slightly over predicts the experimental concentration at the 0.7 mL/hr. feed rate with a 0.7% 'Absolute Difference in Concentration.' Also, it is shown that for each data point with the same oil feed rate, as the dilution gas flow rate increases, the concentration decreases.

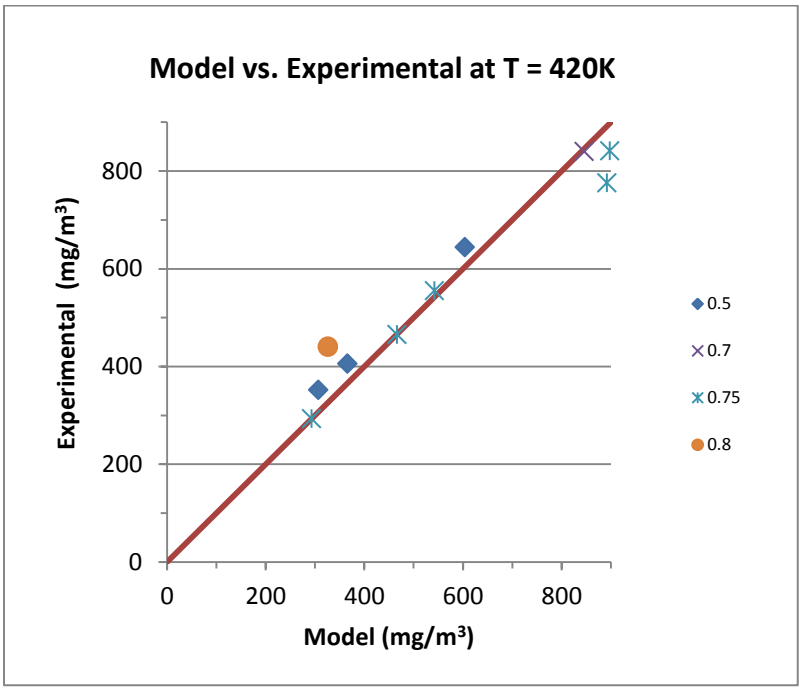

Graph 19: Model Concentration vs. Experimental Concentration at T = 420 K for various oil feed rates.

The two data points shown for the oil feed rates of 0.5 mL/hr. and 0.6 mL/hr. shown in Graph 20 are in close proximity to the red 45° line, however little can be concluded from the points, due to the low volume of data for the entire graph. The same conclusion can be drawn for the two data points at the 0.65 mL/hr. oil feed rate.

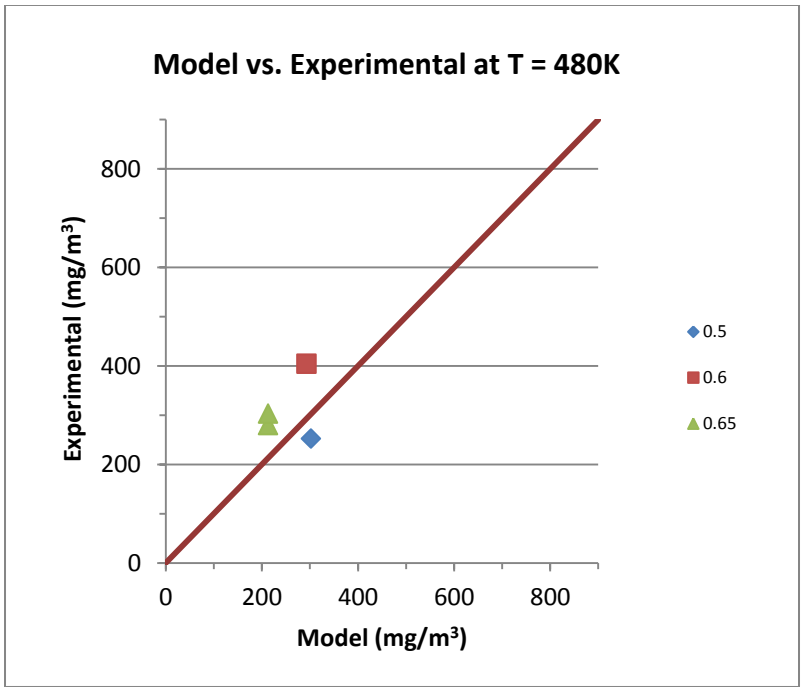

Graph 20: Model Concentration vs. Experimental Concentration at T = 480 K for various oil feed rates.

In summary, the plots shown in Graphs 18-20 show the correlation between the model and experimental concentrations at each temperature, 390 K, 420 K, and 480 K, as a function of the oil feed rates.

The experimental and model concentrations at a fixture temperature of 390 K show an oil feed rate dependence. The concentration values measured experimentally increase as the oil feed rate increases. The concentrations calculated by the model also increase as the oil feed rate increases. At the 420 K fixture temperature, the model tracks

the experimental concentrations more closely than it does at the 390 K fixture temperature, making 420 K the temperature with the best agreement between the model and the experiment. At the 480 K fixture temperature, the model concentrations and the experimental concentrations increase with oil feed rate, however, with only four data points, little can be concluded.

Generally, these results show that by increasing the oil feed rates and holding the temperature constant, the concentration increases. This agrees with intuition. If more oil is available for ligament growth and subsequent shearing, the higher the concentration.

Effects of Oil Feed Rate Variation at Constant Fixture Temperature Without Dilution Gas

As stated before in 'Effects of Fixture Temperature Variation at a Constant Oil Feed Rate Without Dilution Gas,' the dilution gas is utilized in the experiment to dilute the oil aerosol to keep it within the range of the concentration meter. Mathematically, the dilution gas has no effect upon the mechanisms for aerosol formation, it only affects the measurements taken by the concentration meter. Thus, it is appropriate to see how the model reacts with relation to the varied oil feed rate without the effects of the dilution gas. This can be achieved in the model by simply setting the dilution gas flow rate to zero.

By removing the dilution gas, holding fixture temperature constant, and varying the oil feed rate, the concentration changes. These effects are shown in Table 12 and Graph 21.

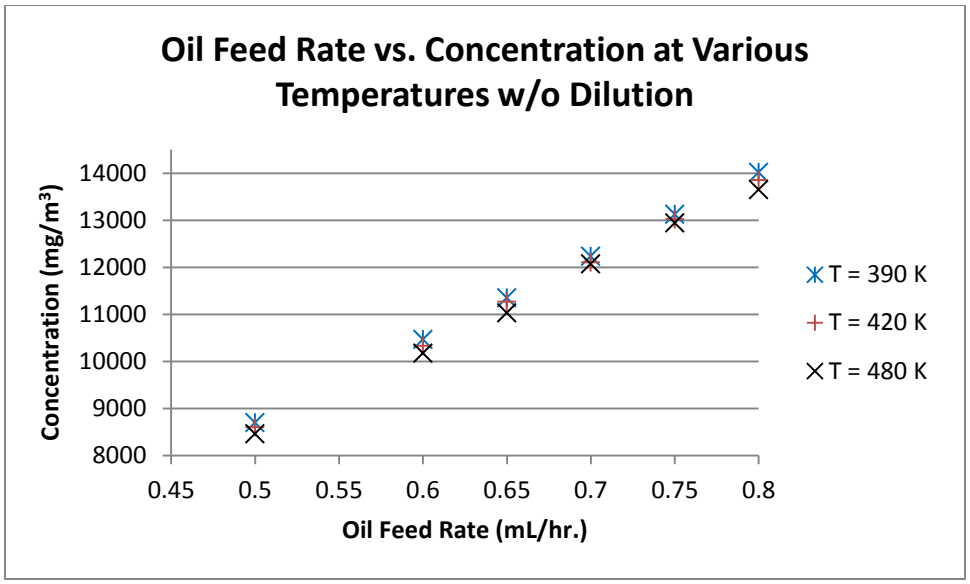

Graph 21: Oil Feed Rate vs. Concentration at Various Temperatures without Dilution Gas.

Graph 21 plots the same values shown in Table 12, except in terms of the varied oil feed rate instead of fixture temperature. By varying the oil feed rate and utilizing the same fixture temperature for each of the three oil feed rates, it is shown that the concentration increases as the oil feed rate increases. Also, at each oil feed rate, three fixture temperatures are plotted, 390 K, 420 K, and 480 K. The lower fixture temperature, 390 K, shows the higher concentration, and the higher fixture temperature, 480 K, shows a lower concentration. The middle fixture temperature, 420 K, shows a concentration between the highest and lowest concentrations.

CHAPTER 7

CONCLUSION

The hydrocarbon emissions of an internal combustion engine are directly correlated with the engine's oil consumption. This oil consumption is associated with reverse blow-by, a condition in which gases flow past the ring-pack from the crankcase to the combustion chamber. This reverse blow-by breaks down the oil film on the cylinder walls and entrains oil particles in the gas flow during the downstroke of the piston.

In this project a physics-based numerical model was developed that accurately describes the formation of aerosols in the ring pack of a reciprocating piston by simulating the mechanisms by which oil globules are broken up, atomized, and entrained in a gas flowing through an orifice. The gas is modeled using mass flows or conservation of mass methodology and the oil aerosol as a sheared piece of mass (ligament). While the gas theory is straight forward utilizing first principles, the oil theory is a new methodology. The oil theory starts as a mass that is sheared. The shearing involves the properties of the fluid; strain rate, density, and viscosity, which all vary with time, temperature, and oil injection rate. The oil injection rate and temperature are shown to have a profound effect on the size of the oil ligament and ultimately the concentration.

This conclusion was deduced by comparing the concentrations that were ran at varied oil feed rates and constant temperatures. By increasing the oil feed rate and holding the temperature constant, the concentration increased. The results agree with intuition, if more oil is available to shear, the higher the concentration.

Also, by comparing the aerosol concentrations at various temperatures for constant oil feed rates, the effect of temperature on the concentration is shown. At the higher temperatures, the concentration tends to be lower, and, at the lower temperatures, the concentration tends to be higher. This effect is explained by the temperature dependence of the dynamic viscosity. When the dynamic viscosity decreases with respect to increasing temperature, the result is a decreased strain rate. The decreased strain rate in return effects the thickness, height, and mass of the ligament.

Dilution, the only varied gas flow rate in this project is also shown to have an effect on the aerosol concentration. The dilution effects can be seen by increasing the dilution gas flow rate while holding the oil feed rate and temperature constant. As the dilution gas flow rate increases, the oil concentration in the aerosol decreases as one would expect.

A discussion is also presented regarding the general applications of atomization and how past researchers have developed and advanced the theories of atomization. Included in this discussion is a clear and concise definition of an aerosol, an introduction to past models of oil consumption, and the conditions needed for aerosols to form within the ring-pack of a piston.

CHAPTER 8

FUTURE AND EXTENDED RESEARCH

In this current work, the theoretical physics-based model has been used to simulate aerosol generation based on a single oil with specific relationships for the oil properties: density, viscosity, and surface tension and their dependence on temperature and strain rate. Therefore, future research could investigate variations in oil property relationships and how they affect aerosol generation.

Also, in this current project, a single orifice size and nitrogen gas flowrate were modeled. Therefore, future research could investigate the effects of orifice size and nitrogen gas flow rate on aerosol generation.

Furthermore, in this current research, aerosol generation was modeled at three different temperatures and at a single pressure differential across the orifice. Therefore, future research could also further investigate the effects of temperature and pressure differential on aerosol generation.

APPENDIX A ---Correspondence from ATS RheoSystems to CK Engineering

ATS RheoSystems

Thursday April 1, 2010

Dr. Kwame Duho
CK Engineering
1116 Holloway Rd.
Ballwin, MO 63011

Dear Kwame,

We have completed the rheological study on the DEO Oil you sent to us. Capillary Rheometry measurements were conducted using a R1000 Single Bore Capillary Rheometer. Experiments were performed using a 0.156 mm diameter die with a 65 mm length. Data was collected at temperatures of 50, 100, and 150°C. Both a 3.5 and a 35 MPa pressure transducer were used to cover a range of shear rates from 10,000 to 1,000,000 s^{-1}.

Data Summary:

The DEO Oil shear viscosity profile was studied in the shear rate range 10,000 to 1,000,000 s^{-1}. The experiments were performed at 50, 100 and 150°C using Capillary Rheometry. The DEO Oil shows a decrease in viscosity with increasing temperature and is also seen to exhibit shear thinning i.e. decrease in viscosity with increasing shear rate. The degree of shear thinning decreases with increasing temperature.

Sample Preparation:

The DEO Oil sample was tested as received and loaded into the Single Bore barrel at the desired test temperature. The Oil was then packed, tightly, into a homogenous mass using the drive piston. This was done in order to eliminate air bubbles from the barrel. A 15 minute thermal equilibrium hold ensured the sample was thermally equated.

REOLOGICA Instruments Guarantee
The results generated in this report by this model of rheometer can be routinely reproduced when used under the same laboratory conditions anywhere in the world

Web: www.atsrheosystems.com ▼ Email: info@atsrheosystems.com
Headquarters: 231 Crosswicks Road, Bordentown, NJ 08505 Tel: 609 298 2522 Fax: 609 298 2795
Satellite Office: 5240 Whitsett Ave., Suite 12, Valley Village, CA 91607 Tel/Fax: 818 753 2960

Experimental Setup and Discussion:

As with all of our consulting and contract testing, the analysis of a known sample was performed to confirm the calibration and performance of the instrument. For the 0.156 by 65 mm capillary geometry, a VRM5 Newtonian oil with a nominal viscosity of 0.005956 Pa s at 100°C was used as the standard and the results are presented in Figure 1. All relevant rheological values are within acceptable limits. The instrument calibration was also verified at 150°C using a Tannas R-400 viscosity standard, however, the data was omitted for brevity.

All testing experiments were performed using a 0.156 x 65 mm die geometry.

For the shear rate range in this study, capillary rheometry experiments were performed at 50, 100 and 150°C. The low temperature end was set at 50°C since this is the software limited, controllable low temperature operating limit for our current Capillary Rheometer (room temperature measurements are also possible). The experimental shear rate was increased from 10,000 to 1,000,000 by increasing the drive piston speed. At each test shear rate in this range the steady state pressure drop was measured using the transducer. The piston speed and measured pressure drop were then used to calculate the shear rate and shear stress for the fluid, respectively. The fluid viscosity is determined from the ratio of the shear stress to the shear rate.

The measured viscosity profiles are presented in Figure 2. From Figure 2, the DEO Oil is seen to show a temperature dependent viscosity profile. The sample viscosity decreases with increasing temperature. The DEO Oil also exhibits shear thinning behavior i.e. the sample viscosity decreases with increasing shear rate. The shear thinning behavior is more pronounce at high shear rates while the fluid viscosity approaches a zero shear value at low shear rates. In addition, the degree of shear thinning decreases with increasing temperature. The power law index (in the high shear rate region) is 0.77 at 50°C as compared to 0.89 at 100°C and 0.96 at 150°C.

Conclusion

The flow profile of the DEO Oil was investigated using Capillary Rheometry experiments. The DEO Oil exhibited a temperature dependent viscosity profile as well as shear thinning. The degree of shear thinning was seen to decrease with increasing temperature.

Web: www.atsrheosystems.com ▼ Email: info@atsrheosystems.com
Headquarters: 231 Crosswicks Road, Bordentown, NJ 08505 Tel: 609 298 2522 Fax: 609 298 2795
Satellite Office: 5240 Whitsett Ave., Suite 12, Valley Village, CA 91607 Tel/Fax: 818 753 2960

Clearly, the R1000 Single Bore Capillary Rheometer is ideally suited for the characterization of the rheological behavior of this type of sample.

As with any sophisticated analytical instrument, the organization and staff are equally as important as the quality of the equipment. In light of this, we have included ATS RheoSystems' Statement of Qualifications with this hard copy of the report.

We will follow up with you in the next few days to discuss these results and possibility to further this project with the execution of additional experiments and/or the purchase of a Capillary Rheometer.

Sincerely,

Dr. Kenneth K. Aniunoh
Staff Engineer

E-Mail: info@atsrheosystems.com
Visit our Web site @ http://www.atsrheosystems.com

DEO at 50C	
Shear rate	Viscosity
10001.387	0.0486183
15845.779	0.048199
25105.326	0.0449606
39922.907	0.0454626
63094.836	0.0436842
100011.95	0.0412951
158455.87	0.0398928
251059.02	0.0374414
399225.23	0.0343071
630940.68	0.0311321
1000121.4	0.0272454
1358187.9	0.0244407

DEO at 100C	
Shear rate	Viscosity
10001.387	0.0128732
15845.779	0.0127005
25105.326	0.0126965
39922.907	0.0124928
63094.836	0.0122831
100011.95	0.012511
158455.87	0.0120696
251059.02	0.0121215
399225.23	0.0116821
630940.68	0.0109855
1000121.4	0.0104387
1358187.9	0.0100139

DEO at 115C	
Shear rate	Viscosity
10001.387	0.0105157
15845.779	0.0103644
25105.326	0.0103298
39922.907	0.0101584
63094.836	0.0099836
100011.95	0.0100832
158455.87	0.00979
251059.02	0.0097408
399225.23	0.0094212
630940.68	0.0089068
1000121.4	0.0085118
1358187.9	0.0082203

DEO at 150C	
Shear rate	Viscosity
10001.387	0.0052977
15845.779	0.0051935
25105.326	0.0050915
39922.907	0.0049915
63094.836	0.004894
100011.95	0.0047094
158455.87	0.0047445
251059.02	0.0044715
399225.23	0.0044171
630940.68	0.004306
1000121.4	0.0042469
1358187.9	0.0042502

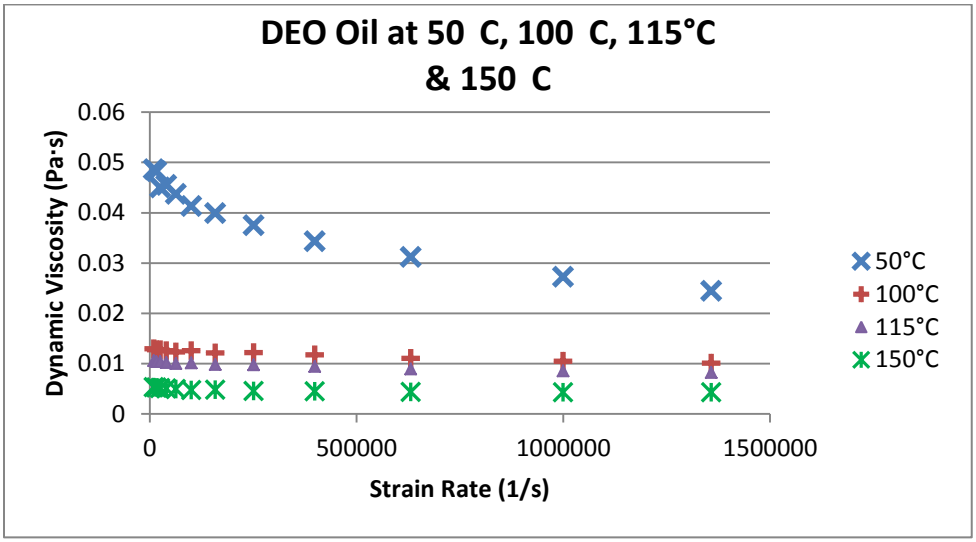

APPENDIX B ---RESULTS

Test Number	1
Experimental Total Time (s)	600
Oil Feed Rate (mL/hr)	0.5
Room Temp (K)	291.78
Fixture Temp (K)	389.49
Meter Temp (K)	299.79
Gas Dilution Flow Rate (L/min.)	11.617
Gas Flow rate (L/min.)	0.092

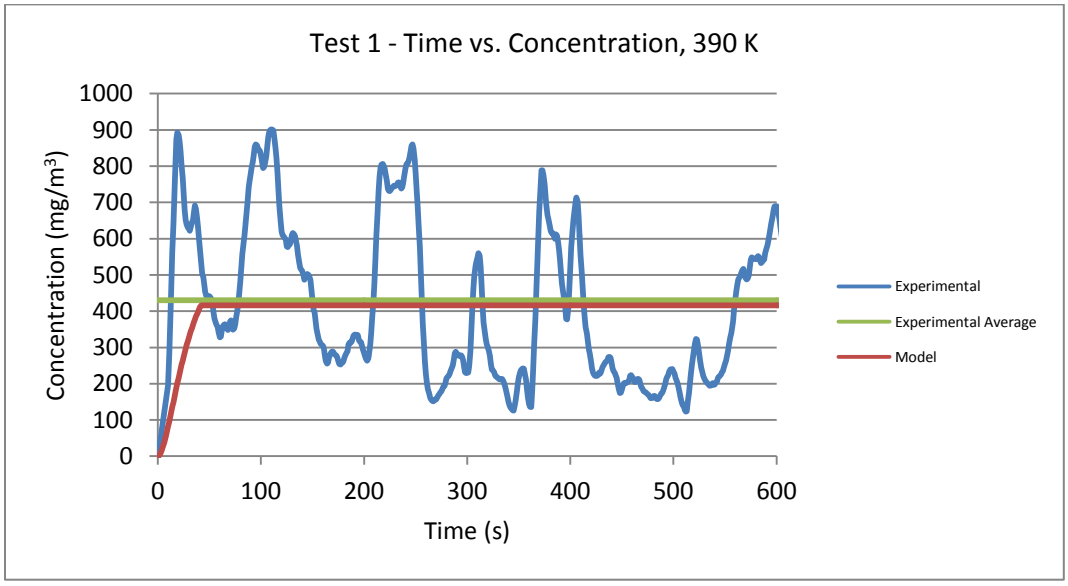

Test Number	2
Experimental Total Time (s)	600
Oil Feed Rate (mL/hr)	0.5
Room Temp (K)	291.78
Fixture Temp (K)	389.16
Meter Temp (K)	299.76
Gas Dilution Flow Rate (L/min.)	16.977
Gas Flow rate (L/min.)	0.092

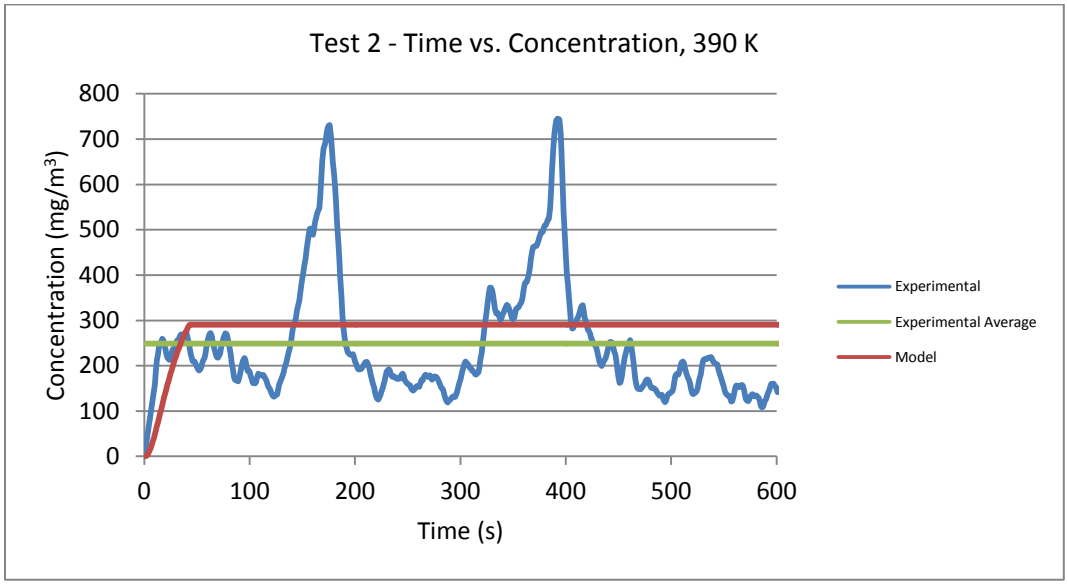

Test Number	3
Experimental Total Time (s)	600
Oil Feed Rate (mL/hr)	0.5
Room Temp (K)	291.78
Fixture Temp (K)	422.21
Meter Temp (K)	300.31
Gas Dilution Flow Rate (L/min.)	10
Gas Flow rate (L/min.)	0.092

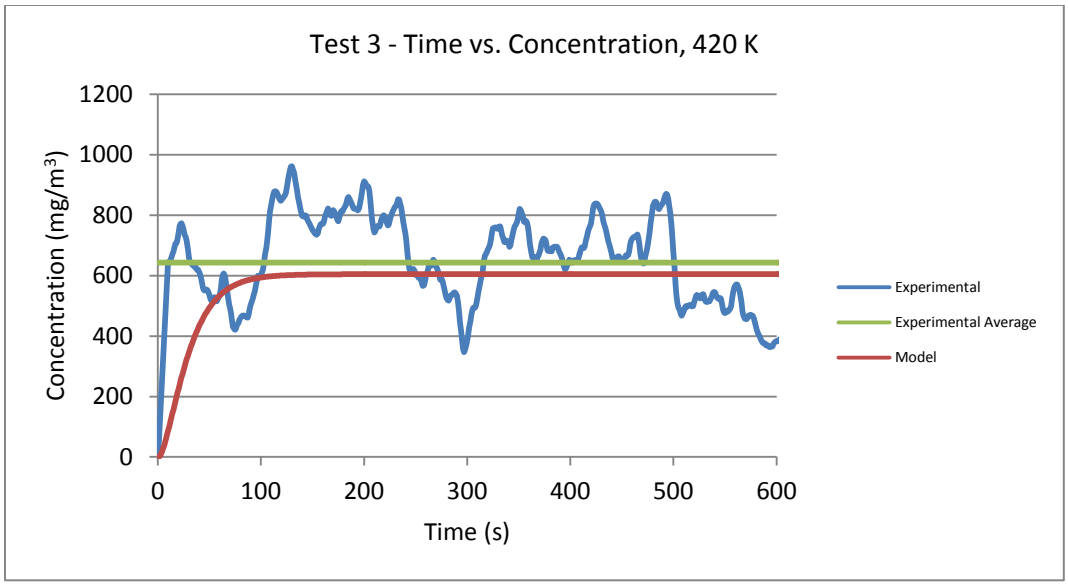

Test Number	4
Experimental Total Time (s)	600
Oil Feed Rate (mL/hr)	0.5
Room Temp (K)	291.78
Fixture Temp (K)	421.96
Meter Temp (K)	300.24
Gas Dilution Flow Rate (L/min.)	16.977
Gas Flow rate (L/min.)	0.092

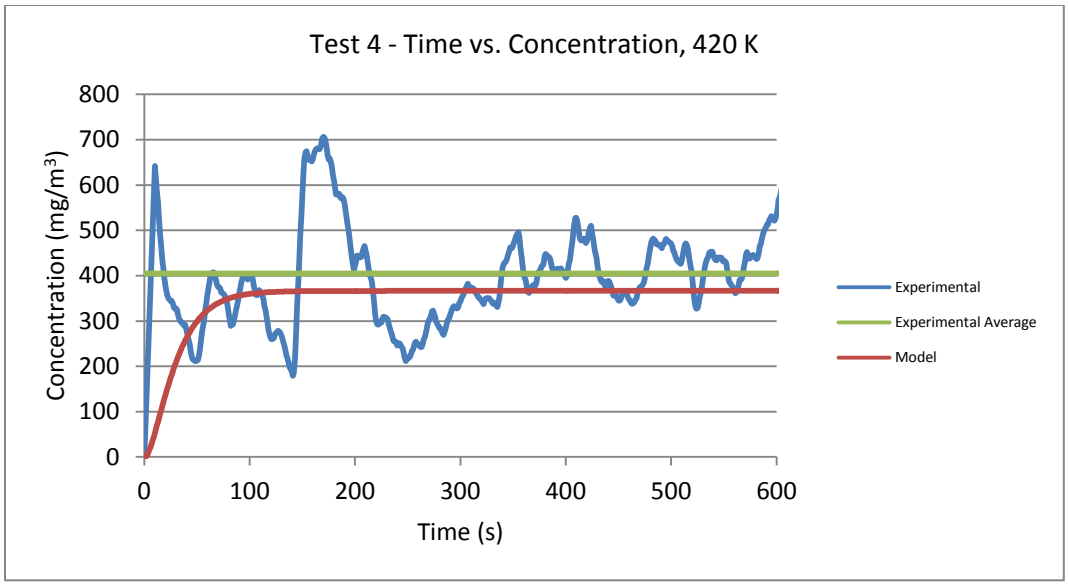

Test Number	5
Experimental Total Time (s)	550
Oil Feed Rate (mL/hr)	0.5
Room Temp (K)	291.78
Fixture Temp (K)	423.07
Meter Temp (K)	306.13
Gas Dilution Flow Rate (L/min.)	20
Gas Flow rate (L/min.)	0.092

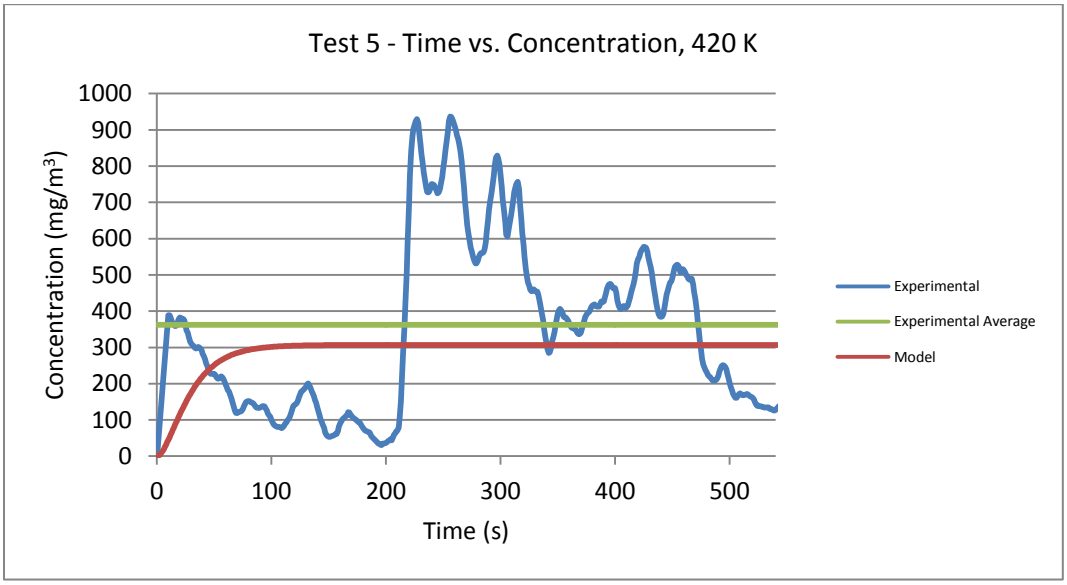

Test Number	6
Experimental Total Time (s)	375
Oil Feed Rate (mL/hr)	0.5
Room Temp (K)	291.78
Fixture Temp (K)	471.29
Meter Temp (K)	307.71
Gas Dilution Flow Rate (L/min.)	20
Gas Flow rate (L/min.)	0.092

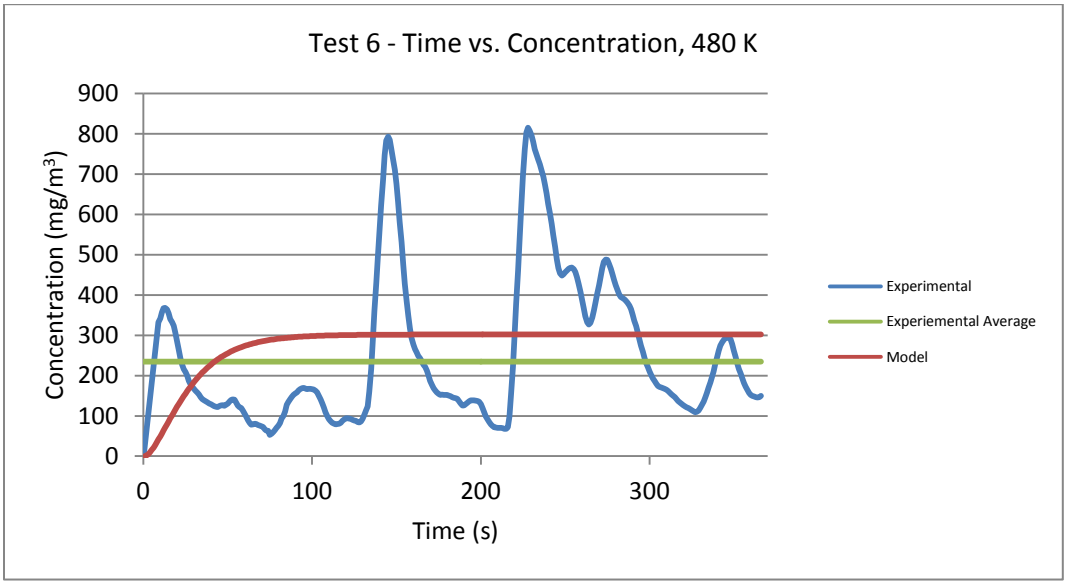

Test Number	7
Experimental Total Time (s)	600
Oil Feed Rate (mL/hr)	0.5
Room Temp (K)	291.78
Fixture Temp (K)	390.48
Meter Temp (K)	305.15
Gas Dilution Flow Rate (L/min.)	5
Gas Flow rate (L/min.)	0.092

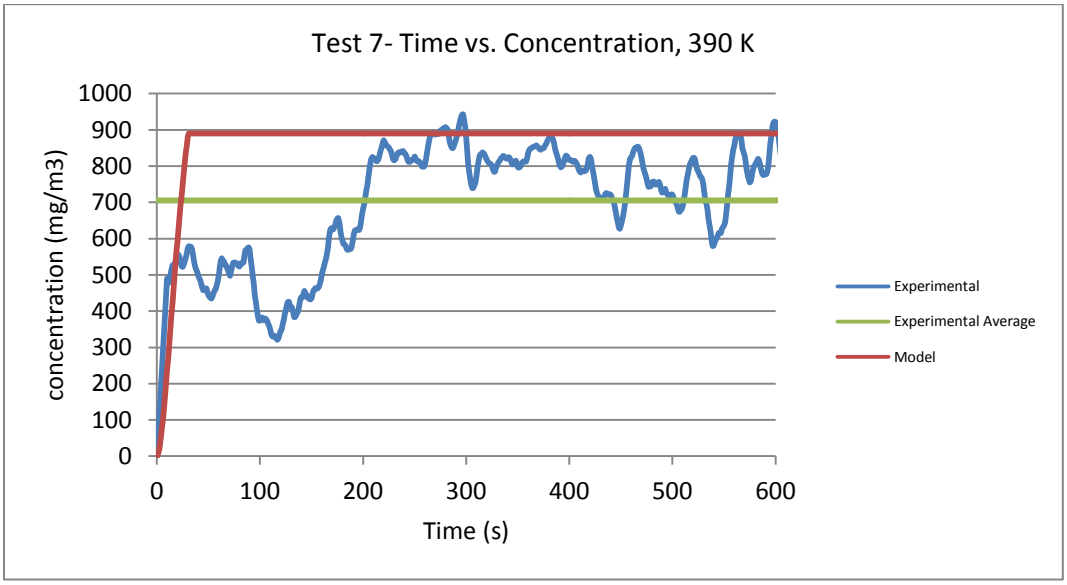

Test Number	8
Experimental Total Time (s)	600
Oil Feed Rate (mL/hr)	0.5
Room Temp (K)	291.78
Fixture Temp (K)	473.18
Meter Temp (K)	305.64
Gas Dilution Flow Rate (L/min.)	25
Gas Flow rate (L/min.)	0.092

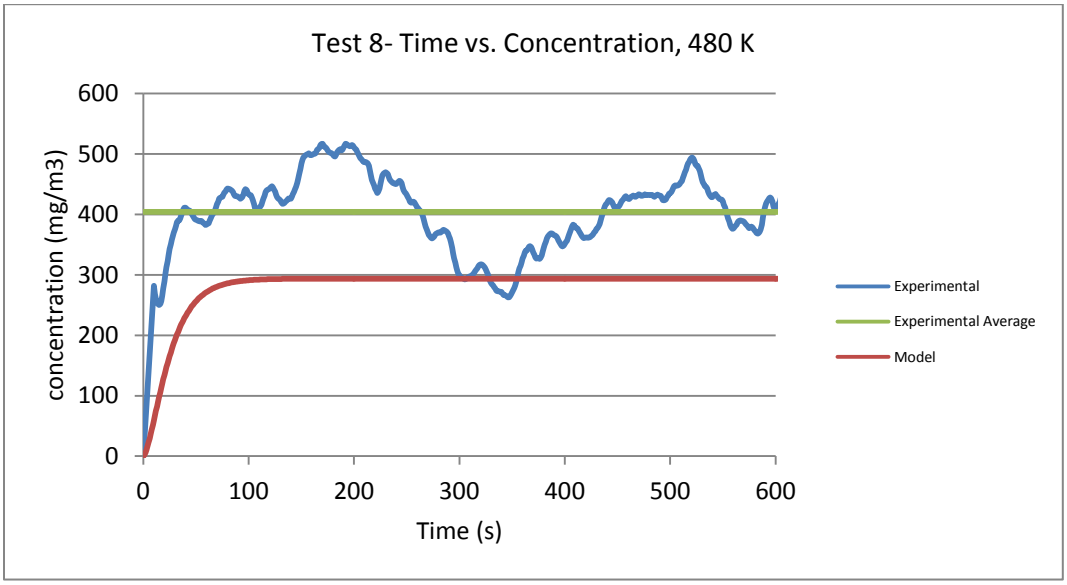

Test Number	9
Experimental Total Time (s)	600
Oil Feed Rate (mL/hr)	0.65
Room Temp (K)	291.78
Fixture Temp (K)	389.56
Meter Temp (K)	299.51
Gas Dilution Flow Rate (L/min.)	10
Gas Flow rate (L/min.)	0.092

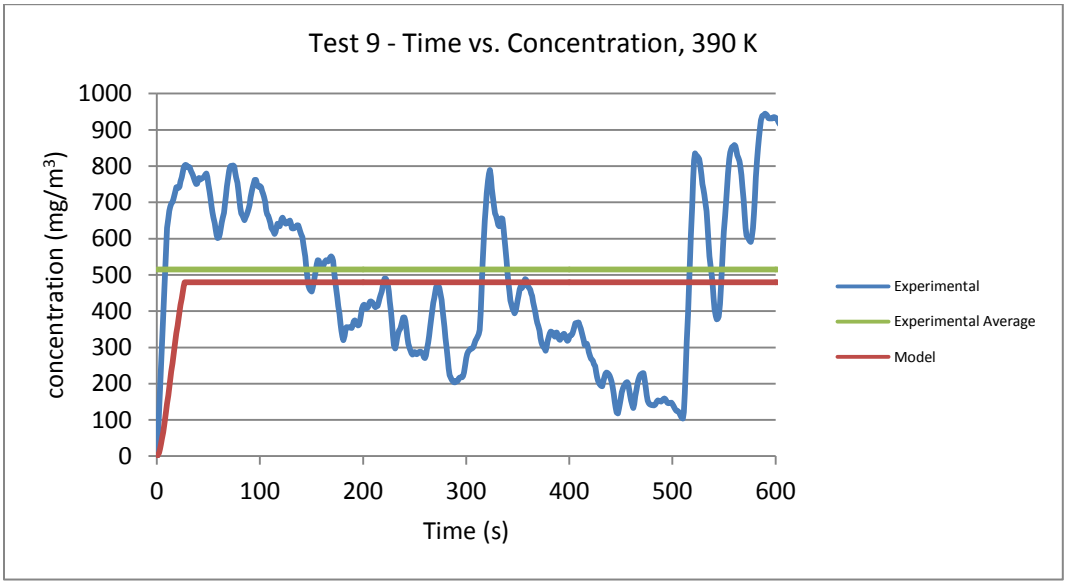

Test Number	10
Experimental Total Time (s)	600
Oil Feed Rate (mL/hr)	0.65
Room Temp (K)	291.78
Fixture Temp (K)	389.23
Meter Temp (K)	299.24
Gas Dilution Flow Rate (L/min.)	11.617
Gas Flow rate (L/min.)	0.092

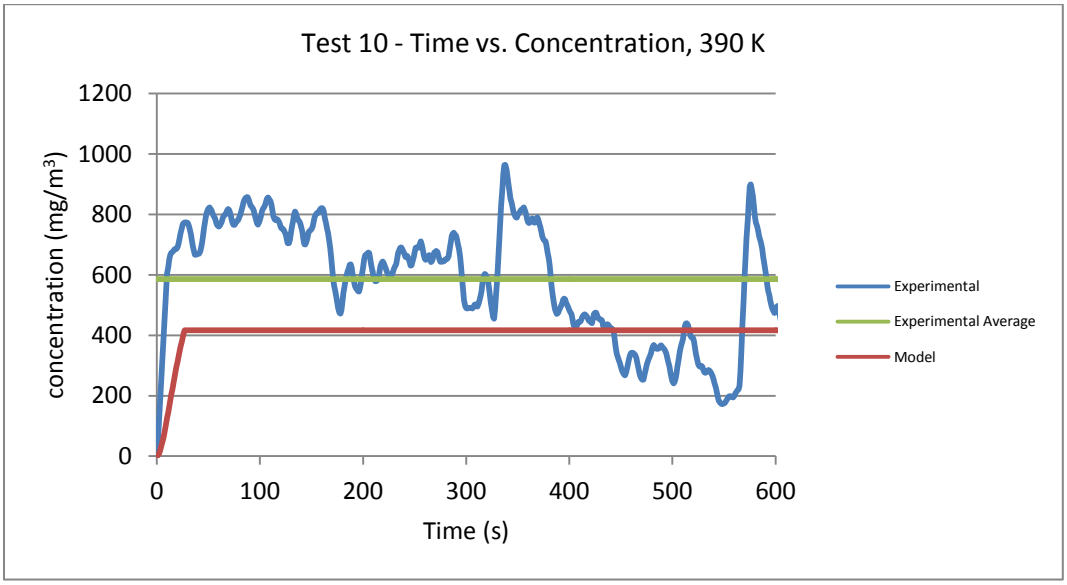

Test Number	11
Experimental Total Time (s)	600
Oil Feed Rate (mL/hr)	0.65
Room Temp (K)	291.78
Fixture Temp (K)	389.25
Meter Temp (K)	299.77
Gas Dilution Flow Rate (L/min.)	15
Gas Flow rate (L/min.)	0.092

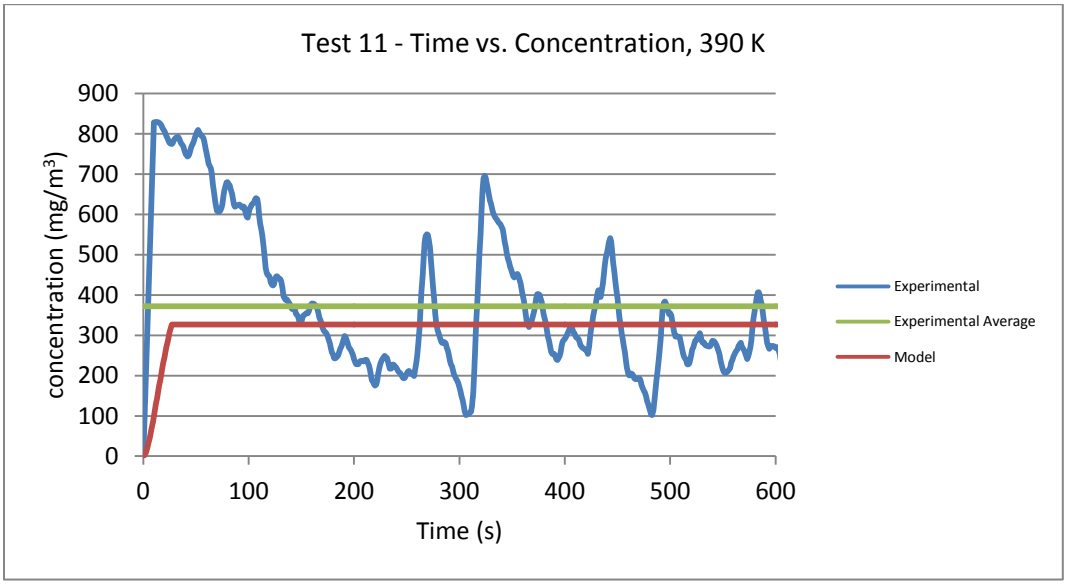

Test Number	12
Experimental Total Time (s)	600
Oil Feed Rate (mL/hr)	0.65
Room Temp (K)	291.78
Fixture Temp (K)	389.51
Meter Temp (K)	299.25
Gas Dilution Flow Rate (L/min.)	16.977
Gas Flow rate (L/min.)	0.092

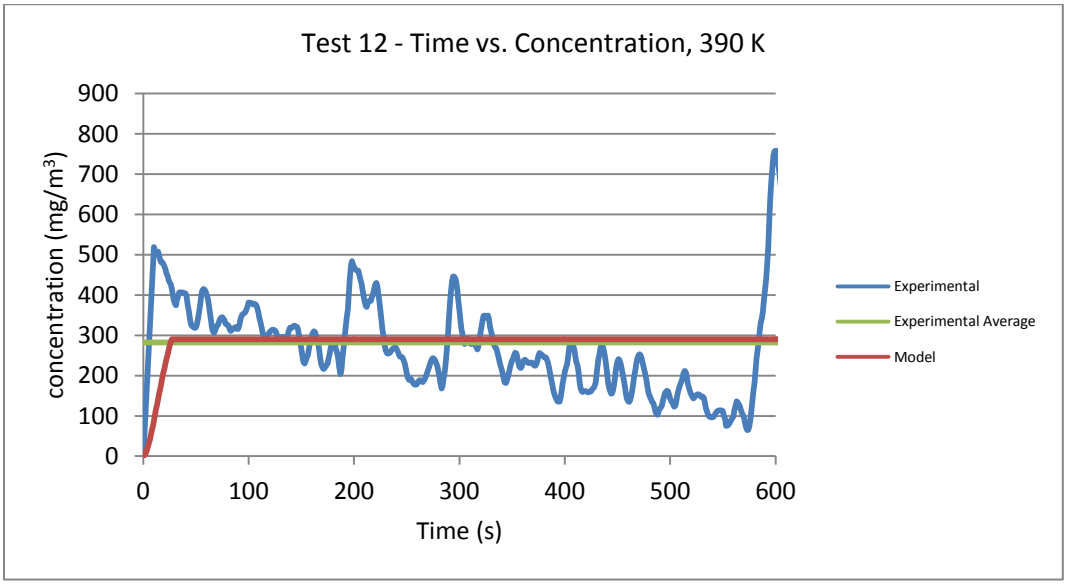

Test Number	13
Experimental Total Time (s)	600
Oil Feed Rate (mL/hr.)	0.65
Room Temp (K)	291.78
Fixture Temp (K)	391.6
Meter Temp (K)	303
Gas Dilution Flow Rate (L/min.)	20
Gas Flow rate (L/min.)	0.092

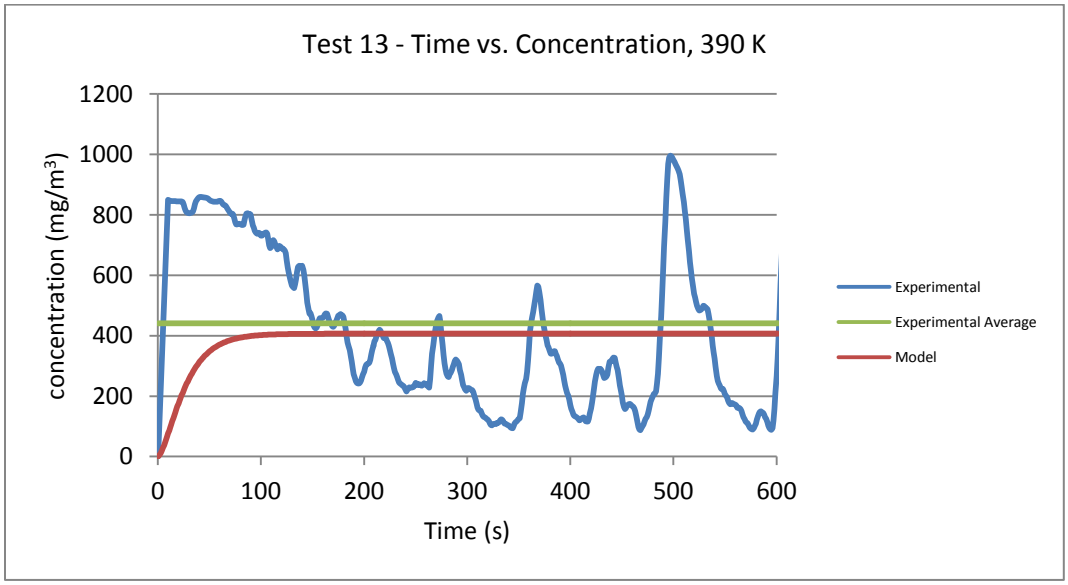

Test Number	14
Experimental Total Time (s)	600
Oil Feed Rate (mL/hr.)	0.65
Room Temp (K)	291.78
Fixture Temp (K)	480
Meter Temp (K)	303
Gas Dilution Flow Rate (L/min.)	36.617
Gas Flow rate (L/min.)	0.092

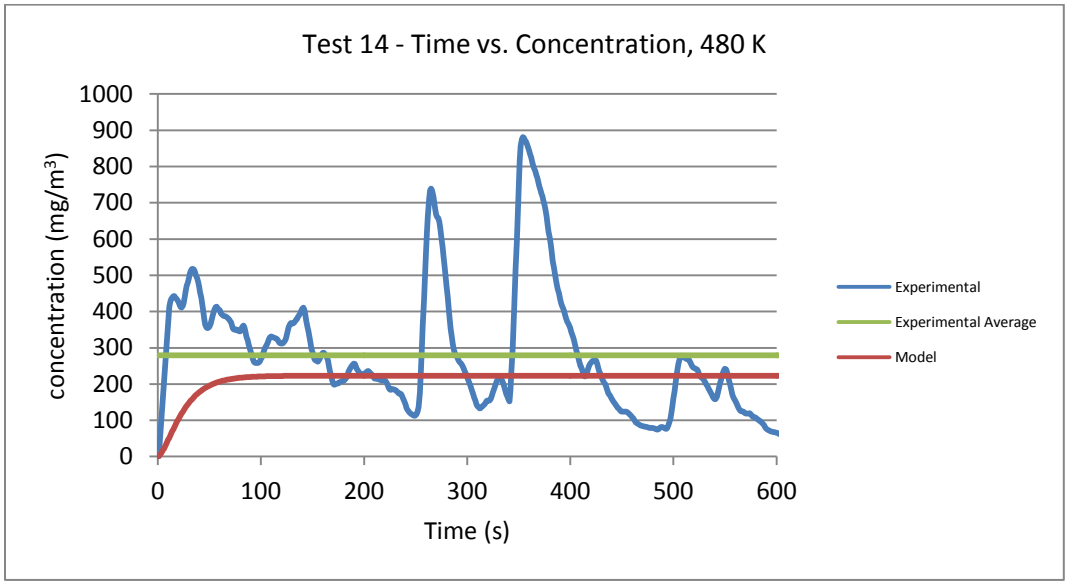

Test Number	15
Experimental Total Time (s)	600
Oil Feed Rate (mL/hr)	0.65
Room Temp (K)	291.78
Fixture Temp (K)	472.56
Meter Temp (K)	300.03
Gas Dilution Flow Rate (L/min.)	36.617
Gas Flow rate (L/min.)	0.092

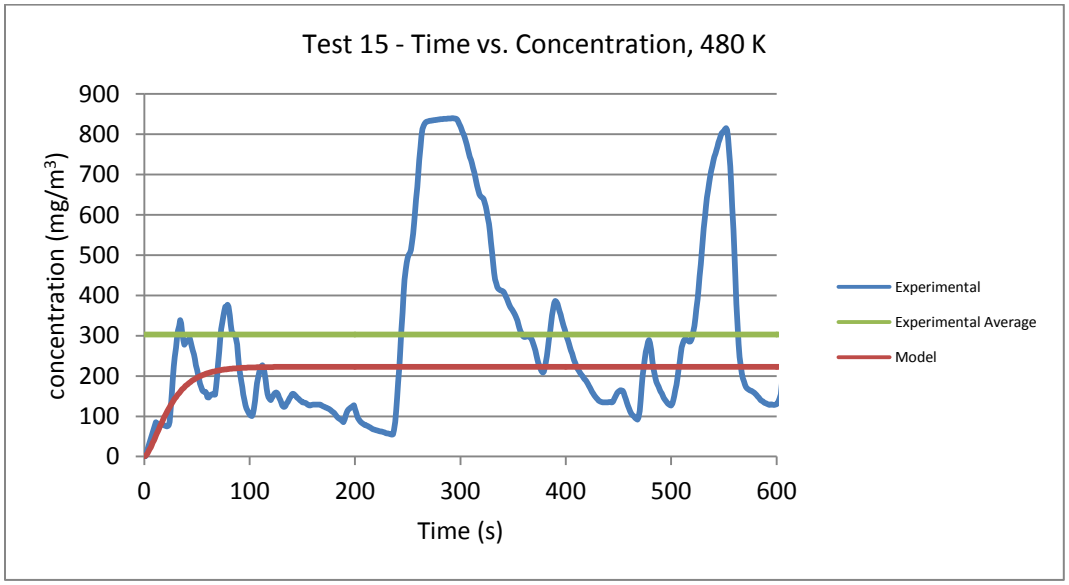

Test Number	16
Experimental Total Time (s)	600
Oil Feed Rate (mL/hr)	0.7
Room Temp (K)	291.78
Fixture Temp (K)	389.48
Meter Temp (K)	302.13
Gas Dilution Flow Rate (L/min.)	5.907
Gas Flow rate (L/min.)	0.092

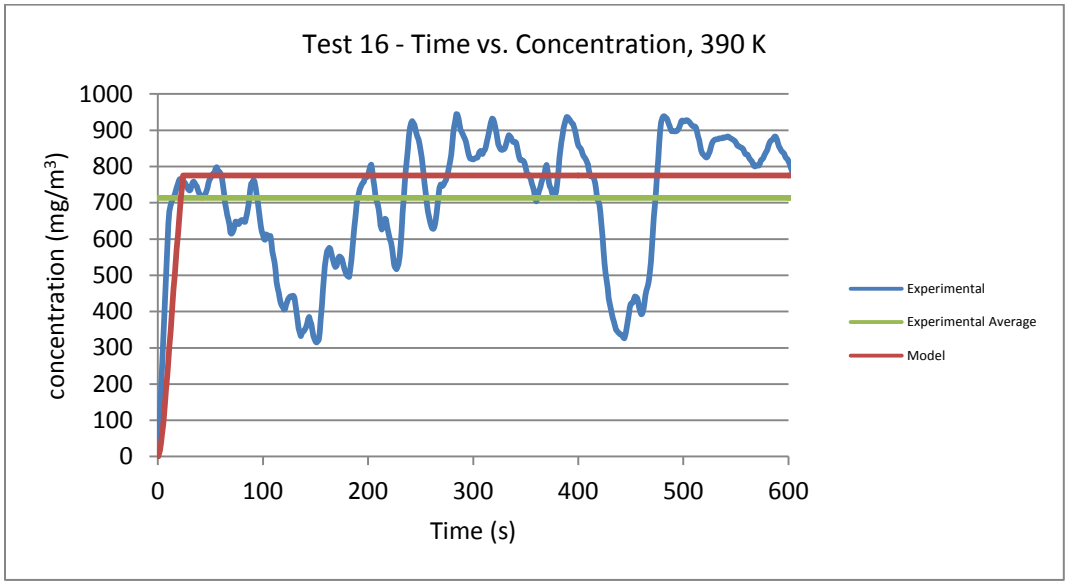

Test Number	17
Experimental Total Time (s)	600
Oil Feed Rate (mL/hr)	0.7
Room Temp (K)	291.78
Fixture Temp (K)	389.83
Meter Temp (K)	300.63
Gas Dilution Flow Rate (L/min.)	8.806
Gas Flow rate (L/min.)	0.092

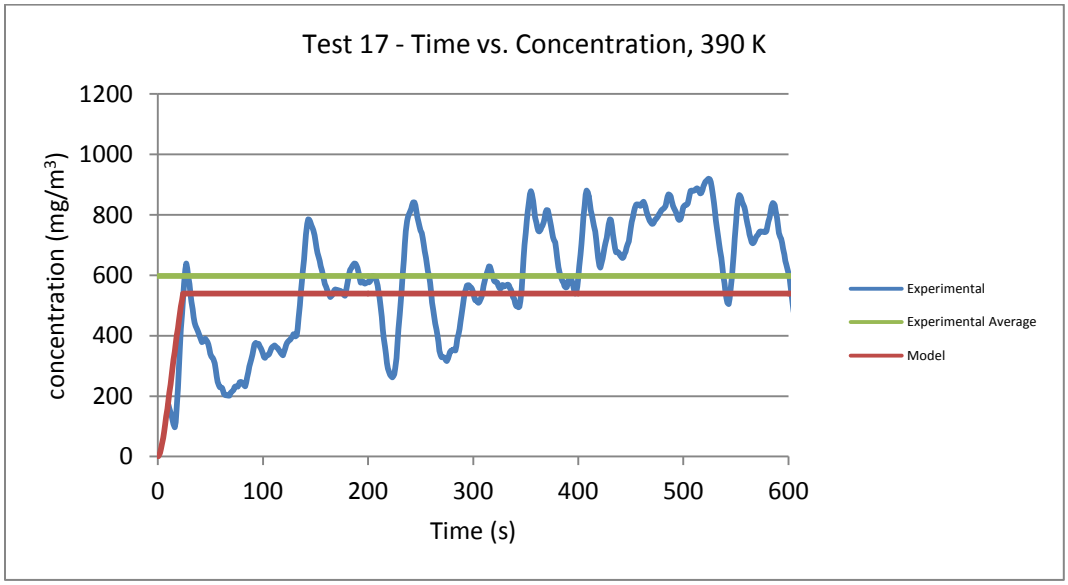

Test Number	18
Experimental Total Time (s)	600
Oil Feed Rate (mL/hr)	0.7
Room Temp (K)	291.78
Fixture Temp (K)	389.59
Meter Temp (K)	300.92
Gas Dilution Flow Rate (L/min.)	11.617
Gas Flow rate (L/min.)	0.092

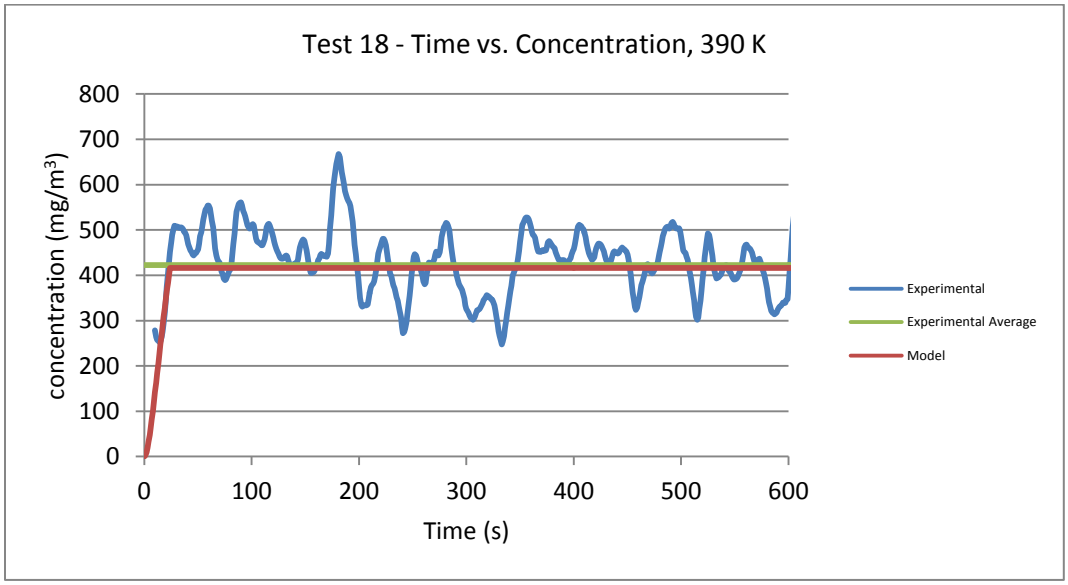

Test Number	19
Experimental Total Time (s)	600
Oil Feed Rate (mL/hr)	0.7
Room Temp (K)	291.78
Fixture Temp (K)	389.66
Meter Temp (K)	302.5
Gas Dilution Flow Rate (L/min.)	16.977
Gas Flow rate (L/min.)	0.092

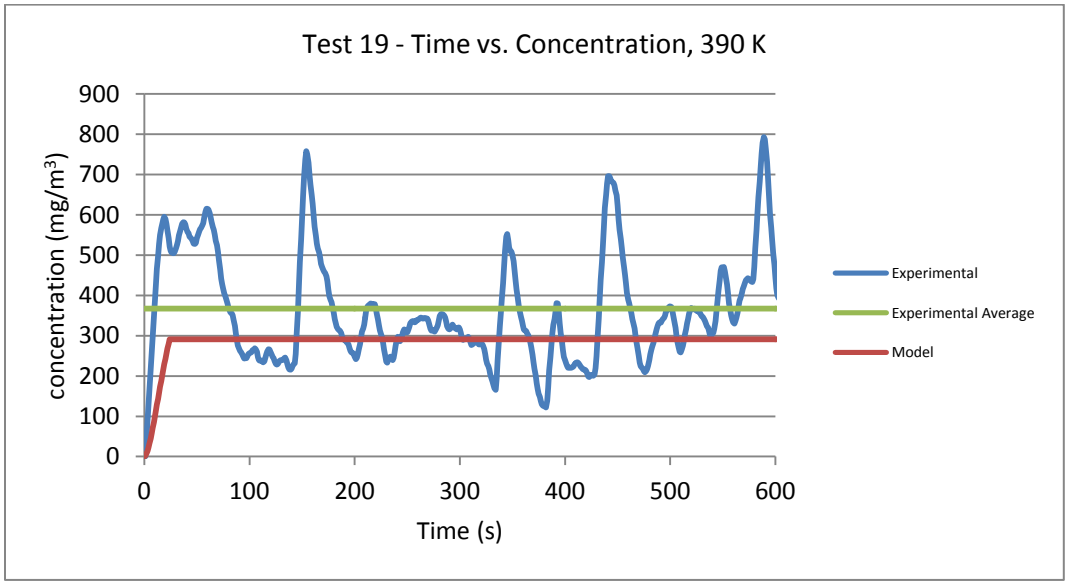

Test Number	20
Experimental Total Time (s)	600
Oil Feed Rate (mL/hr)	0.7
Room Temp (K)	291.78
Fixture Temp (K)	422.69
Meter Temp (K)	303.77
Gas Dilution Flow Rate (L/min.)	10
Gas Flow rate (L/min.)	0.092

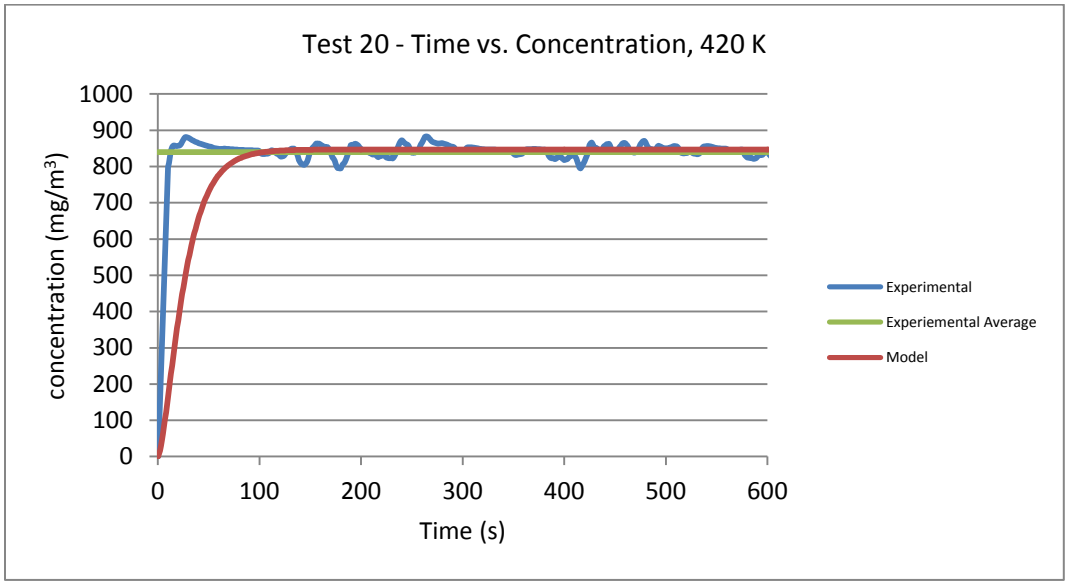

Test Number	21
Experimental Total Time (s)	600
Oil Feed Rate (mL/hr)	0.75
Room Temp (K)	291.78
Fixture Temp (K)	389.79
Meter Temp (K)	301.3
Gas Dilution Flow Rate (L/min.)	5.907
Gas Flow rate (L/min.)	0.092

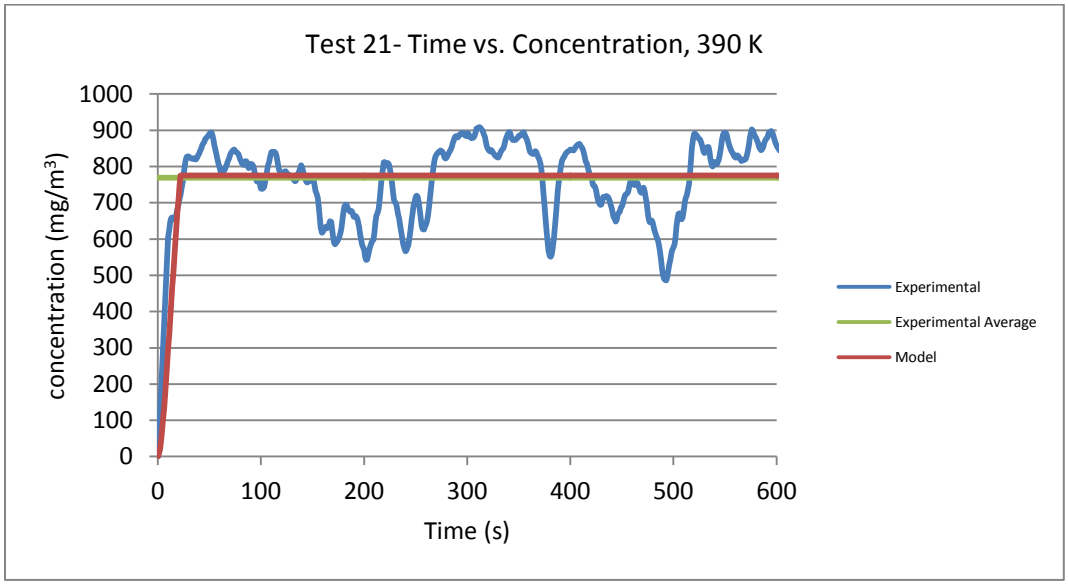

Test Number	22
Experimental Total Time (s)	600
Oil Feed Rate (mL/hr)	0.75
Room Temp (K)	291.78
Fixture Temp (K)	389.46
Meter Temp (K)	301.3
Gas Dilution Flow Rate (L/min.)	11.617
Gas Flow rate (L/min.)	0.092

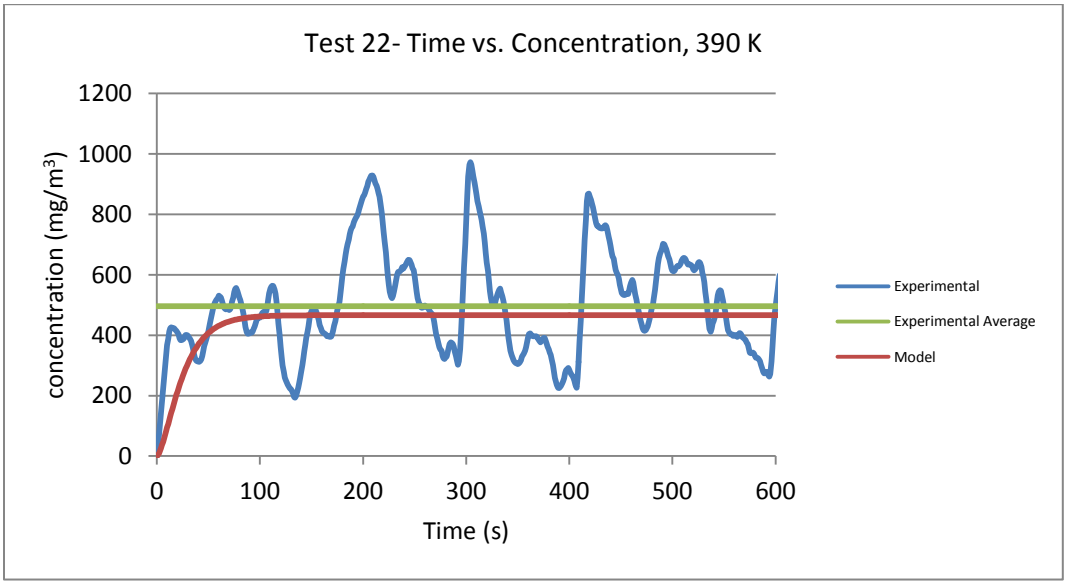

Test Number	23
Experimental Total Time (s)	400
Oil Feed Rate (mL/hr)	0.75
Room Temp (K)	291.78
Fixture Temp (K)	389.6
Meter Temp (K)	301.28
Gas Dilution Flow Rate (L/min.)	11.617
Gas Flow rate (L/min.)	0.092

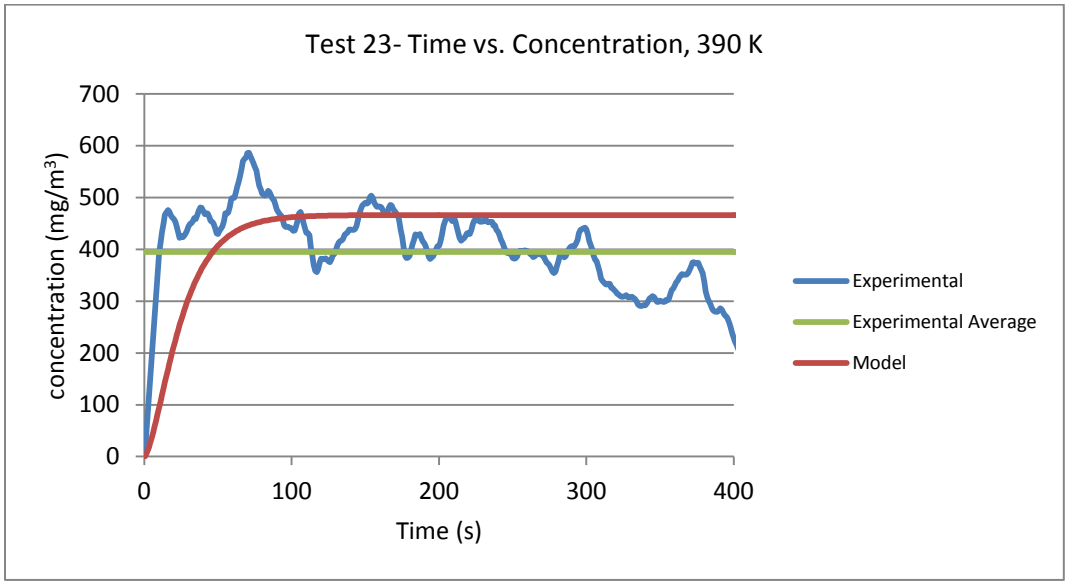

Test Number	24
Experimental Total Time (s)	600
Oil Feed Rate (mL/hr)	0.75
Room Temp (K)	291.78
Fixture Temp (K)	389.5
Meter Temp (K)	302.46
Gas Dilution Flow Rate (L/min.)	11.617
Gas Flow rate (L/min.)	0.092

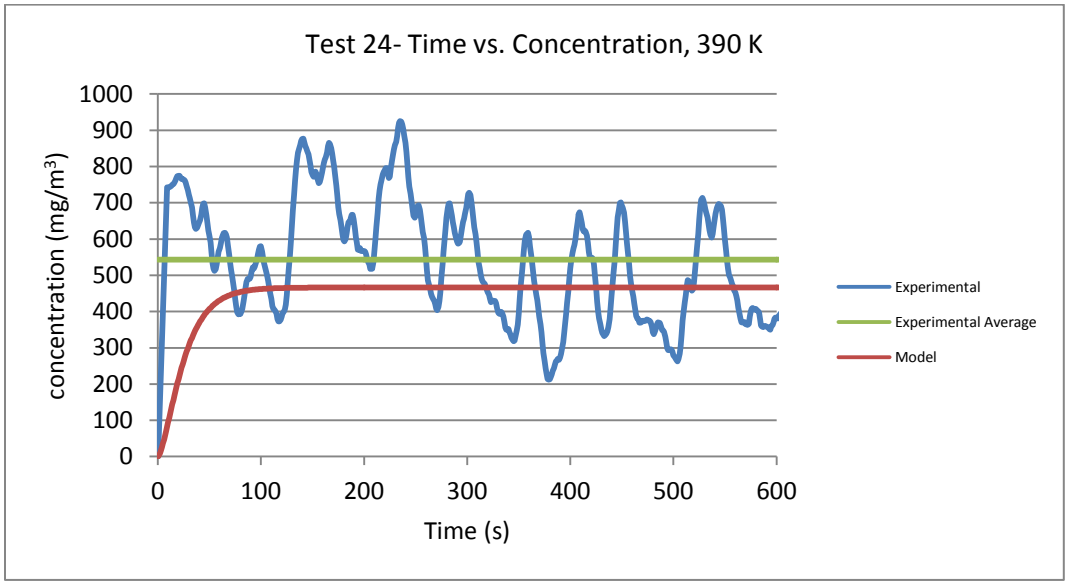

Test Number	25
Experimental Total Time (s)	600
Oil Feed Rate (mL/hr)	0.75
Room Temp (K)	291.78
Fixture Temp (K)	388.07
Meter Temp (K)	304.17
Gas Dilution Flow Rate (L/min.)	11.617
Gas Flow rate (L/min.)	0.092

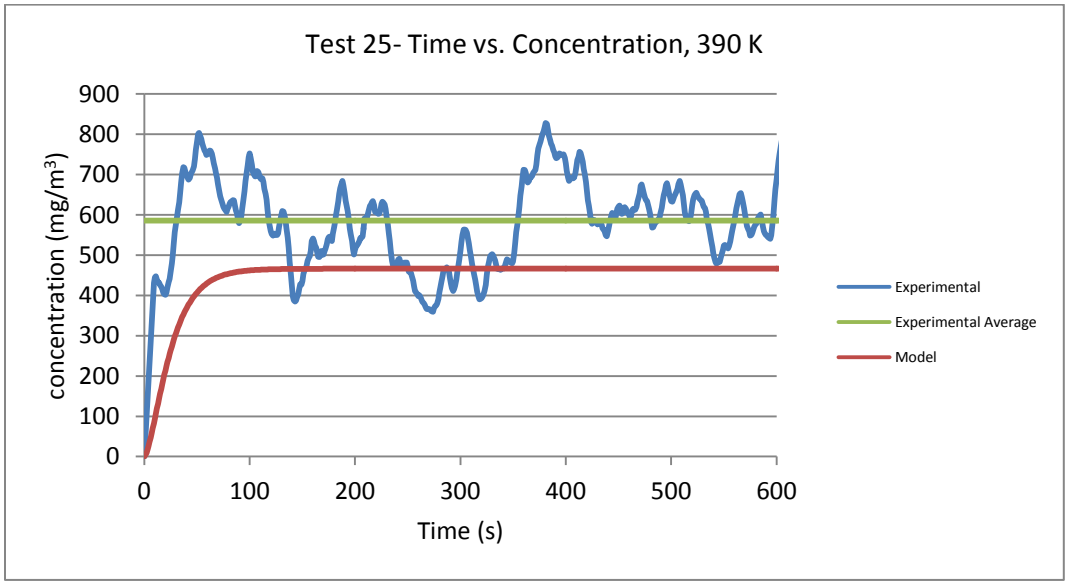

Test Number	26
Experimental Total Time (s)	600
Oil Feed Rate (mL/hr)	0.75
Room Temp (K)	291.78
Fixture Temp (K)	389.57
Meter Temp (K)	302.76
Gas Dilution Flow Rate (L/min.)	16.977
Gas Flow rate (L/min.)	0.092

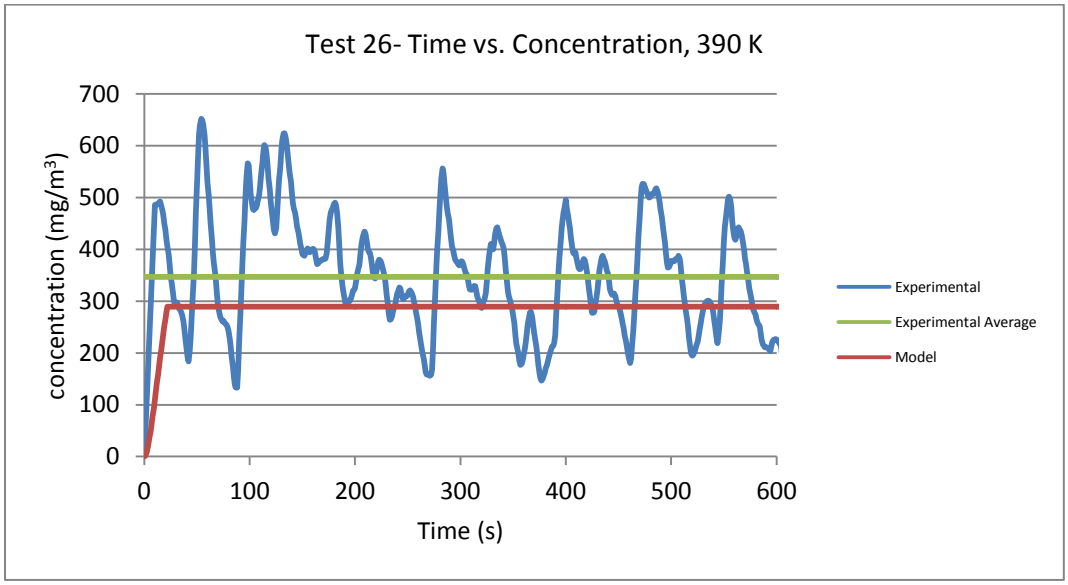

Test Number	27
Experimental Total Time (s)	600
Oil Feed Rate (mL/hr)	0.75
Room Temp (K)	291.78
Fixture Temp (K)	388.54
Meter Temp (K)	304.36
Gas Dilution Flow Rate (L/min.)	16.977
Gas Flow rate (L/min.)	0.092

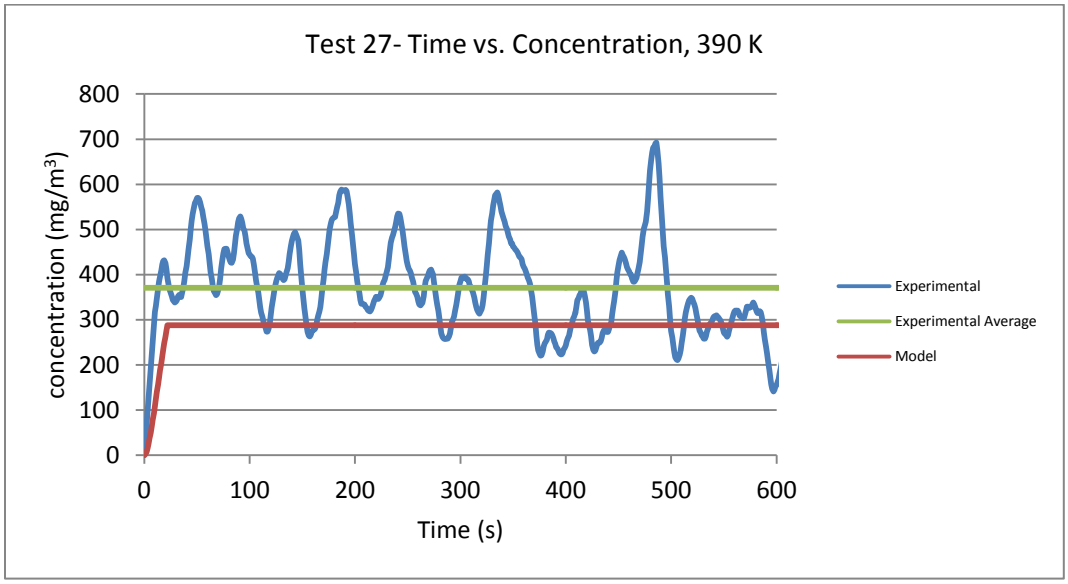

Test Number	28
Experimental Total Time (s)	600
Oil Feed Rate (mL/hr)	0.75
Room Temp (K)	291.78
Fixture Temp (K)	426.67
Meter Temp (K)	301.94
Gas Dilution Flow Rate (L/min.)	20
Gas Flow rate (L/min.)	0.092

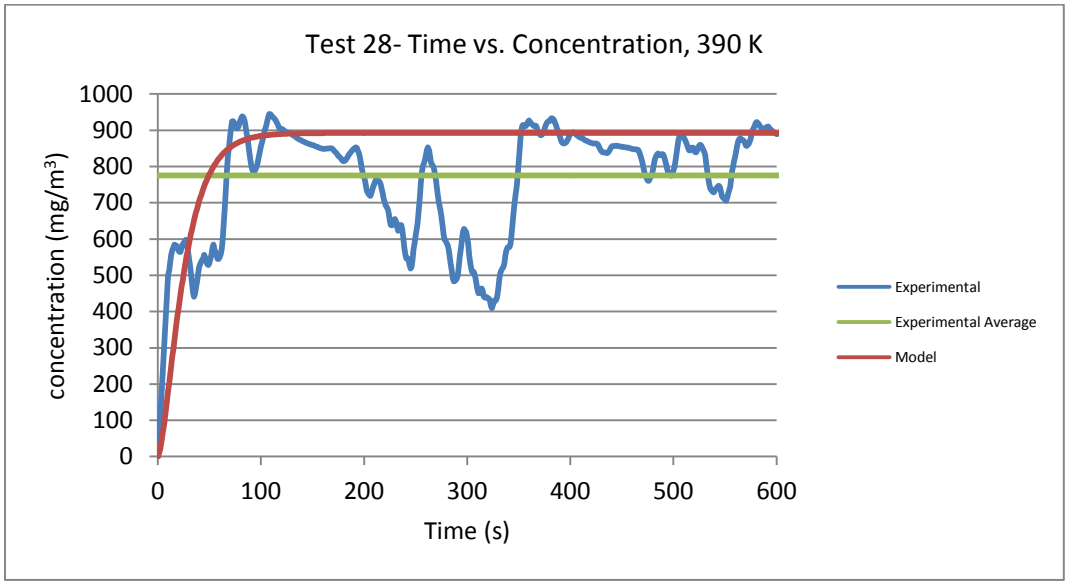

Test Number	29
Experimental Total Time (s)	600
Oil Feed Rate (mL/hr)	0.75
Room Temp (K)	291.78
Fixture Temp (K)	423.27
Meter Temp (K)	302.47
Gas Dilution Flow Rate (L/min.)	10
Gas Flow rate (L/min.)	0.092

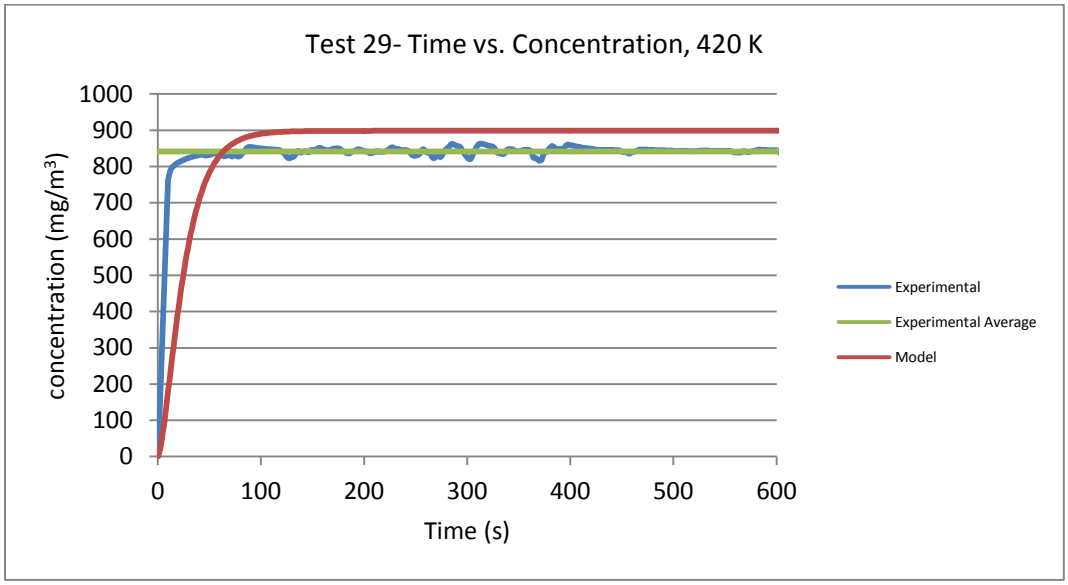

Test Number	30
Experimental Total Time (s)	600
Oil Feed Rate (mL/hr)	0.75
Room Temp (K)	291.78
Fixture Temp (K)	423
Meter Temp (K)	305.03
Gas Dilution Flow Rate (L/min.)	10
Gas Flow rate (L/min.)	0.092

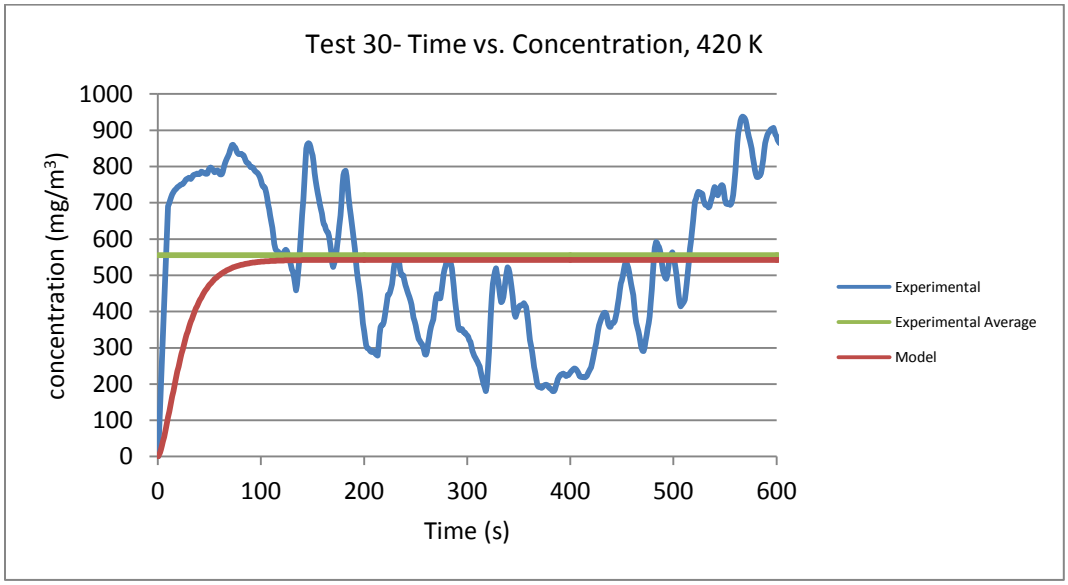

Test Number	31
Experimental Total Time (s)	500
Oil Feed Rate (mL/hr)	0.75
Room Temp (K)	291.78
Fixture Temp (K)	421.77
Meter Temp (K)	304.61
Gas Dilution Flow Rate (L/min.)	16.977
Gas Flow rate (L/min.)	0.092

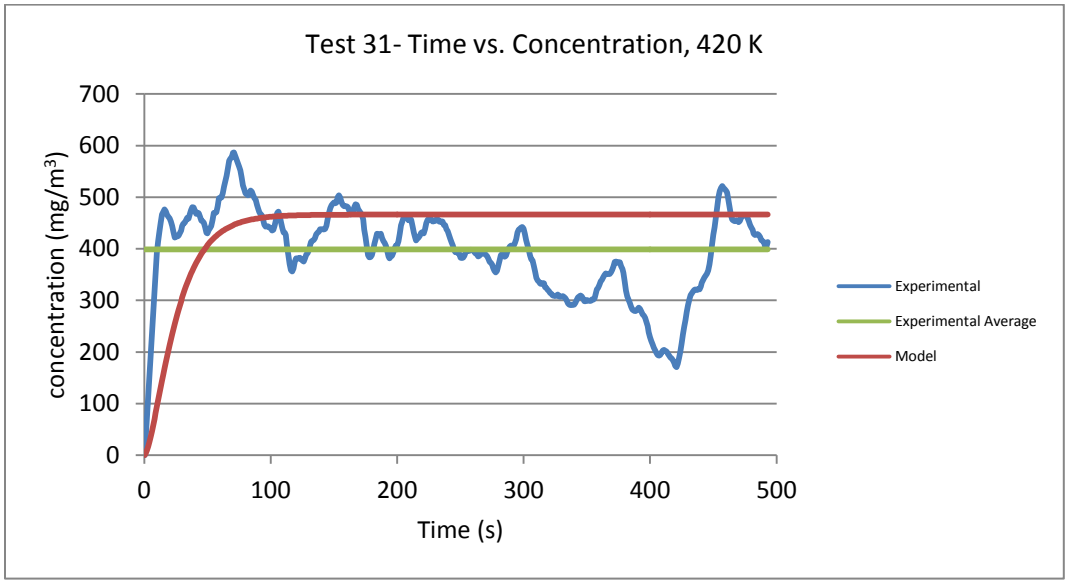

Test Number	32
Experimental Total Time (s)	500
Oil Feed Rate (mL/hr)	0.75
Room Temp (K)	291.78
Fixture Temp (K)	426.94
Meter Temp (K)	302.07
Gas Dilution Flow Rate (L/min.)	20
Gas Flow rate (L/min.)	0.092

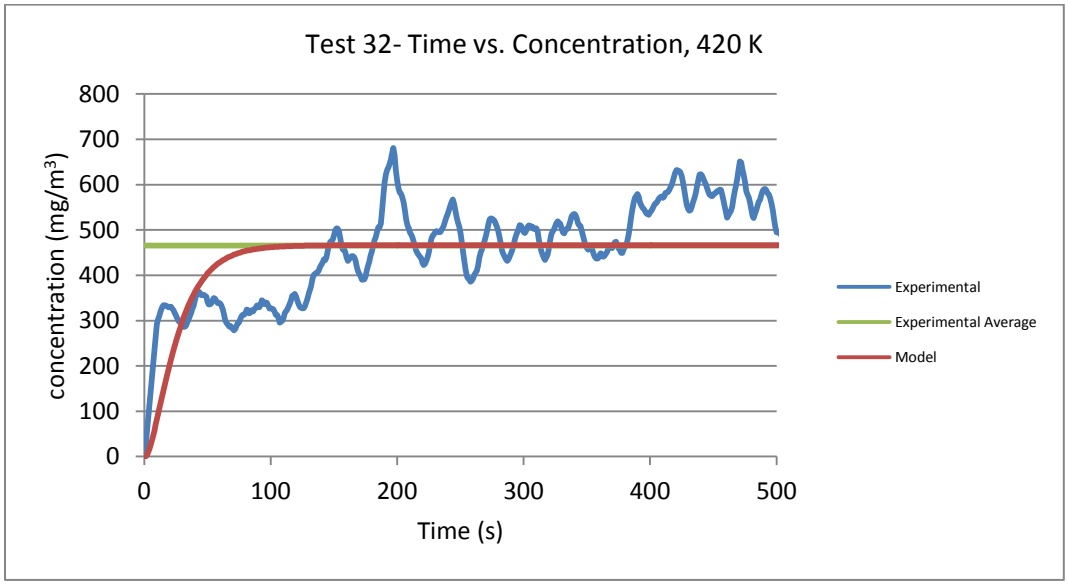

Test Number	33
Experimental Total Time (s)	600
Oil Feed Rate (mL/hr)	0.75
Room Temp (K)	291.78
Fixture Temp (K)	423
Meter Temp (K)	306.97
Gas Dilution Flow Rate (L/min.)	31
Gas Flow rate (L/min.)	0.092

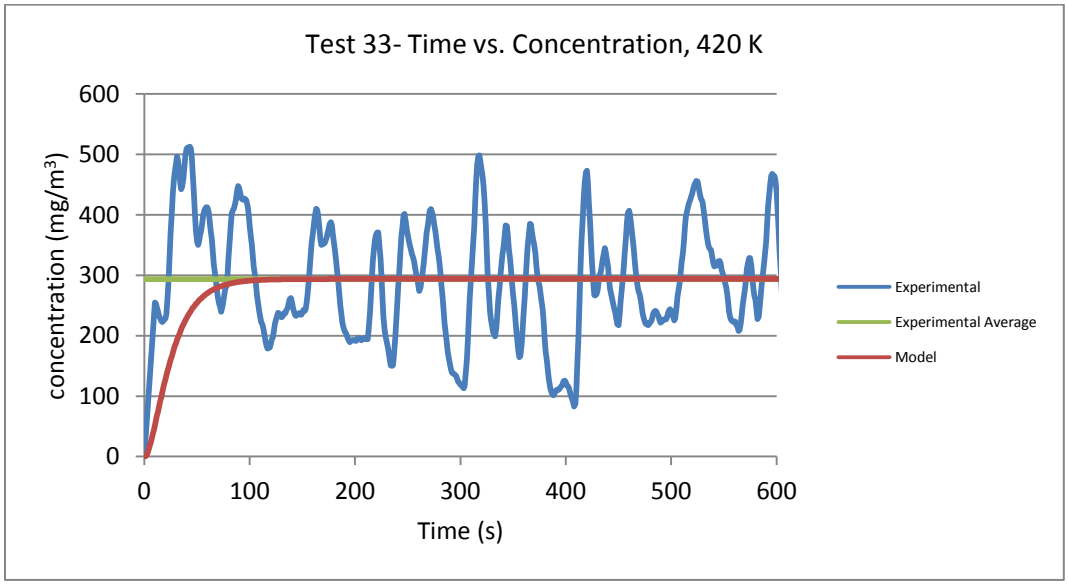

Test Number	34
Experimental Total Time (s)	600
Oil Feed Rate (mL/hr)	0.8
Room Temp (K)	291.78
Fixture Temp (K)	387.91
Meter Temp (K)	298.09
Gas Dilution Flow Rate (L/min.)	11.617
Gas Flow rate (L/min.)	0.092

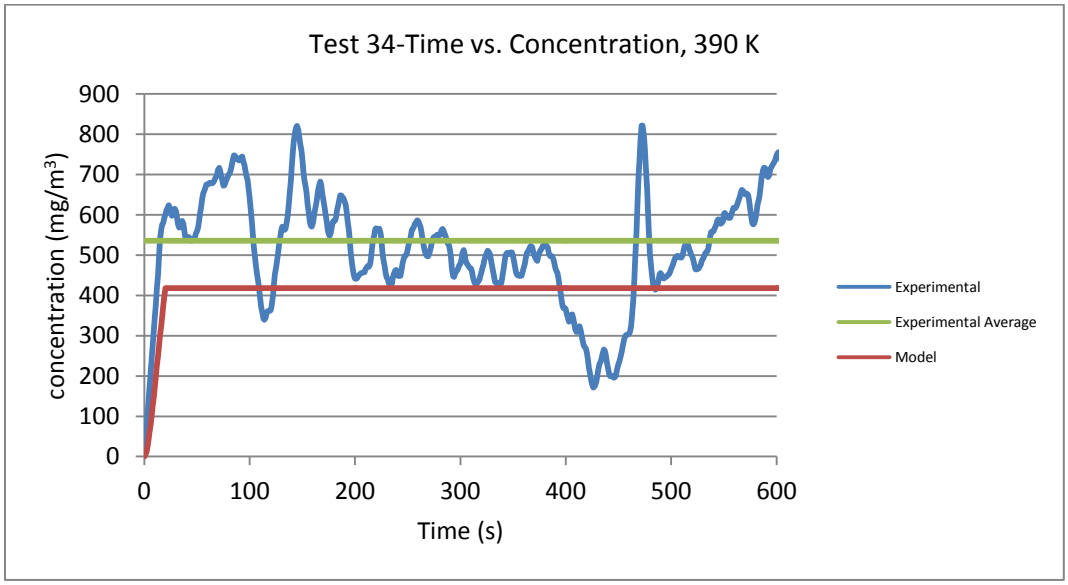

Test Number	35
Experimental Total Time (s)	600
Oil Feed Rate (mL/hr)	0.8
Room Temp (K)	291.78
Fixture Temp (K)	389.09
Meter Temp (K)	299.08
Gas Dilution Flow Rate (L/min.)	16.977
Gas Flow rate (L/min.)	0.092

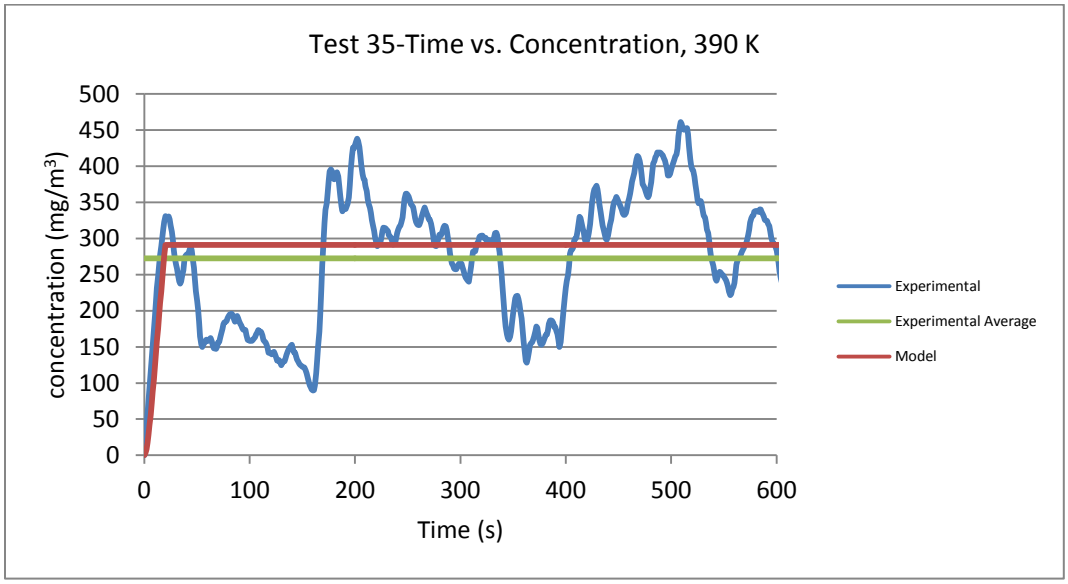

Test Number	36
Experimental Total Time (s)	600
Oil Feed Rate (mL/hr)	0.8
Room Temp (K)	291.78
Fixture Temp (K)	423.22
Meter Temp (K)	301.1
Gas Dilution Flow Rate (L/min.)	30.907
Gas Flow rate (L/min.)	0.092

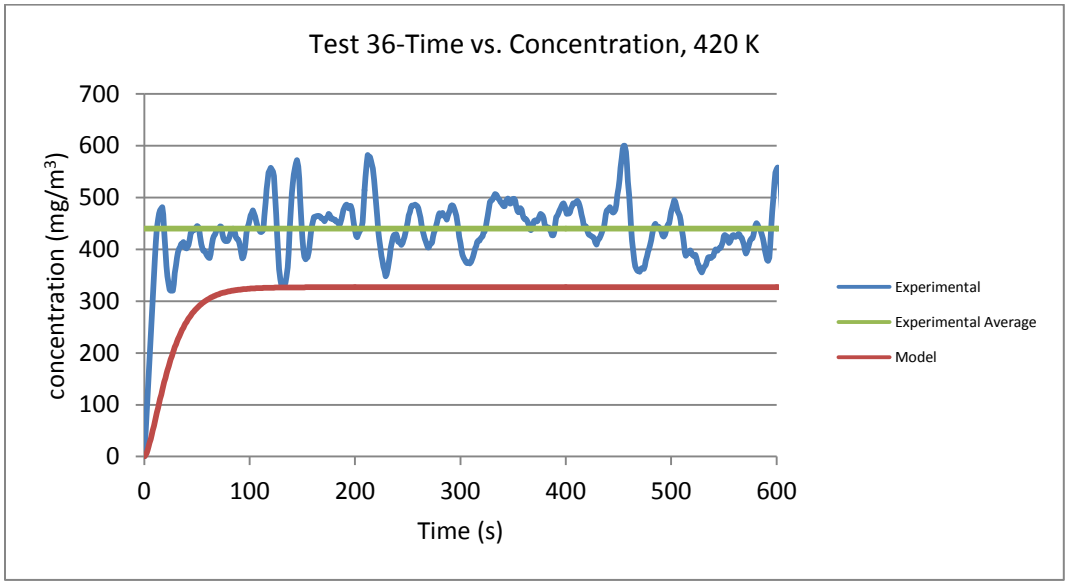

REFERENCE LIST

[1] Ramsbottom, J., 1854, "On an Improved Piston for Steam Engines," ARCHIVE: Proceedings of the Institution of Mechanical Engineers 1847-1982 (vols 1-196), 5(1854), pp. 70-74.
[2] Ramsbottom, J., 1855, "On the Construction of Packing Rings for Pistons," ARCHIVE: Proceedings of the Institution of Mechanical Engineers 1847-1982 (vols 1-196), 6(1855), pp. 206-208.
[3] Miller, G. M., 1862, "On a Packing for Pistons of Steam Engines and Pumps," ARCHIVE: Proceedings of the Institution of Mechanical Engineers 1847-1982 (vols 1-196), 13(1862), pp. 315-327.
[4] Shell, P. J. B., 1992, "Relationship between Oil Consumption, Deposit Formation and Piston Ring Motion for Single-Cylinder Diesel Engines," SAE Paper No. 920089.
[5] Tian, T., Noordzij, L. B., Wong, V. W., and Heywood, J. B., 1998, "Modeling Piston-Ring Dynamics, Blowby, and Ring-Twist Effects," Journal of Engineering for Gas Turbines and Power, 120(4), pp. 843-854.
[6] Castleman, R. A., 1931, "The Mechanism of the Atomization of Liquids," Bureau of Standards Journal of Research, 7(pp. 269-376).
[7] Ruddy, B. L., Dowson, D., and Economou, P. N., 1981, "Prediction of Gas Pressures within the Ring Packs of Large Bore Diesel Engines," Journal of Mechanical Engineering Science, 23(6), pp. 295-304.
[8] Ting, L. L., and Mayer Jr, J. E., 1973, "Piston Ring Lubrication and Cylinder Bore Wear Analysis - 1. Theory," American Society of Mechanical Engineers (Paper), (73 - Lub-25).
[9] Rhode, S. M., 1980, "Mixed Friction Model for Dynamically Loaded Contacts with Application to Piston Ring Lubrication," AGARD Lecture Series, pp. 19-50.
[10] Keribar, R., Dursunkaya, Z., and Flemming, M. F., 1991, "An Integrated Model of Ring Pack Performance," Journal of Engineering for Gas Turbines and Power, 113(3), pp. 382-389.
[11] Miyachika, M., 1991, "An Analytical Evaluation Method for Lubrication Oil Consumption," Proceedings of the Institution of Mechanical Engineers. Part D, Journal of Automobile Engineering 205(1), pp. 31-39.
[12] Hoult, D. P., and Shaw, B. T., 1994, "Puddle Theory of Oil Consumption," S T L E Tribology Transactions, 37(1), pp. 75-82.
[13] Depetris, C., Giglio, V., and Police, G., 1996, "Some Insights on Mechanisms of Oil Consumption," SAE Paper No. 961216.
[14] Yilmaz, E., Tian, T., Wong, V. W., and Heywood, J. B., 2004, "The Contribution of Different Oil Consumption Sources to Total Oil Consumption in a Spark Ignition Engine," SAE Paper No. 2004-01-2909.
[15] Cho, Y., and Tian, T., 2004, "Modeling Engine Oil Vaporization and Transport of the Oil Vapor in the Piston Ring Pack of Internal Combustion Engines," SAE Paper No. 2004-01-2912.
[16] Chun, S. M., 2005, "Computer Program Development Predicting Engine Oil Consumption," ASME Conference Proceedings, 2005(42029), pp. 593-594.
[17] Day, L., 2008, "Lost in the Cracks (or Where Oil Meets the Ring)," Tribology and Lubrication Technology, pp. 31-39.

[18] Plateau, J. a. F., 1873, *Statique Expérimentale Et Théorique Des Liquides Soumis Aux Seules Forces Moléculaires*, Paris, Gand [printed], 1873.
[19] Triebnigg, H., 1925, *Der Einblase- Und Einspritzvorgang Bei Dieselmaschinen*, Springer, Wien.
[20] Weber, C., 1931, "Disintegration of Jets," Journal of Applied Mathematics and Mechanics, 1(11), pp. 136-154.
[21] Hinze, J. O., 1948, "Critical Speeds and Sizes of Liquid Globules," Applied Science Research, 1(1), pp. 273-288.
[22] Morrell, G., 1961, "Critical Conditions for Drop and Jet Shattering," NASA Technical Note D-677.
[23] Ingebo, R. D., 1985, "Liquid Fuel Spray Processes in High-Pressure Gas Flow," NASA Technical Memorandum 86944.
[24] Reitz, R. D., and Bracco, F. V., 1982, "Mechanism of Atomization of a Liquid Jet," Physics of Fluids, 25(10), pp. 1730-1742.
[25] O'rourke, P. J., and Amsden, A. A., 1987, "The Tab Method for Numerical Calculation of Spray Droplet Breakup," SAE Paper No. 872089.
[26] Diego, A. A., 2005, "Numerical and Experimental Study of Air and Fuel Flow in Small Engine Carburetors," Ph.D. thesis, University of Wisconsin-Madison, Madison, Wisconsin.
[27] Inc., C. E., 2011, Ck Engineering Inc. Home, January 2, http://www.c-kengineering.com/.
[28] Photos courtesy of Harold McCormick - CK Engineering, Ballwin Missouri 2012.
[29] Ross, S., 1950, "Variation with Temperature of Surface Tension of Lubricating Oils," Technical Report No. Stanford University, Washington D.C.
[30] Correspondance from ATS RheoSystems to CK Engineering, 2010.
[31] Lefebvre, A. H., 1989, *Atomization and Sprays*, Hemisphere Pub. Corp., New York.
[32] Munson, B. R., Young, D. F., and Okiishi, T. H., 1999, *Fundamentals of Fluid Mechanics*, John Wiley, New York.
[33] Olson, R. M., 1973, *Essentials of Engineering Fluid Mechanics*, Intext Educational Publishers, New York.
[34] Campbell, J., 2003, *Castings*, Butterworth-Heinemann, Oxford [u.a.].
[35] Padday, J. F., and Pitt, A. R., 1972, "Surface and Interfacial Tensions from the Profile of a Sessile Drop," Proceedings of the Royal Society of London. Series A, Mathematical and Physical Sciences, 329(1579), pp. 421-431.

VITA

Brian Ellis Dallstream was born in Columbia, Missouri on October 8, 1979, the son of Charles and Susan Dallstream. After completing high school at Richmond High School in Richmond, Missouri in 1998, he attended Maple Woods Community College in Kansas City, Missouri from 1998-2001. He graduated with an Associate of Engineering degree in 2001. From 2001-2012, he attended the University of Missouri, located in Kansas City, Missouri. He graduated with a Bachelor of Science degree in Mechanical Engineering in 2003 and a Master of Science degree in Mechanical Engineering in 2006. Brian then entered the Interdisciplinary Ph.D., program majoring in Mechanical Engineering and Physics, at the University of Missouri in Kansas City, Missouri in the summer of 2006. While attending graduate school he was a student instructor, teaching assistant, lab instructor, and researcher to several faculty members in the Civil-Mechanical Engineering Department in the University of Missouri's School of Computing and Engineering. When Brian was not in the University setting, he taught physics and mathematics at a local community college and worked as an engineering consultant both privately and for an engineering consulting company. As of right now, Brian is looking forward to graduation and to the next phase in his life, joined by his wife, Katherine, and their son Riley.